





Infrared-Enhanced Electron Emission from Nanoantennas for Optical Detection

by Giorgia Ciuffarella

in partial fulfillment of the requirements for the degree of

Nanotechnologies for ICTs - Micro and Nanotechnologies for Integrated Systems

October 2025

Authored by: Giorgia Ciuffarella

Supervisor: Prof. Fabrizio Giorgis

Advisors: Dr. Phillip D. Keathley

Infrared-Enhanced Electron Emission from Nanoantennas for Optical Detection

Abstract

Within optical systems, Infrared (IR) detectors are a key focus of research because of the need for low-power, high-performance, versatile devices. Conventional IR technologies are limited by a trade-off between system requirements and performance. Microbolometers exploit thermal phenomena; they operate at room temperature but suffer from slow response and low sensitivity. Meanwhile, semiconductor detectors offer superior performance but require cryogenic cooling, since their working principle relies on the photoelectric effect. Many past works have presented plasmonic nanostructures as candidates for next-generation detectors in the visible spectral region, but few have considered this approach for infrared detection. The work in this thesis explores an alternative approach based on plasmonic nanoantennas engineered for both Field- and Schottky-mediated electron emission and collection.

Electromagnetic and thermal simulations were used for the design of new detector geometries, whose properties have been optimized for resonance conditions, field enhancement, thermal hotspot formation, and electron transport from emitter to collector. Initial steps relied on the analysis of previous reports addressing photocurrent in similar structures that were attributed purely to infrared-enhanced Fowler-Nordheim tunneling. With further analysis, however, it was found that other regimes should not be ruled out. Indeed, it has been shown that there are three key electron emission regimes to consider from biased metalic nanoantenna structures: Schottky emission at low bias, Fowler-Nordheim tunneling at higher bias, and space-charge saturation. This thesis aims to explore devices designed to leverage either the Schottky or Fowler-Nordheim tunneling regime for roomtemperature IR detection. We develop a fabrication process employing electronbeam lithography, thin-film deposition, and substrate underetching. Scanning electron microscopy (SEM) and elemental analysis were used to verify the nanogap integrity and revealed process challenges such as gold damage and residual oxides. A custom optical setup integrating a Fourier Transform Infrared (FTIR) source, off-axis parabolic mirrors, and lock-in detection was designed and implemented to conduct photocurrent measurements under IR illumination. Initial tests have confirmed a measurable infrared photoresponse consistent with Schottky emission. These results indicate the feasibility of plasmonic nanoantenna-based IR detection at room temperature and provide a basis for further optimization and for the development of more complete imaging systems.

Contents

Li	st of	Acronyms	4
Li	st of	Figures	12
1	Intr	Structure of the dissertation	13 17
2	Stat 2.1 2.2 2.3	te of the art of IR detectors Overview of Infrared Detectors: Thermal and Photon Detectors Optical Nanoantennas: Design and Prior Applications Plasmonic Hot-Electron and Emission-Based Detectors	19 19 25 28
3	Elec 3.1	etron Emission Mechanisms for Infrared Detection Application of Emission Regimes to Nanoscale Antenna Design	29 33
4	Des 4.1 4.2 4.3 4.4	ign and Nanofabrication of Plasmonic Detector Structure Geometry Concepts and Design Rationale Multiphysics Simulation and Field Analysis Nanofabrication Process Characterization via SEM Imaging	38 38 39 42 47
5	Exp 5.1 5.2 5.3	Optical Characterization and Alignment System	57 57 67 69
6	Opt 6.1 6.2 6.3 6.4 6.5 6.6	Static electrical characterization	72 73 75 78 79 80 81
7	Cor	aclusions and Future Perspectives	84
$R\epsilon$	eferen	ces	87

List of Acronyms

IR – Infrared

FTIR – Fourier Transform Infrared

SEM – Scanning Electron Microscopy

LCC – Leadless Chip Carrier

QNN – Quantum Nanostructures and

Nanofabrication

MIT – Massachusetts Institute of

Technology

SWaP – Size, Weight, and Power

SERS – Surface-Enhanced Raman

Scattering

LSPR – Localized Surface Plasmon

Resonance

LSPRs - Localized Surface Plasmon

Resonances

FN – Fowler–Nordheim

QWIP – Quantum Well Infrared

Photodetector

SLS – Superlattice Structure

MCT – Mercury Cadmium Telluride

PtSi – Platinum Silicide

SiGe - Silicon-Germanium

QDIP – Quantum Dot Infrared

Photodetector

 $\mathbf{Au} - \mathrm{Gold}$

TiN – Titanium Nitride

SiO₂ – Silicon Dioxide

Si – Silicon

OAP – Off-Axis Parabolic

ITO – Indium Tin Oxide

VMA – Voltage Measurement

Amplifier

DC – Direct Current

HeNe – Helium–Neon (laser)

QKD – Quantum Key Distribution

LIGO – Laser Interferometer

Gravitational-Wave Observatory

UV - Ultraviolet

EBL – Electron Beam Lithography

PEC – Proximity Effect Correction

ODUS – Over-Dose/Under-Exposure

NEP – Noise Equivalent Power

D – Specific Detectivity

R - Responsivity

 τ – Response Time

List of Figures

1.1	Photograph of the device embedded on a Leadless Chip Carrier (LCC) to allow reversible integration on a printed circuit board, as an alternative to soldering. Given the periodicity of the nanoantennas array, they appear to be colored due to diffraction effects. Color and intensity appear to scale with geometries and gap size	16
2.1	Figure adapted from [16]. Schematic diagram of a thermal infrared detector. Incident infrared radiation is absorbed by a sensing element, raising its temperature relative to the substrate. The temperature change is converted into an electrical signal through a thermometer element whose resistance, voltage, or polarization varies with temperature. The absorber, thermal link, and supporting substrate determine the detector's responsivity and response time through their thermal conductance and heat capacity	21
2.2	Figure adapted from [25]. Schematic illustration of the operating principle of a photon, or quantum, infrared detector. Incoming infrared photons with energy $h\nu$ greater than the material bandgap E_g are absorbed in the active region, promoting electrons from the valence to the conduction band and generating electron—hole pairs. The resulting photoexcited carriers are collected under an applied bias, producing a measurable photocurrent proportional to the incident photon flux	23
2.3	Taken from [30]. a, Schematic of the device. b, Illustration of the optical field sampling. Attosecond electron bursts are launched from a gold nanoantenna connected to electrodes (a) by a strong driver field $E_D(t)$ (red), collected by an adjacent gold wire, and read out with an external current detector. A weak signal field $E_S(t)$ (blue), about 10^{-4} the intensity of the driver, modulates the average	
	photocurrent $I(\tau)$ as a function of the delay τ (grey)	26

2.4	interface (top) and the corresponding temporal emission (bottom). For $\gamma=20$, the emission follows the pulse envelope, while for $\gamma=0.9$ the electron wavefunction is driven into the vacuum on a sub-cycle timescale of the laser field.	27
3.1	Schematic of Fowler–Nordheim emission. Under an applied bias, the electric field tilts the potential barrier at the emitter interface into a triangular shape, effectively reducing its width and height. Electrons near the Fermi level can quantum-mechanically tunnel across the barrier into the vacuum or opposite electrode, generating a current from source to drain. As the bias (field) increases, the barrier becomes narrower, enhancing the tunneling probability and leading to the characteristic exponential dependence of the Fowler–Nordheim current.	31
3.2	Schematic of Schottky emission mechanism. Under forward bias, the applied electric field at the metal–semiconductor interface lowers the potential barrier through the Schottky effect, reducing the effective work function. Thermally excited electrons with sufficient energy can overcome this field-lowered barrier and be emitted. The resulting current flows from source to drain and increases exponentially with temperature and moderately with the applied field. The barrier maintains a rounded profile, contrasting the triangular shape typical of Fowler–Nordheim tunnelling	33
3.3	Taken from [38]. I–V characteristics of Au and TiN devices. (a) experimental sweep with inset $\ln(I)$ vs $V^{1/2}$ plot (Schottky plot) showing Schottky behavior. The turn-on voltage V_{TH} is extracted from the tangent at 1 nA. (b) data in $\ln(I/V^2)$ vs $1/V$ (FN plot) form highlighting FN behavior. The inset shows a 3D simulation of the field enhancement ($\gamma \sim 7\times$ at the tip). FN fitting would require $\gamma \sim 50\times$, inconsistent with simulation. (c) TiN device with inset Schottky plot, displaying a linear regime followed by superlinear growth and saturation. (d) TiN FN plot confirming that the superlinear regime arises from FN emission, fitted with $\gamma \sim 10\times$, consistent with simulation. Measurements performed at 10^{-6} mbar.	35
3.4	Figure adapted from [37]. Geometries from Piltan et al., used for comparison. (a) 3D rendering of the patterned array with busbars/contact pads. (b) Parameterized unit cell with definitions used in design and simulation: T (lattice pitch), L (arm length), W	
	(arm width), H (notch depth), G (gap), and θ (tip angle)	37

4.1	2D design layouts of the antenna geometries. Planar masks for bowties, nanorods, Schottky nanorods, and triangular antennas define the nominal length, aspect ratio, and gap used for fabrication and simulations. Top row (Schottky devices): unlike prior work, the electron-emission channel (metal-semiconductor junction) is intentionally placed at the point of highest thermal buildup (plasmonic hot spot) rather than at the point of highest field enhancement; this targets thermally assisted Schottky emission under optical heating.	39
4.2	Example of the design flow. From the 2D resonance plots discussed in Section 4.2, a target resonance is chosen, which fixes the required antenna length and aspect ratio. The corresponding geometry is then built in COMSOL. Thermal simulations of this design give access to the local temperature distribution, highlighting the choke-point temperature at the gap and the position of the thermal hotspots across the structure. This sequence illustrates how optical design and thermal analysis are combined in practice to guide device optimization.	40
4.3	2D resonance maps from simulations. Each plot reports the peak temperature and field enhancement factor as a function of antenna length and aspect ratio. The maps allow us to identify the geometrical parameters providing the desired resonance and quantify the expected local field enhancement at the gap. These plots represent the starting point for geometry selection, later transferred to COMSOL for full 3D geometry and thermal simulations	41
4.4	Design maps correlating resonance wavelength, field enhancement, and thermal response. The top panels show the simulated resonance wavelength as a function of antenna length and aspect ratio. Complementary maps report the maximum local field enhancement (FE) at the gap and the corresponding choke-point temperature under illumination. Superimposing these maps highlights regions in parameter space where the optical and thermal constraints are simultaneously satisfied. They are used in the design step to provide for length—aspect ratio combinations that provide the targeted resonance wavelength together with high FE and controlled temperature	
	rise, defining the optimal parameters window for fabrication	42

4.5	Schematic cross-section illustrating the main steps of the fabrication process. The sequence includes substrate preparation, resist coating, electron-beam lithography and development, metal deposition, and lift-off. Subsequently, an optical lithography process is performed to define contact pads on the nanoantennas (not shown here). The final step consists of the underetching of the oxide layer, which releases the structures and reduces dielectric charging effects	43
4.6	Layout view from the GDSII design file. Different colors indicate the swept electron-beam doses used for the fabrication of the antenna arrays. The image also shows the overall contact pattern providing electrical access to the devices. Insets give a magnified view of the arrays, highlighting the individual geometries defined within each block.	44
4.7	Figure adapted from [45]. Schematic representation of a scanning electron microscope (SEM) column and signal detection geometry. The diagram shows the focused primary electron beam interacting with the specimen surface, along with the typical configuration of detectors for secondary electrons (SE) and backscattered electrons (BSE). The insets illustrate how SEs, emitted from near-surface regions, are collected for topographical imaging, while BSEs, scattered from deeper within the interaction volume, provide compositional contrast	48
4.8	Figure adapted from [45]. Schematic representation of the electron–matter interaction volume in a scanning electron microscope (SEM). The diagram highlights the spatial regions from which different signals originate: Auger electrons are generated very close to the surface, secondary electrons (SE) arise from shallow depths and provide topographic information, backscattered electrons (BSE) emerge from deeper regions and carry compositional contrast, while characteristic X-rays and continuum (Bremsstrahlung) X-rays originate from the entire interaction volume. The overall shape and depth of this volume depend on the accelerating voltage and the atomic number of the specimen	49
4.9	InLens SEM images of a bowtie antenna array at increasing magnification. The sequence shows the overall array layout and progressively zooms in on a single device. In the highest magnification image the antenna tips are resolved, revealing a gap of about 20 nm.	50

SEM images of fabricated nanoantenna geometries. (a) Triangular antennas, overdoses array does not present gap (b) Schottky nanorods, designed to present thermal hotspot across the gap region. (c) Bowtie arrays, overdoses array does not present gap (d) Field-enhancing nanorods, overdoses array does not present gap. All images were acquired with the InLens detector to emphasize surface morphology and definition of the gaps	51
Tilted SEM images of the fabricated nanoantenna geometries. (a) Field-enhancing nanorods, (b) triangular antennas, (c) Schottky nanorods, and (d) bowtie antennas. All images were acquired with the InLens detector under tilt 55°, showing that the RIE process produced an anisotropic underetch, leaving the antennas standing on the silicon substrate	52
Tilted SEM image zoomed on a single nanorod. In this chip, the undercut was obtained by anisotropic wet etching, producing a cavity below the structure. As a result, the antenna appears suspended above the silicon substrate, giving the impression of a floating geometry.	52
Comparison of InLens and SE2 imaging for a bowtie antenna. Side- by-side SEM images acquired with the InLens detector (left) and the SE2 detector (right). The InLens image emphasizes the surface morphology and especially clears the gap by the difference in color due to discharging effects, while the SE2 signal provides more superficial contrast, highlighting different aspects of the same structure.	53
Schottky nanorod imaged with InLens and SE2 detectors. Some SEM views show that the gold nanorod was strongly damaged during the underetch process. The structure is barely visible in the InLens image but clearly resolved in SE2, underlining the complementary information provided by the two detectors	53
EDS elemental mapping of a Schottky nanorod array. The maps report the spatial distribution of Si, O, Au, and C. Gold is localized only on the nanorods, confirming the successful definition of the antenna geometry. Silicon and oxygen signals are distributed across the entire substrate, indicating that the underetch was not effective and the oxide layer was not selectively removed. A residual carbon background is also visible, likely from resist contamination. The superimposed spectrum extracted from the mapping region, compared with the background, highlights the clear Au peaks confined to the antennas, while Si and O dominate the substrate signal	55
	lar antennas, overdoses array does not present gap (b) Schottky nanorods, designed to present thermal hotspot across the gap region. (c) Bowtie arrays, overdoses array does not present gap (d) Field-enhancing nanorods, overdoses array does not present gap. All images were acquired with the InLens detector to emphasize surface morphology and definition of the gaps

4.16	SEM images of a Schottky nanorod array after Au loss. InLens (left) shows weak surface contrast; SE2 (center) reveals missing nanorod tips from gold removal. The tilted view (right) confirms the absence of metal and shows residual underetched structures on the substrate.	56
4.17	EDS of a Schottky nanorod array after Au loss. Elemental maps show only Si, O, and C across the substrate; Au is absent. The spectrum likewise lacks Au peaks, indicating complete removal of the nanorods—consistent with SEM evidence of metal loss after underetching	56
5.1	Preliminary sketch of the optical setup. Broadband or laser excitation is directed to the sample through free-space optics. A mechanical chopper modulates the beam to provide the reference for lock-in detection. The light beam is focused onto the chip inside the vacuum chamber, with windows and lenses arranged to preserve alignment and minimize aberrations. The scheme illustrates the optical path and components described in Section 5.1, serving as the basis for the subsequent implementation of FTIR and HeNe excitation sources.	59
5.2	Internal view of the FTIR Nicolet 6700 spectrometer. Photograph showing the main optical components of the instrument: the broadband source, the Michelson interferometer with its moving mirror, and the detector stage. Mirrors, beam splitter, and optical paths are visible, providing a direct view of the layout that underlies the operation of the spectrometer	60
5.3	FTIR reflectance spectrum of the ITO dichroic beamsplitter. The curve reports the measured reflectance as a function of wavelength, showing low reflection in the visible and near-infrared regions and a strong increase beyond 2 µm, where ITO behaves as a metallic reflector. The data confirm the expected dichroic behavior of the coating—transparent at short wavelengths and highly reflective in the mid- to long-wave infrared, consistent with the optical response of conductive oxides	61
5.4	Figure adapted from [50]. Off-axis parabolic (OAP) mirror geometry. The diagram defines the parent focal length (from the vertex), off-axis angle, reflected effective focal length (EFL), focal point, and mechanical distances A (aperture setback), B (back working distance from mirror back), C (edge clearance), plus the mirror diameter and Y-offset of the off-axis section.	62

5.5	Images from the custom-built microscope given by a pair of OAP mirrors. Left: overview of the entire chip under illumination. Right: magnified view with the $20 \times$ objective, where the green tracer beam used for alignment and aiming is clearly visible on the sample surface.	64
5.6	Schematic of the final experimental setup. The diagram summarizes the complete optical and electronic chain: broadband or laser source, beam conditioning and focusing optics, chopper for modulation, and the vacuum chamber containing the device. The photocurrent is converted to voltage by the transimpedance amplifier, referenced to the chopper, and read out by the lock-in amplifier. Additional elements such as shielding, FTIR coupling, and the VMA for noise analysis are included, providing a full overview of the setup as implemented in this work.	65
5.7	Photograph of the final experimental setup. The main optical path with mirrors, focusing optics, and the vacuum chamber is visible, together with the alignment tools and mechanical mounts. The picture provides an overview of the laboratory arrangement used for the measurements described in Chapter 5	66
6.1	Figure adapted from [37]. Reference dark (blue) and illuminated (red) I–V characteristics for a metal–insulator–metal nanojunction under broadband excitation. Illumination lowers the effective barrier and enhances tunnelling/Schottky emission, giving a larger current magnitude and a small photo-offset near zero bias. This qualitative trend is what we expect and use as a guide in the first tests	73
6.2	SEM illustrating device failure: only one column is still electrically connected out of the whole array (left) and broken wires (right). The failure is due to electromigration of columns presenting one or multiple shorted antenna devices	75
6.3	SEM image showing the intentional thinning of the connecting wire (adapted from [54]). This structural modification was introduced to enable the selective disconnection of shorted antenna columns: when a column exhibited an electrical short, localized electromigration at the thinned region effectively isolated it from the circuit	76
6.4	Mid-IR portion of Globar spectrum, providing a broadband infrared illumination peaking in the mid-IR region. It spans wavelengths ~ 1 - $17\mu m$, corresponding to wavenumbers ~ 600 - $10000cm^{-1}$.	77

6.5	Lock-in photocurrent versus long-pass (LP) filter cut-on wavelength at fixed bias and identical optical alignment. The signal decreases monotonically and vanishes with a 1.5 μm LP, indicating that the detected response is dominated by sub-1.5 μm (NIR) content rather than mid/LWIR band radiation	78
6.6	Normalized lock-in amplitude versus normalized chopping frequency f/f_c for a first-order RC-coupled (high-pass) model of the device. The response is suppressed at very low f , rises monotonically through the cutoff, and approaches a constant for $f \gg f_c$, consistent with charging-dominated behavior, where $f_c = 1/(2\pi RC)$.	79
6.7	Photocurrent as a function of modulation frequency, measured under FTIR illumination at a constant 5 V bias. The increase in signal is consistent with the suppression of oxide-related capacitive effects at higher frequencies	80
6.8	Discrimination between emission mechanisms: experimental data plotted as $\log(I)$ vs $V^{1/2}$ (blue) compared with a Schottky fit and a Fowler–Nordheim (FN) fit. In this Schottky-linearization, the data follow a near-linear trend reproduced by the Schottky model (orange), while the FN model (green) shows strong curvature and mismatch. This indicates Schottky-dominated transport over the measured bias range at room temperature	81
6.9	Photocurrent as a function of applied bias under FTIR illumination at a chopping frequency of 500 Hz. At low biases (< 3 V), the signal remains below the detection threshold, while around 5 V, a stable photoresponse emerges, indicating the onset of field-assisted emission. For higher biases, the photocurrent follows a quasi-exponential trend, reaching ~ 4 pA at 10 V. The insert shows a Schottky plot, $\log(I)$ as a function of $V^{1/2}$, the linear relation supports a Schottky type of emission at higher biases	82
7.1	Summary of first measurements, determining the first photocurrent in Schottky-type devices. Left: FTIR illumination (source 1.5–17 μm ; measured response attributed to the NIR tail) photocurrent vs. bias. Peak responsivity at 10 V is 45 m/W . Inset: log(I) vs $V^{1/2}$; the linear trend indicates Schottky-type emission at higher biases. Right: measured photocurrent in the lock-in vs chopping frequency. The monotonic increase with frequency is consistent with charging-induced high-pass behavior; no roll-off was observed	
	within the tested range $(\sim kHz)$	86

1. Introduction and Research Motivation

Optical detection systems represent a fundamental tool for many scientific fields, both in research and industry contexts [1–3]. Light-matter interaction is used for various applications, such as spectroscopy [4–6], thermal imaging [7], telecommunications [8, 9], environmental monitoring [10], and biomedical diagnostics [11, 12. Each field imposes performance requirements and operational constraints that call for a wide diversification of every system. As a result, detection architectures have evolved into highly sophisticated technologies, with different tailored designs and functions to address the details of their own applications. Driven by interdisciplinary research, the development of these systems eventually moved towards their refinement through the application of a diverse array of physical principles. Over time, advances in the field have been matched by designs and functionalities being added to their systems, carefully optimized to meet the specific demands required by their domain of use. Despite the diversity of existing systems, achieving both high speed and high sensitivity at room temperature remains a fundamental challenge. This trade-off motivates the exploration of alternative detection mechanisms, opposed to traditional photon or thermal-based systems.

The most advanced devices, depending on the field of use and purpose, require high performance in specific ways. In biomedical imaging, for example, fast three-dimensional photoacoustic tomography systems are widely used [11]. They are based on ultrasound sensors combined with an optical readout and a Fabry-Pérot-like structure, originally conceived for optics and photonics contexts. The use of high-repetition laser sources enables volumetric blood and liquid imaging in vivo without the need for piezoelectric-based systems. These techniques are highly advanced for what concerns detection depth, allowing millimeter scale analysis and speed reaching hundreds of milliseconds. Autonomous vision systems represents another rapidly emerging field, where the demand for rapid response and minimal delay is steering research toward novel device innovations. Current systems predominantly utilize neuromorphic event-based cameras, which achieve rates of up to 5,000 frames per second [13]. This is made possible by an event trigger mechanism capable of microsecond-level intensity modulation per pixel. Each specific application requires an emphasis on parameters such as detection volume, temporal resolution, sensitivity, or bandwidth. One domain where highperformance optical systems are crucial is quantum communication. Quantum Key Distribution (QKD) networks, such as those deployed across terrestrial and satellite links in China, leverage photon-based protocols for secure key exchange [9]. These systems integrate low-loss optical fibers with free-space laser satellite terminals to enable high-throughput, globally scalable quantum-secure communications.

Gravitational wave detection offers another possible example of optical system deployment. Facilities like the Laser Interferometer Gravitational-Wave Observatory (LIGO) or VIRGO facility utilize kilometer-scale laser interferometry to detect gravitational wave sources on Earth. These setups demand exceptional sensitivity and stability, and the need for a lower noise level fuels this development branch. Quantum-enhanced techniques such as squeezed light injection have further improved detection thresholds closer to sub-quantum noise regimes [5, 14. Beyond visible light, many detection systems also operate in different regions of the spectrum, especially in the ultraviolet (UV) and infrared (IR) domains. This is especially true in spectroscopy, where accessing a broader spectrum is often a fundamental requirement. One example is dual-comb spectroscopy with single-photon sensitivity, that has emerged as a novel technique in the near-UV [4]. This apparatus employs slightly detuned frequency combs, which have become widely adopted in optical systems. Their technology allows the system to achieve a quasi-quantum-limited signal-to-noise ratio when operating in single-photon regime. By carefully tuning the frequency combs, this technique can reach broadband, ultra-high-resolution spectral measurements with nearly quantum-limited signal-to-noise ratios.

There are many other characterization techniques which focus on regions of the spectrum extending into the infrared. Some of these systems serve environmental sciences, with gas sensing being a major application. Many greenhouse gases and pollutants, such as carbon dioxide (CO₂) and methane (CH₄), exhibit characteristic absorption features in the IR. To detect them effectively, research has moved towards the development of sensors that combine high speed, low noise, and broad bandwidth [10]. For similar reasons, mid-IR sensors are deployed in spacebased sensing as sensitive astronomical imagers [6]. Infrared (IR) systems are also widely used for thermal imaging and night-vision applications, including compact, lightweight sensors designed for wearable or drone-mounted systems. These contexts demand fast, sensitive, and low-power detectors capable of operating at room temperature. The infrared wavelength region is fundamental, as it allows the characterization of objects and processes that are undetectable at shorter wavelengths. This portion of the spectrum offers access to a multitude of phenomena, such as thermal emissions, molecular vibrational modes, and celestial body thermal signatures, for example. Unveiling them allows for the detection of many systems that would otherwise be challenging to analyze.

Numerous IR detection systems have been developed to answer these needs [15],

ultimately converging on two primary approaches: bolometers and semiconductor-based detectors [16]. The technology behind microbolometers offers a well-known and reliable solution that effectively meets SWaP (Size, Weight, and Power) requirements. However, due to their working principle, detecting temperature-induced resistance changes rather than direct photon absorption, they suffer from strict performance limitations that prevent their use in higher-performance contexts [17, 18]. Semiconductor-based detectors, on the other hand, have enhanced sensitivity, faster response times, and broader spectral coverage [19, 20]. One of their major strengths is the vast knowledge and understanding of fabrication techniques acquired in semiconductor industry. However, the inability to operate at room temperature limits their operational use, as the SWaP requirements are not compatible with the need for a cryogenic cooling system. This represents a critical barrier to widespread, low-power deployment.

The necessity of devices combining high detectivity and fast response speed is shifting the attention toward new detection systems based on alternative physical mechanisms. One example is the exploitation of plasmonic nanoantennas for novel optical detectors. These metallic nanostructures at sub-wavelength scales are capable of enhancing the local electromagnetic field through plasmonic effects. The most representative example is given by Surface-Enhanced Raman Scattering (SERS). This application is one of the oldest and most common uses of plasmonics in optical detection and it is still widely used due to its simple yet effective working principle. SERS techniques use localized surface plasmon resonances (LSPRs) in metallic nanoantennas to enhance the Raman signal by amplifying the local electromagnetic field, potentially accessing to single-molecule detection. Ever since their first use, the resonance properties of metallic nanoantennas have represented a useful tool for many different detection types. A key feature of many nanoantenna designs is their nonlinear behavior.

With proper engineering, it is possible to couple the nanoantennas' electromagnetic enhancement with nonlinear electron emission to obtain a new system able to detect light in the IR range. The basic principle is that electron emission across a nanoscale gap coupled to a nanoantenna is perturbed through the absorption of IR light within the antenna. Of particular interest are electron-emission mechanisms based on Fowler–Nordheim (FN) tunneling and Schottky barrier lowering. While optical perturbation of each of these mechanisms can enable photo-induced charge extraction, it is not understood how to best leverage their separate contributions for sensitive IR detection. Understanding these emission mechanisms and how to enhance their sensitivity to IR light within nanoscale antenna and gap structures is the focus of this work.

If successful, the use of this enhanced electron emission approach may open the door to a new class of plasmonic nanoantenna-based IR detectors, less constrained by physical and fundamental limitations. Nanoantennas have already been deployed

in optical sensing application and can be found in a number of previous works. The device presented here deviates from previously reported systems through its operational emphasis on the precise electron emission regime. As will be further analyzed in Chapter 3 metallic plasmonic structures can be engineered to support photo-induced electron emission across a barrier, mediated by localized field enhancement.

This thesis focuses on the analysis, development and characterization of a system able to detect light in the IR regime by taking advantage of the combined phenomena of plasmonic electrical enhancement and non-linear electron emission. Based on prior work, the system presented here adapts proven nanoantenna geometries to the novel operational context of IR detectivity at room temperature. The device will be characterized to demonstrate its IR sensitivity and benchmark its performance relative to existing IR detection technologies.

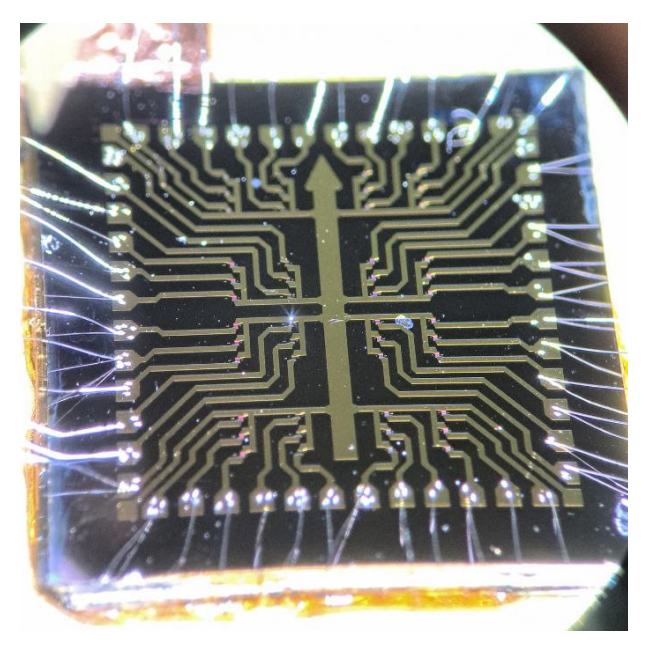


Figure 1.1: Photograph of the device embedded on a Leadless Chip Carrier (LCC) to allow reversible integration on a printed circuit board, as an alternative to soldering. Given the periodicity of the nanoantennas array, they appear to be colored due to diffraction effects. Color and intensity appear to scale with geometries and gap size

1.1 Structure of the dissertation

The document is structured to guide the reader through the development of the system in several steps. The thesis provides a total of seven chapters and aims to present the general progression leading towards product realization. The first introductory part is given to the reader as a guide to this study field and contains a brief presentation of the state of the art in IR detection sensors as well as the theoretical background. The design process is presented alongside the fabrication steps and challenges. Intrinsically embodied within them is also a presentation of characterization techniques used to close the feedback cycle with the fabrication process in the early stages. Central to this document is the characterization of the device: the custom setup schematic and the performances obtained.

Given the nature of this thesis project, which is conceived to be part of a long-term ongoing work conducted by the research group, the document also offers a theoretical overview of potential advancements of the reported device. By illustrating the opportunities enabled by this technology, we also propose a conceptual implementation of a complete infrared camera system, which represents the ultimate goal. The final chapter of this document will contain an overall reflection on the thesis work and its key contributions to the field.

In Chapter 2 a broad review of state-of-the-art IR detection systems is presented. A brief theoretical presentation of their mechanisms and limitations is meant to guide a critical and informed comparison between products in the current market and benchmarking in this landscape. A particular emphasis is set on novel devices and specifically on the two main technologies, microbolometers and semiconductor detection systems, and how this device would be positioned in this context.

Chapter 3 illustrates theoretical insights on the Fowler-Nordheim tunneling principle and the Schottky Emission principle. These notions will be useful to understand the design choices used to engineer the device. The understanding behind the difference between these two mechanisms is the key reason that led to the project.

The following Chapter 4 describes the device design rationale, starting from proven structures and geometries. Section 4.1 explores the design choices, tailored to address this specific emission regime, and Section 4.2 illustrates the associated computer-aided simulations. Section 4.3 faces the fabrication steps and the challenges met when trying to develop the final recipe for the process. Since achieving consistent nanometric gaps is a major challenge, the imaging process represented an important part of the process and is explained in Section 4.4.

Following up, Chapter 5 describes in detail the characterization setup. The first part, mainly Section 5.1, introduces the system more focused on the optical side. Finally, Section 5.2 will describe the electronics and signal-processing chain

developed for the measurements, while Section 5.3 will discuss the strategy adopted for optical alignment and the overall setup optimization, outlining the trade-offs that guided its configuration.

Chapter 6 will present the experimental results, focusing on the device's electrical and optical response under different illumination regimes and bias conditions. The discussion will include the observed behaviour across wavelengths, frequency response, and stability, as well as a comparison with conventional IR detector performances.

Chapter 7 will summarize the main outcomes of this research and highlight potential future directions, both in terms of design refinement and extended operational bandwidth.

2. State of the art of IR detectors

The project is intended to propose an innovative approach to Infrared (IR) detection, offering an innovative solution to a performance-related gap in the existing technologies. The following section is intended to provide an overview of current IR detection methods, emphasizing why there is an increasing interest in emerging technologies and why traditional systems struggle to provide simultaneously high performance and room-temperature operation. This challenge motivates the investigation of plasmonic structures, whose field-enhancement capabilities, well established in the visible, can be tuned to operate in the IR, though their use as direct IR detectors remains largely unexplored. This analysis is crucial to better contextualize the proposed alternative approach and to identify its future position in the market landscape.

2.1 Overview of Infrared Detectors: Thermal and Photon Detectors

The landscape of classical infrared (IR) detectors is characterized by two principal classes: photon detectors and thermal detectors. While the first category relies on quantum excitation of charge carriers by incident photons, the latter detects the temperature rise caused by absorbed infrared radiation. Thermal detectors offer broadband response and room-temperature operation but exhibit lower performance due to slow temporal response and reduced sensitivity. On the other hand, photon detectors, typically semiconductor-based, provide higher sensitivity and faster response times, though they require cryogenic cooling, making them unsuitable for compact or portable low-power systems. This fundamental difference is reflected in their application fields: photon detectors' main driver is given by military applications and scientific imaging, whereas thermal detectors prevail in civilian and commercial uses, where cost and simplicity overcome the need for ultimate performances [3, 15, 21–24].

Beyond the specific operational principles, all infrared detectors are commonly characterized by a set of figures of merit defining their sensitivity and speed. The main parameters used to describe them are the specific detectivity (D^*) , responsivity (R), and response time (τ) . The detectivity quantifies the smallest optical signal that a detector can distinguish from its intrinsic noise and provides

a normalized measure of performance across different device areas and bandwidths. It is expressed as:

$$D^* = \frac{\sqrt{A\Delta f}}{NEP} \tag{2.1}$$

where A is the active area, Δf the electrical bandwidth, and NEP the Noise Equivalent Power, representing the minimum detectable optical power at unit signal-to-noise ratio. The responsivity, defined as:

$$R = \frac{I_{ph}}{P_{out}} \tag{2.2}$$

relates the generated photocurrent $I_{\rm ph}$ to the incident optical power $P_{\rm opt}$ and serves as a direct indicator of the conversion efficiency. Since D^* scales proportionally with R and inversely with the total noise current, the two parameters are often analyzed together to evaluate detector performance. The unit commonly used to express detectivity is the Jones, defined as $cmHz^{1/2}/W$. One Jones corresponds to a detector capable of distinguishing a signal of $1~W/cm^2$ with a noise bandwidth of 1 Hz. This unit, therefore, quantifies the normalized sensitivity of the detector, allowing direct comparison between devices operating under different conditions.

Finally, the response time (τ) determines how rapidly the detector output can follow variations in illumination, setting the upper limit of its operational bandwidth. For thermal detectors, it is governed by the ratio between heat capacity and thermal conductance $(\tau = C/G)$, while photon- and field-assisted mechanisms enable much shorter responses, reaching the microsecond or nanosecond regime. These quantities provide a tool to compare different infrared technologies and express the fundamental trade-off between sensitivity and speed that defines their overall performance.

Thermal Detectors

The first class to be analyzed is that of thermal detectors, whose operation is based on the rise in temperature of the element denominated *absorber* due to incident IR power. The temperature difference translates into a measurable change in a physical property of the absorber, such as electrical resistance, polarization, or gas pressure, varying based on the absorber type. As this mechanism relies on the absorbed energy and is not dependent on photon wavelength, thermal detectors offer broadband detection, whose only constraint is given by the absorber's ability to efficiently capture the incoming radiation.

The most representative device of this category is the bolometer, whose functioning relies on a temperature-dependent resistance :

$$\Delta R = \alpha R_0 \Delta T \tag{2.3}$$

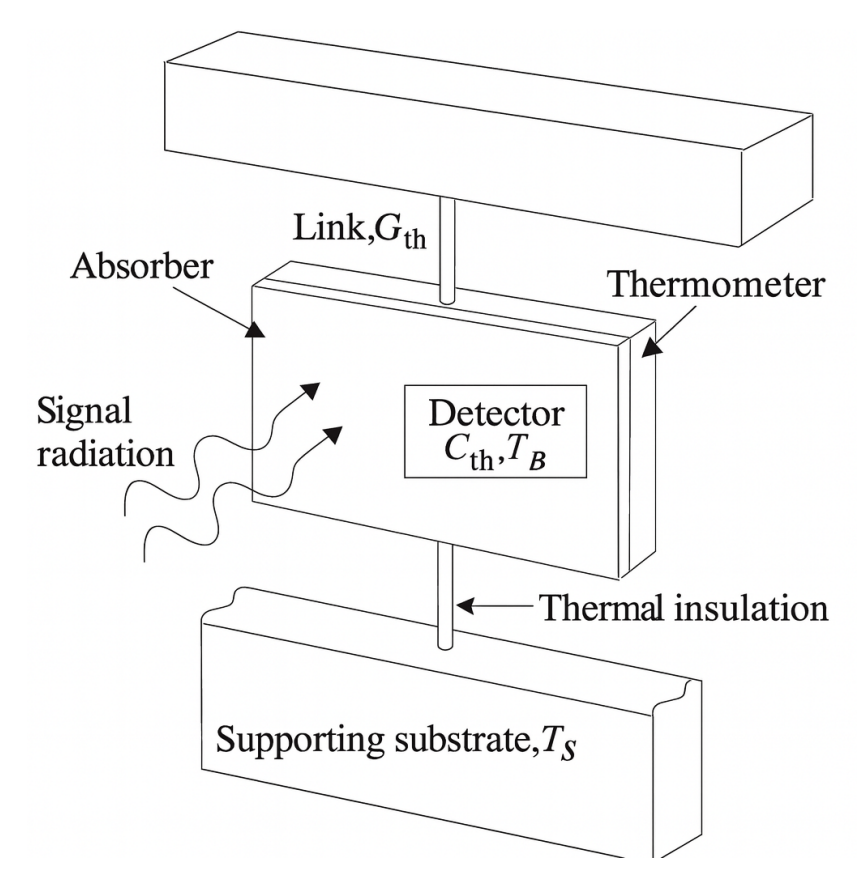


Figure 2.1: Figure adapted from [16]. Schematic diagram of a thermal infrared detector. Incident infrared radiation is absorbed by a sensing element, raising its temperature relative to the substrate. The temperature change is converted into an electrical signal through a thermometer element whose resistance, voltage, or polarization varies with temperature. The absorber, thermal link, and supporting substrate determine the detector's responsivity and response time through their thermal conductance and heat capacity.

where α is the temperature coefficient of resistance (TCR). The absorbed radiation causes a difference in temperature, generating a resistance change that is read out electrically. The detector's response time is given by:

$$\tau = \frac{C}{G} \tag{2.4}$$

where C is represents the heat capacity and G the thermal conductance. Since the bolometer's functioning performs an integration over absorbed power, the response time will be intrinsically slower than that of photon-based detectors. While early bolometers used platinum-based resistive elements, modern devices employ advanced materials and architectures. A widely adopted technology is based on the use of Vanadium Oxide (VO_x) , characterized by a high TCR and therefore high sensitivity. Due to remarkable electrical and thermal properties, VO_x represents a mature technology, diffused and dominant in different markets other than microbolometer devices. An important emerging competitive alternative is amorphous silicon (a-Si), offering similar characteristics and compatibility with Complementary Metal-Oxide-Semiconductor (CMOS) fabrication processes. Due to the semiconductor industry's history, silicon devices benefit from extensive knowledge in fabrication techniques, allowing a better tuning of properties and performances. Another significant alternative exploits Micro-Electro-Mechanical Systems (MEMS) microbolometers, in which the absorber element is a suspended membrane isolated thermally from the substrate. MEMS technology allows compact and low-power detectors while benefiting from CMOS-compatible fabrication techniques. Indeed, MEMS, alongside NEMS technology, has been exploited for several decades due to the ease of fabricating compact devices based on a suspended element like the absorber. Furthermore, MEMS platforms enable wavelength sensitivity by integrating plasmonic metal-insulator-metal absorber, typically gold antenna arrays separated by aluminium-oxide (Al_2O_3) spacers. By tuning the antenna geometry, it is possible to engineer the resonance peak and thus the optimal detection wavelength. Overall responsivity is given by a combination of the optical absorption and the electrical response of the system. The resulting plasmonic MEMS bolometers offer compactness and robustness, making them optimal options for on-chip spectrometers, gas sensors, and Internet-of-Things (IoT) applications. Thermal detectors also include pyroelectric devices, thermopiles, and Golay cells, each with distinct advantages and performance ranges (Table 2.1). Due to the different operating principles, there is a great variation across technologies in their detectivity (D^*) and response time.

Commercially diffused VO_x microbolometers typically achieve $D^* \approx 10^{10} - 10^{11}$ Jones and response times of 5-15 ms, while amorphous silicon counterparts show comparable detectivity and a tunable spectral response when engineered with MEMS absorbers. Both detectivity and response time decrease when considering pyroelectric detectors, usually reaching $D^* \approx 10^8 - 10^9$ Jones with slightly faster (1-10 ms) response, whereas Golay cells are used when higher sensitivity is needed, like for laboratory spectrometers, but they represent slow (hundreds of ms) and bulky systems.

Photon Detectors

The second main category is represented by photon detectors, widely used for high-performance and defense applications. These devices are based on semiconductor band-structure physics, where incident photons are absorbed by the material and excite electrons across the bandgap, creating an electron-hole pair. As the process requires the photon energy to match the bandgap of the material, photon detectors exhibit wavelength-selective response. The excitation process can be intrinsic, exciting carriers across the entire bandgap, or extrinsic, when the phenomenon

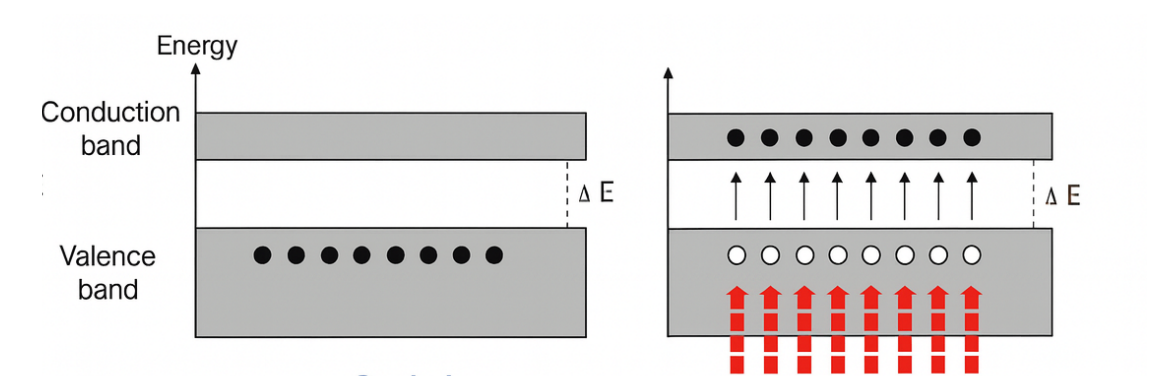


Figure 2.2: Figure adapted from [25]. Schematic illustration of the operating principle of a photon, or quantum, infrared detector. Incoming infrared photons with energy $h\nu$ greater than the material bandgap E_g are absorbed in the active region, promoting electrons from the valence to the conduction band and generating electron—hole pairs. The resulting photoexcited carriers are collected under an applied bias, producing a measurable photocurrent proportional to the incident photon flux.

leverages impurity levels. The response is characterized by a cutoff wavelength λ_C , related to the bandgap E_G by:

$$E_g = \frac{hc}{\lambda_C} \tag{2.5}$$

To reach the background-limited infrared photodetector (BLIP) regime, where performances of the device are limited only by the photon shot noise, cryogenic cooling of the semiconductor matrix is required. At cryogenic temperature, thermally generated carriers are suppressed, and the signal-to-noise ratio (SNR) is improved.

Amongst various material systems, bandgap engineering has been used to engineer the spectral response of different detectors. This approach exploits semi-conductor alloys, materials whose bandgap is dependent on chemical composition, to control the cutoff wavelength λ_C . The fabrication technique, however, requires the alloy design to be lattice-matched to avoid crystalline defects as dislocations or internal strain, which could be compressive or tensile. Two materials are to be considered lattice-matched when the lattice constant of the two crystalline structures is nearly identical, allowing them to be grown epitaxially. By lining up their atomic planes, it is possible to minimize strain, dislocations, and defects at the interface.

Historically, older applications used lead chalcogenides like PbS, PbSe, and PbTe as IR materials, later replaced by new indium-based semiconductors such as indium antimonide (InSb) and indium gallium arsenide (InGaAs). These materials are usually involved in detection in short- and mid-wave infrared (SWIR and MWIR) regions, especially in applications like telecommunications and astronomy.

InSb (with $E_g \approx 0.17 \text{ eV}$) and InGaAs ($E_g \approx 1.7 - 3.5 \text{ eV}$, depending on substrate) deliver high sensitivity when cooled to 77 K, achieving sensitivities several orders of magnitude higher when compared to thermal detectors.

To better tune in the spectral response and be able to work in different IR regimes, new detectors have been developed, based on mercury–cadmium–telluride (HgCdTe, or MCT) alloy, offering a bandgap control from 1 to 30 μm . Thanks to its spectral tunability and near-theoretical background-limited performances, it has become the dominating material for IR detection. HgCdTe-based detectors represent the state-of-the-art devices for IR detection across SWIR to LWIR, including most of the photodiodes and avalanche-photodiodes systems. This material, however, presents drawbacks related to mercury volatilization, high cost, and non-uniformity, complicating the fabrication process.

Later developments regarding photon detectors involve some more complex architectures, such as Quantum Well Infrared Photodetectors (QWIPs). Those systems are based on GaAs/AlGaAs and provide large focal-plane arrays (FPAs) and narrow-band response by exploiting intraband transitions. Usually, Quantum Well IR Photodetectors are based on III-V technologies and provide radiation-resistant devices. However, the quantum efficiency and detectivity do not reach the performances found in other photon technologies such as MCT, as summarized later in Table 2.1 for comparison.

Another type-II superlattices (SLS) formed by alternating InAs and GaSb layers have been investigated as a potential HgCdTe replacement. The use of these materials, such as InAs, GaSb, and AlSb, is very much spread in bandgap engineering as they form an almost lattice match around 6 Armstrong, allowing a spectral range between 0.36 eV and 1.61 eV and devices able to operate from MWIR to very-long-wave IR (VLWIR). However, SLS detectors present short carrier lifetimes and suffer from surface passivation challenges, limiting their sensitivity (see Table 2.1 for comparative values).

In general, thanks to the cooling system, photon detectors can achieve high detectivity, wavelength selectivity, and faster response times when compared to thermal detectors. Typical values for lead-salt devices reach $D^* \approx 10^{11}$ Jones with microsecond-scale responses; indium-based alloys reach 10^{12} Jones. QWIPs and SLSs achieve similar values of detectivity and nanosecond to microsecond response times, while HgCdTe (MCT) represents the state-of-the-art of IR devices, with $D^* \approx 10^{13}$ Jones and response time from microseconds to tens of nanoseconds.

It is evident that a technological gap opens in the market, where no practical solution has been found for uncooled infrared detectors combining both high detectivity and fast response. Current uncooled devices typically achieve detectivities below $\sim 10^{10}$ Jones or response times slower than ~ 10 ms, whereas state-of-the-art cryogenic photon detectors can reach $> 10^{13}$ Jones and sub-microsecond response.

This disparity has pushed research toward novel IR detection technologies, including Schottky-barrier detectors (e.g., PtSi and SiGe heterostructures), quantum-dot IR photodetectors (QDIPs), and 2D-material-based devices. This gap motivated the work presented in this thesis, exploring plasmonic nanoantenna architectures capable of coupling electromagnetic energy into electron-emission processes such as Schottky or Fowler–Nordheim tunneling, potentially enabling high-detectivity, fast-response IR detection at room temperature.

Table 2.1: Comparison of the key performance metrics of thermal and photon infrared detectors, summarizing typical spectral ranges, detectivity and response times. Units: detectivity D in cm $\sqrt{\text{Hz}}/\text{W}$; NEP in W/ $\sqrt{\text{Hz}}$.

Detector Type	Spectral Range	D	Response	Notes
VO_x microbolometer	0.5–14 $\mu\mathrm{m}$	$10^{10} - 10^{11}$	5–15 ms	NETD 30–80 mK; uncooled IR cameras
a-Si MEMS bolometer	3–14 μm (tunable)	$\sim 10^{10}$	5–15 ms	CMOS-compatible; plasmonic absorber for selectivity
Pyroelectric (LiTaO ₃ , PZT, BST)	up to $\sim 100~\mu \mathrm{m}$	$10^8 - 10^9$	$1-10~\mathrm{ms}$	Motion sensing, NDIR
Golay cell	broadband	$\mathrm{NEP} \sim 10^{-10}~\mathrm{W}/\mathrm{\sqrt{Hz}}$	$\sim 100 \text{ ms}$	Very sensitive; slow, bulky
PbS / PbSe	$15~\mu\mathrm{m}$	$10^{10} - 10^{11}$	$\mu \mathrm{s}$	Low-cost spectroscopy
InSb	$15.5~\mu\mathrm{m}$	$\sim 10^{12}$	$<1~\mu s$	High-performance MWIR
InGaAs	0.9–1.7 (to 3.5) $\mu\mathrm{m}$	$\sim 10^{12}$	ns $-\mu$ s	SWIR/telecom; extended-range vari- ants
HgCdTe (MCT)	1–30 $\mu\mathrm{m}$	$10^{12} - 10^{13}$	ns– μ s	State-of-the-art; near BLIP
${\rm QWIP} \; ({\rm GaAs/AlGaAs})$	8–15 $\mu\mathrm{m}$	$10^{10} - 10^{11}$	ns– μ s	Large uniform FPAs; QE $\sim 10\%$
$\begin{array}{ccc} \text{Type-II} & \text{SLS} & (\text{InAs/-}\\ \text{GaSb}) \end{array}$	3–15 $\mu\mathrm{m}$	$10^{11} - 10^{12}$	ns– μ s	Alternative to MCT (MWIR/LWIR)

2.2 Optical Nanoantennas: Design and Prior Applications

The central theme of this thesis project is the adoption of nanostructures for alternative IR sensing. To understand the antenna designs used throughout this work, in this section we briefly discuss the original purpose for which they were developed within the Petahertz Nanoelectronics division of the Quantum Nanostructures and Nanofabrication (QNN) group at the Massachusetts Institute of Technology (MIT). Of course, others have also used similar antenna structures for optical detection, largely in the visible and near-infrared spectral regions, and this work is discussed in the following section.

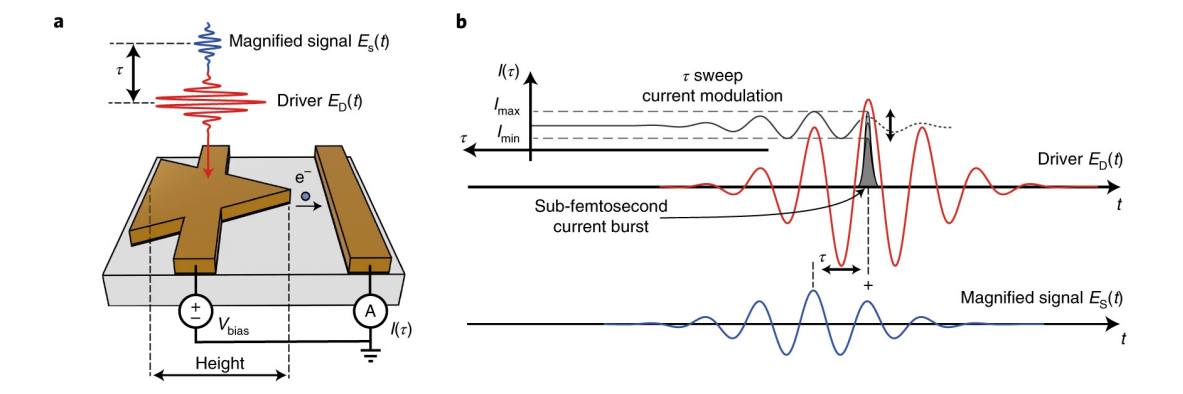


Figure 2.3: Taken from [30]. a, Schematic of the device. b, Illustration of the optical field sampling. Attosecond electron bursts are launched from a gold nanoantenna connected to electrodes (a) by a strong driver field $E_D(t)$ (red), collected by an adjacent gold wire, and read out with an external current detector. A weak signal field $E_S(t)$ (blue), about 10^{-4} the intensity of the driver, modulates the average photocurrent $I(\tau)$ as a function of the delay τ (grey).

The nano-vacuum-gap antennas developed by the MIT group were initially conceived for ultrafast field sampling and carrier-envelope phase detection, achieving attosecond-scale temporal resolution. While this regime extends beyond the operational scope of the present work, it provides the physical and technological foundation on which the proposed IR detector concept is built.

The original goal of the nanoantenna architecture was the realization of on-chip petahertz electronic devices operating at low power. The idea relies on well-known principles of plasmonic effect combined with nanoscale electron emission. Indeed, emission from solids has been largely used, especially in the context of electron guns, analyzing emitter bodies and properties, from point sources to thin films [26–29]. To be able to combine this phenomenon with plasmonic properties such as localized surface plasmon resonance (LSPR) for field enhancement enables matching attosecond techniques with plasmonic electron emitters.

For example, the emission can be engineered to enable subcycle electric field reconstruction and thus allows investigation of its behaviour at specific time instants rather than relying on intensity-based analysis[30], the base principle shown in Figure 2.3. Subcycle field sampling requires very short pulses combined with highly localized and intense electrical fields. The latter condition and its coupling to ultrashort pulses represent the real challenge and innovation [31]. This combination acts like an oscillating modulation of the potential barrier, following the field envelope, that the electron has to face to ultimately tunnel outside of the tip and towards the collector. When the applied electric field works favorably to the emission of the electrons, de facto lowering the potential barrier, the whole system becomes susceptible to tunneling current phenomena, uniquely based on the probed electromagnetic radiation state, before the reversal of the applied field

prevents tunneling. Whenever the tunneling phenomenon is faster than the time the potential barrier needs to switch from one position to the other, field sampling is attainable. In literature, to monitor this ratio, a parameter is commonly used. Namely, the Keldysh parameter [32] is to be defined as $\gamma = t_{TUN}/T$ (where t_{TUN} : tunneling time, T: electric field cycle time), or can alternatively be linked to the workfunction of the material and the electric field peak value. Two regimes then open up, a multiple-photon or perturbative regime, whenever $\gamma >> 1$, as opposed to an optical-tunneling regime whenever $\gamma << 1$.

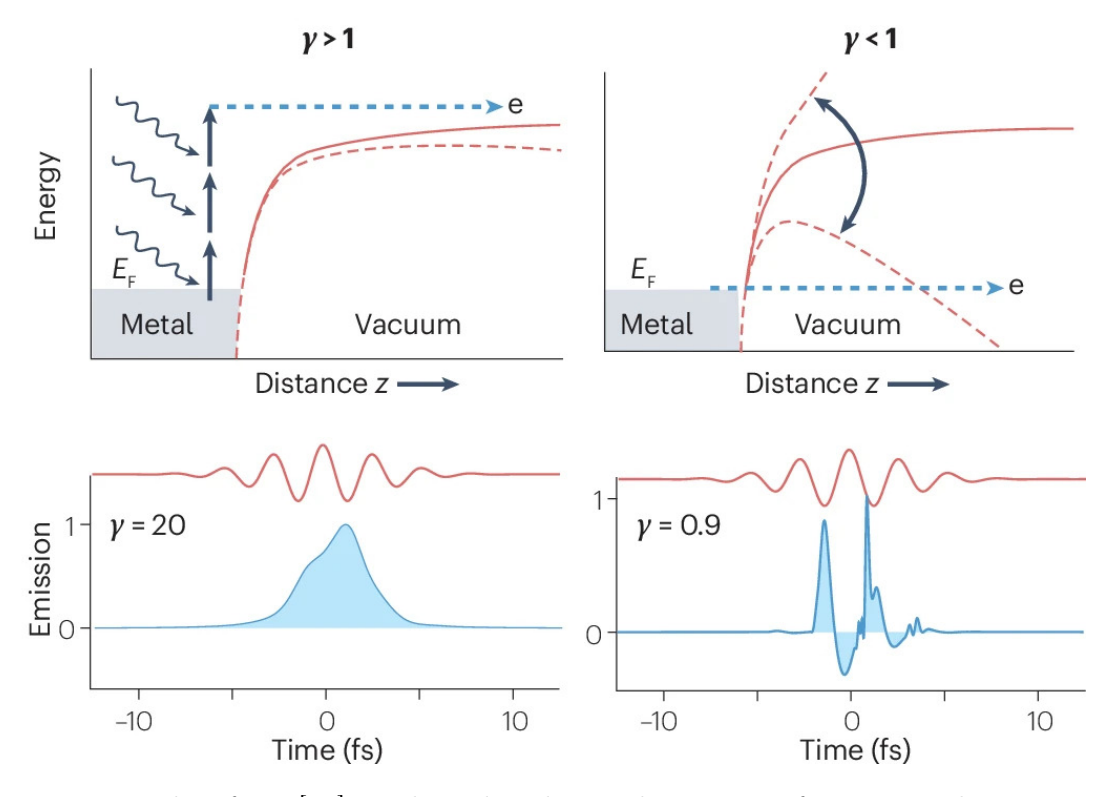


Figure 2.4: Taken from [33]. Light-induced tunnel ionization from a metal–vacuum interface (top) and the corresponding temporal emission (bottom). For $\gamma=20$, the emission follows the pulse envelope, while for $\gamma=0.9$ the electron wavefunction is driven into the vacuum on a sub-cycle timescale of the laser field.

By developing this two-field-based system, the idea of exploiting a similar mechanism to detect infrared radiation arose. The duality of this mechanism holds the potential for a high-performance Size–Weight–and–Power (SWaP)-friendly IR detector. This idea was indeed then further supported by a detailed analysis of the underlying emitting mechanisms of these structures, which will be further analyzed in Chapter 3.

2.3 Plasmonic Hot-Electron and Emission-Based Detectors

In addition to their use for field sampling and ultrafast optical control, plasmonic nanoantennas have also been explored as active photodetectors. Their ability to locally enhance electromagnetic fields at specific locations enables the generation of charge carriers, which can produce measurable currents. These so-called hot-electron detectors mainly operate in the visible and near-infrared range, where photon energies are sufficient to promote carrier emission across a potential barrier. Several studies have implemented this concept in different nanometric structures, obtaining various levels of efficiency and spectral sensitivity. Works such as those presented by Sun et al. [34], Chalabi et al. [35], and Pertsch et al. [36] exploit plasmonic effects to convert incident optical radiation into electrical current, achieving fast temporal response and tunable detection properties.

Extending these principles to longer wavelengths is considerably more challenging, as the lower photon energies in the mid-infrared regime reduce the probability of direct photoemission. An interesting case study was reported by Piltan et al. [37], describing a plasmonic-enhanced detector based on Fowler–Nordheim tunneling that nominally operates in the MIR range. Their work represents an important step toward plasmonic emission-based detection beyond the visible, linking field-induced tunneling with localized surface-plasmon enhancement. However, the reported emission currents and optical modulation levels suggest contributions that are not yet fully understood and may involve competing transport mechanisms or thermal effects. Further experimental confirmation and systematic analysis are required to clarify the true origin of the signal reported in their work.

The approach developed in this thesis builds on this concept by directly testing how plasmonic enhancement and emitter—collector geometry influence the emitted current under controlled experimental conditions. Measuring the emitted current as a function of wavelength and bias, and distinguishing between different field-assisted emission regimes, this study aims to clarify how nanoscale field enhancement can effectively drive electron emission in the infrared and to identify the dominant physical mechanisms responsible for the observed photocurrent.

3. Electron Emission Mechanisms for Infrared Detection

Electron emission is the core physical principle that these devices are meant to exploit for Infrared (IR) detection. Generally speaking, electron emission represents a fundamental process in vacuum electronics, photocathodes, and field-emission devices. Through electron emission mechanisms, it is possible to convert photons or other forms of radiation into electrical charge carriers, quantities easier to measure, manipulate, and process. This transformation of a radiation signal into an electrical current represents the base of almost every detection system, as it enables the information carried by electrons to be decoded, amplified, and processed using standard electronic circuits.

Different emission mechanisms can be observed in solids, such as photoelectric emission, thermionic emission and field emission. Other processes, such as secondary emission, can occur when impinging photonic particles cause an electron emission cascade in the device, but hold no relevant use for IR detection has been found and will therefore not be discussed further. The photoelectric effect, first described by Einstein, is governed by the relation:

$$E_k = h\nu - \phi \tag{3.1}$$

Einstein's law describes an incident photon, characterized by energy $h\nu$, interacting with a material of work function ϕ and producing an electron of kinetic energy E_K . For this phenomenon to occur, the photon energy has to be sufficient to overcome the material work function. In the infrared range, this is not the case for most metals and materials in general, due to the photon's reduced energy. Indeed, photons associated with the infrared spectrum have energies in the order of hundreds of meV, orders of magnitude too weak when compared to the several electron volts (eV) characteristic of most metallic work functions. Unless extremely low-work-function materials or engineered bandgap structures are involved, the photoelectric effect does not find a direct application in IR detection.

A different process is thermionic emission, described by the Richardson-Dushman law:

$$J = AT^2 \exp\left(\frac{-\Phi}{kT}\right) \tag{3.2}$$

Where J is the current density, A the Richardson constant, ϕ the work function, and T the temperature. This principle is particularly used in various electron

emission systems like hot cathodes and electron guns used in Scanning Electron Microscopy (SEM) and Transmission Electron Microscopy (TEM). However, it does not yield practical direct applications for IR detection. To obtain measurable currents, the system requires extremely high temperatures, often exceeding 1000 K, incompatible with deployable devices. Nevertheless, thermionic emission remains a central physical phenomenon for vacuum tubes, microwave sources, and cathode-ray technologies.

In general, IR detection is challenging due to its low photon energies, fractions of eV, while typical work functions are an order of magnitude higher. This difference makes direct photoemission impossible and calls for different operating principles like field-assisted mechanisms, such as Schottky emission and Fowler–Nordheim (FN) tunneling. At room temperature, materials with tunable low bandgaps can, in principle, extend sensitivity into the infrared; however, their performance is often limited by thermally generated carriers, which significantly degrade the signal-to-noise ratio unless the detector is sufficiently cooled. These processes rely not only on photon energy but also exploit strong electric fields to reshape or thin the potential barrier, enabling electrons to escape with lower energetic cost. This approach also paves the way for the natural integration with plasmonic effects, where the electric field enhancement and resonant absorption due to geometric structuring add extra degrees of freedom in the picture.

Fowler-Nordheim Tunneling

In Fowler–Nordheim (FN) tunnelling, the electrons tunnel through a potential barrier under the influence of high electrical fields. Under strong biases, the potential barrier is bent and acquires a triangular shape, facilitating the process of electron tunnelling from the Fermi level. As this is purely a quantum-mechanical effect, the weak IR photon energy does not go against the phenomenon requirements and the electron emission remains possible, however lower, even if the particle's energy does not exceed the work function of the material. Without photon-energy requirements, FN tunnelling represents an emission mechanism that allows exploitation of IR photons as modulators of tunneling probability rather than direct electron emission causes. In its standard formulation for a metal–vacuum interface, the photocurrent density can be described by:

$$J = \frac{A}{\Phi} E^2 exp\left(-\frac{B\Phi^{3/2}}{E}\right) \tag{3.3}$$

and, more explicitly in terms of bias:

$$I \propto \phi^{-1} \left(\gamma \frac{V}{d} \right)^2 exp \left(-b \frac{d\phi^{3/2}}{\gamma V} v(f) \right)$$
 (3.4)

where E is the local electric field, ϕ the work function, V the applied voltage, d the emitter–collector distance, and γ the field enhancement factor. It is evident from

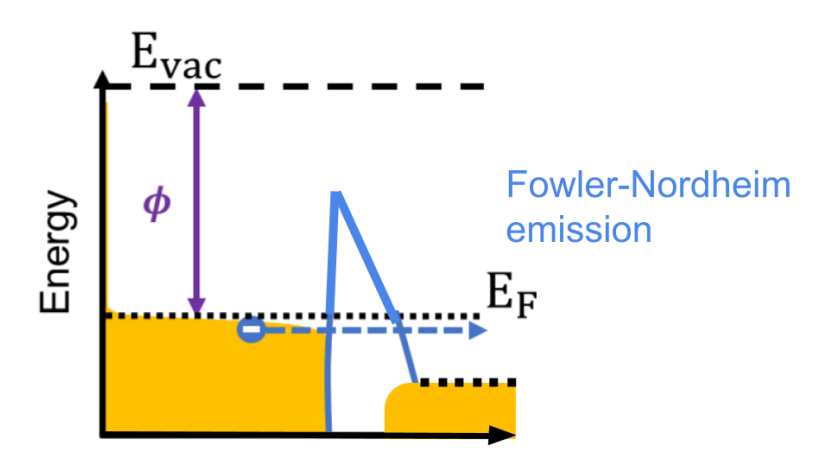


Figure 3.1: Schematic of Fowler–Nordheim emission. Under an applied bias, the electric field tilts the potential barrier at the emitter interface into a triangular shape, effectively reducing its width and height. Electrons near the Fermi level can quantum-mechanically tunnel across the barrier into the vacuum or opposite electrode, generating a current from source to drain. As the bias (field) increases, the barrier becomes narrower, enhancing the tunneling probability and leading to the characteristic exponential dependence of the Fowler–Nordheim current.

these relations that FN emission depends exponentially on the local electric field, making it highly sensitive to plasmonic field enhancement. In the case of plasmonic nanoantennas, localized surface plasmon resonances (LSPRs) enhance the electric field by several orders of magnitude in specific hotspots, increasing tunneling current and sensitivity. These nanoscale "hot spots" originating at antenna tips or gaps are by now well-established, and experimental works have demonstrated enhancement factors of several orders of magnitude in emission current in plasmonic structures. Bending the potential barrier through high electric fields makes this emission technique particularly viable for IR detection. It introduces several design degrees of freedom: antenna geometry, gap size, and resonance frequency, all directly influence field distribution and the FN tunneling current. Experimentally, the tunneling regime is often analyzed through an FN plot, where $\log(I)$ is plotted against 1/E, producing a linear trend characteristic of field emission.

Schottky Emission

Another key mechanism is represented by Schottky emission, also analyzed in this work. This effect occurs when an external electric field reduces the barrier height using image-charge attraction, effectively lowering the material's work function. As a result, electrons need less energy to escape.

This phenomenon, also referred to as field-assisted thermionic emission, is typically formulated for a metal-semiconductor interface, where the barrier lowering is described by:

$$\Delta\Phi = \sqrt{\frac{e^3 E}{4\pi\epsilon_0}} \tag{3.5}$$

The corresponding current density is given by:

$$J = AT^2 exp\left(-\frac{\phi - \Delta\Phi}{k_B T}\right) \tag{3.6}$$

and, in expanded form, the photocurrent can be written as:

$$I \propto T^2 exp\left(\frac{-\phi + q/2}{k_B T} \sqrt{\frac{q\gamma V}{d\pi\epsilon_0}}\right)$$
 (3.7)

where A is the Richardson constant, T the temperature, and k_B the Boltzmann constant [38]. This formalism shows how this effect can be seen as a field-assisted thermionic effect, as the applied electric field acts to lower the barrier and electron emission is exponentially increased.

This barrier-lowering picture is intuitive as it suggests that by applying an external bias, it is possible to relax the conditions around a material workfunction, effectively reducing the requirements on the electron energy to tunnel. The applied field acts as an external source to help the weak IR radiation energy promote an electron. Temperature plays a different role in the two phenomena, marking a crucial difference between the two. While FN tunnelling is considered to be largely temperature-independent, Schottky emission exhibits strong thermal dependence.

Particularly, this means that FN-dominated devices are not influenced by temperature fluctuations, while Schottky-based detectors might benefit from controlled heating or stable thermal control to be able to obtain repeatable emission currents. Because of this, Schottky emission can be engineered by performing thermo-electrical analysis and combining the two physical domains to increase efficiency. This distinction also implies different design processes, depending on the targeted emission regime. Experimentally, Schottky emission is often verified using a Schottky plot, where $\log(I)$ is plotted versus $V^{1/2}$. When represented in an FN plot, Schottky emission can sometimes appear deceptively linear, potentially leading to confusion between the two regimes. However, when analyzed in the appropriate Schottky configuration, their distinct behaviors become clearly distinguishable.

It is furthermore worth mentioning that a device rarely operates under only one of these regimes. More often, both mechanisms coexist and a device can be engineered to enhance one of the two. However, it will still undergo different phenomena at different operating conditions. It is the case for the nanoantennas proposed by Turchetti et al [38], a work previously carried out in the QNN group and considered to set the theoretical foundations for this project. At low biases, the device may exhibit Schottky-dominated behaviour, while at higher fields the emission gradually transitions to the FN regime, eventually reaching saturation.

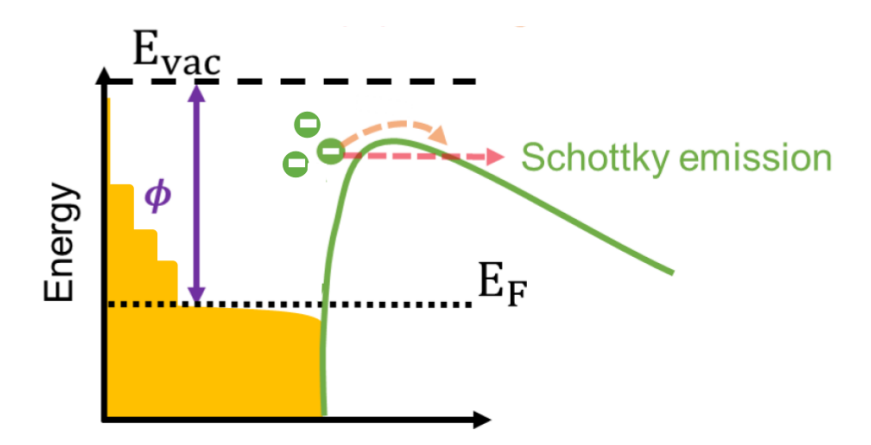


Figure 3.2: Schematic of Schottky emission mechanism. Under forward bias, the applied electric field at the metal—semiconductor interface lowers the potential barrier through the Schottky effect, reducing the effective work function. Thermally excited electrons with sufficient energy can overcome this field-lowered barrier and be emitted. The resulting current flows from source to drain and increases exponentially with temperature and moderately with the applied field. The barrier maintains a rounded profile, contrasting the triangular shape typical of Fowler–Nordheim tunnelling.

3.1 Application of Emission Regimes to Nanoscale Antenna Design

By examining the fundamental notions of electron emission theory and learning from existing work, the idea of a different approach to IR sensing can be investigated. The goal is to investigate both Fowler–Nordheim and Schottky emission mechanisms within the same plasmonic platform, evaluating whether either can deliver adequately high sensitivity ($\gg 10^8$ Jones) and fast response ($\tau \ll 10^{-3}$ s) while maintaining room-temperature operation.

The plasmonic antenna design, as already shown in the literature [37], presents sensitivity in the infrared portion of the spectrum but leaves room for improvement if the geometries were tailored for a different target emission regime. By reengineering these geometries for infrared wavelengths and carefully separating the two emission regimes, this work aims to clarify the physical origin of photo-emission in plasmonic detectors and guide their optimization toward true IR sensitivity.

This thesis builds on previous works found in the literature, with special attention to the analysis of the device proposed by Piltan et al. [37]. The device at issue consists of a periodic array of metallic triangular-shaped nanoantennas designed to support plasmonic effects, especially Localized Surface Plasmon Resonances (LSPRs). The geometry exhibits field enhancement, reaching factors up to 700x in

the region corresponding to the tip of the triangle, with resonance at a wavelength $\lambda=785$ nm. The array stretches out on 40*40 unit cells, each one ~ 400 nm wide, ~ 200 nm long along the tip axis, and ~ 130 nm tall, separated by a ~ 50 nm vacuum gap. The structure was fabricated on a thermally grown SiO_2 on a high-resistivity Si substrate. The arrays were tested under a bias DC voltage in the order of 10 V and exposed to optical radiation at the resonance matching wavelength. In the setup described by Piltan et al., a power density ranging in the hundreds of $[Wcm^{-2}]$ was achieved, and the photocurrent measured by the device was in the μA range. In their work, the authors state that the results can be interpreted through Fowler-Nordheim (FN) field emission theory as shown by an approximate linear behaviour of the I-V characteristics when analyzed on a FN plot (Chapter 3).

A later study from Turchetti et al. [38] shows that electron emission in the gap of such systems is the result of a combination of different emission regimes, and that linear behavior in a FN plot is not often enough to confirm operation in the true FN regime. This interpretation also highlights that the large field-enhancement factors often required to justify an FN fit, sometimes exceed physically realistic values and can lead to misidentification of the underlying emission regime. To demonstrate this, the geometry under analysis was changed in favour of a planar bowtie geometry, realized in both Au and TiN. Testing these devices, three different regimes are identified: Schottky emission seems to dominate at lower applied bias, Fowler-Nordheim (FN) rules emission at higher biases, until a saturation regime is reached for higher values of current. This last regime has been associated with space-charge saturation, widely analyzed in vacuum literature by the Child-Langmuir law [39].

It was possible to identify the three different regimes in the I-V characteristic curves by the different dependencies of the photocurrent. The Au devices show evidence that the dominant behaviour at the previously mentioned range of applied bias is a Schottky emission phenomenon. Moreover, these new analyses indicate a simultaneous field enhancement factor \sim 7-10x, a more realistic value when compared to the field enhancement required by FN fit (>50x).

To be able to distinguish between the two regimes is of fundamental importance, as it unveils the possibility of improving device performance by leveraging the dependencies of each phenomenon on influencing factors. The critical difference in temperature dependence of the Schottky emission photocurrent with respect to the FN photocurrent, as highlighted in Chapter 3, for instance, can be taken into account in the design phase of a IR photodetector structure, where the device can be engineered in such a way that the emitter-collector channel is placed at the area of greatest anticipated heat buildup on optical absorption to achieve the greatest optically-induced perturbation of the electron emission across the channel.

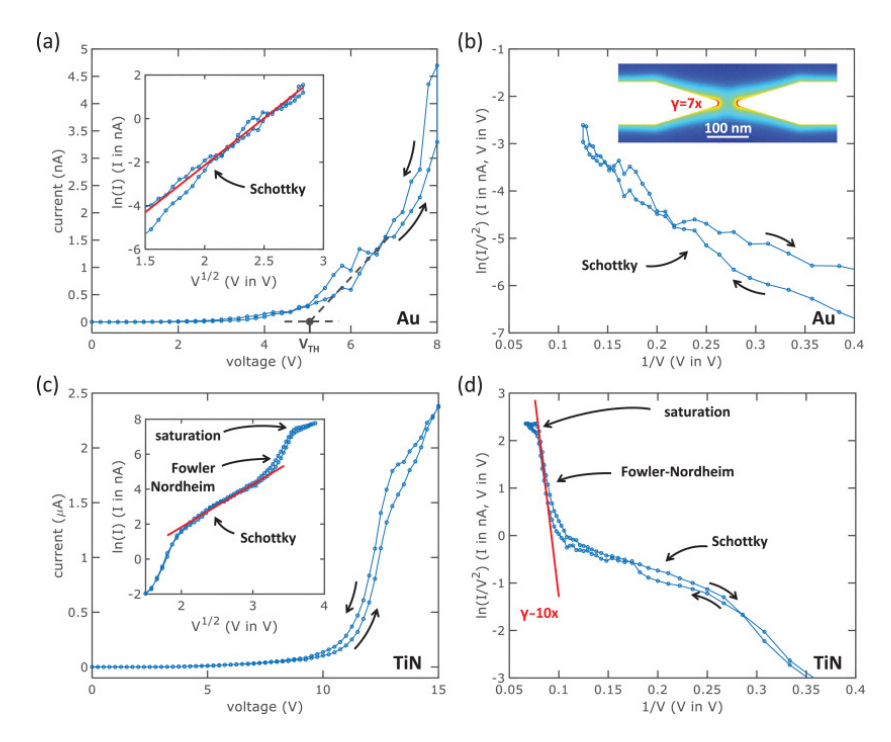


Figure 3.3: Taken from [38]. I–V characteristics of Au and TiN devices. (a) experimental sweep with inset $\ln(I)$ vs $V^{1/2}$ plot (Schottky plot) showing Schottky behavior. The turn-on voltage V_{TH} is extracted from the tangent at 1 nA. (b) data in $\ln(I/V^2)$ vs 1/V (FN plot) form highlighting FN behavior. The inset shows a 3D simulation of the field enhancement ($\gamma \sim 7\times$ at the tip). FN fitting would require $\gamma \sim 50\times$, inconsistent with simulation. (c) TiN device with inset Schottky plot, displaying a linear regime followed by superlinear growth and saturation. (d) TiN FN plot confirming that the superlinear regime arises from FN emission, fitted with $\gamma \sim 10\times$, consistent with simulation. Measurements performed at 10^{-6} mbar.

Implications for IR Detector Operation

Crucial to the success of this project is the correct identification of the physical regime that governs the optically-excited electron emission phenomenon; on that basis, different geometries have been analyzed in further stages of the project. These new geometries can be generally divided into two categories. Half of them kept minimal changes with respect to previous designs and aimed at setting a reference and direct comparison with Fowler-Nordheim-based systems. The new geometries have been developed to take advantage of the temperature dependence of the photocurrent as expected in a Schottky emission-regime-based device. The general idea was to replicate the same baseline geometries and, by introducing only minimal modifications, enhance the temperature role in the emission process. For the emission-oriented devices, two geometries have been designed. The first one, used as reference, consisted of a triangular-shaped nanoantenna, where slight modifications were the aspect ratio was slightly modified. The second chosen geometry was a nanorod-based antenna design, chosen because of its well-known plasmonic properties, and characterized by high performance combined with ease in fabrication. The Schottky-oriented designs were modified to better perform when exposed to temperature-dependent phenomena, with respect to their field-emission counterparts.

As highlighted by Turchetti et al.[38], Schottky emission has a squared dependence on the temperature (due to the prefactor T^2) and a T^{-1} dependence in the exponential; unlike Fowler-Nordheim emission, which is not strongly temperature dependent Chapter 3. The Schottky photocurrent can be modeled as [38, 40, 41]:

$$I \propto T^2 exp\left(\frac{-\phi + q/2}{k_B T} \sqrt{\frac{q\gamma V}{d\pi\epsilon_0}}\right)$$
 (3.8)

while an analog model for FN would be [38, 42]:

$$I \propto \phi^{-1} \left(\gamma \frac{V}{d} \right)^2 exp \left(-b \frac{d\phi^{3/2}}{\gamma V} v(f) \right)$$
 (3.9)

A deeper example of the temperature effects is represented by the work conducted by Hobbs et al [43]. By exposing plasmonic nanorods embedded in two different resists, it is possible to distinguish two different emission mechanisms. In PMMA, the resist exposure coincided with plasmonic resonances and field hotspots induced by LSPRs. Performing the same experiment in hydrogen silsesquioxane (HSQ), a negative-tone electron-beam resist, additional exposure areas were observed at the center of the nanorods. The position of these additional developed spots does not coincide with optical field enhancement but matches the thermal hotspot predictions. This suggests that a thermally induced "hot electron" emission can occur, without the support of a plasmonic-induced field enhancement. It is also possible to exploit these thermally induced charges for optical detection purposes,

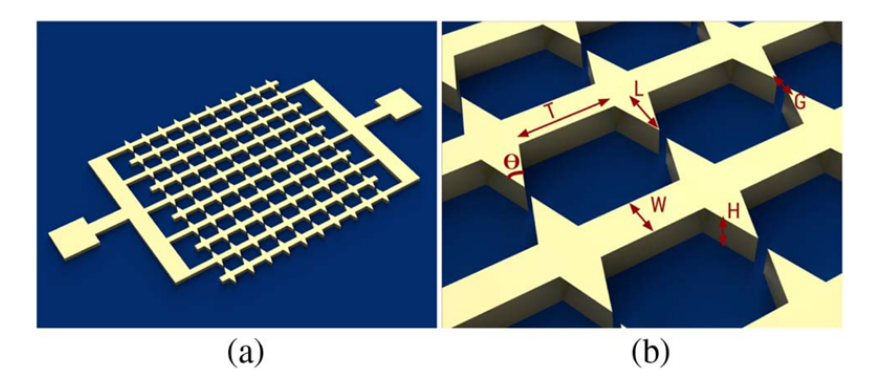


Figure 3.4: Figure adapted from [37]. Geometries from Piltan et al., used for comparison. (a) 3D rendering of the patterned array with busbars/contact pads. (b) Parameterized unit cell with definitions used in design and simulation: T (lattice pitch), L (arm length), W (arm width), H (notch depth), G (gap), and θ (tip angle).

as it has been proven by Chalabi et al., showing that they can take advantage of similar mechanisms in gold nanostripes [35].

Combining this rationale with the Schottky framework, new antenna geometries were developed to take advantage of structural thermal hotspots. The new structures were created to closely resemble their field-emission counterparts, while also presenting minimal changes to target hot electron detection. The nanorod-based geometry is naturally fitted for this aim, as a simple repositioning of the collector element is the only modification needed. Instead of the classical placement near the nanorods' extremities, as is the case for FE geometry, the collector was placed near the center of the antenna, where a thermal hotspot is created. In the triangular case, the geometry required deeper modifications. Since a thermal hotspot was not accessible for a collector placement, a bowtie configuration has been developed instead, by connecting two mirrored triangles along their tip axis.

The theoretical insights presented here guided the structural design of the proposed plasmonic detectors. Building on these considerations, the following Chapter 4 describes the actual implementation of these concepts, illustrating geometry optimization, simulation, and nanofabrication of the detector structures.

4. Design and Nanofabrication of Plasmonic Detector Structure

Building upon the theoretical framework established previously, this chapter focuses on the application of those concepts into practical device architectures. It describes the rationale behind the geometric choices, the multiphysics simulations used to optimize them, and the nanofabrication strategies implemented to realize the plasmonic detector structures.

4.1 Geometry Concepts and Design Rationale

During the design process for the different geometries, the physical dimensions of the elemental cell required deeper analysis; particularly critical was the dimension relative to the gap between the antenna and its collector. A small emitter-collector gap facilitates electron collection, allowing for a more efficient device. However, Fowler-Nordheim emission experiences a stronger influence of the gap size with respect to Schottky emission. While FN dependence is exponential, as explicitly formulated in the photocurrent model (eq. (3.9)), Schottky-induced current is weakly modified through the potential barrier term (eq. (3.8)). Both benefit from a gap size reduction, allowing higher efficiency and photocurrent; Schottky emission withstands a slightly larger tolerance to this dimension when compared to FN. Obtaining an extremely small gap was the most challenging phase and required several iterations and fabrication attempts. While the design pushed this dimension down to 20nm, thanks to fabrication processes tuning, an array containing consistently sub-5nm gaps has also been created.

Each antenna geometry was designed to target a specific emission regime and to provide a direct comparison between field-assisted and thermally assisted electron emission. Triangular antennas, which closely resemble the geometries reported by Piltan et al., were retained as Fowler–Nordheim (FN) references. Their sharp tips and narrow collector gaps favor strong local electric fields, allowing field emission to dominate under bias. These structures are expected to show temperature-independent behavior and serve as a benchmark for purely field-driven operation. Nanorod-based antennas were selected as a second reference geometry because of their well-established plasmonic response and simpler fabrication. In

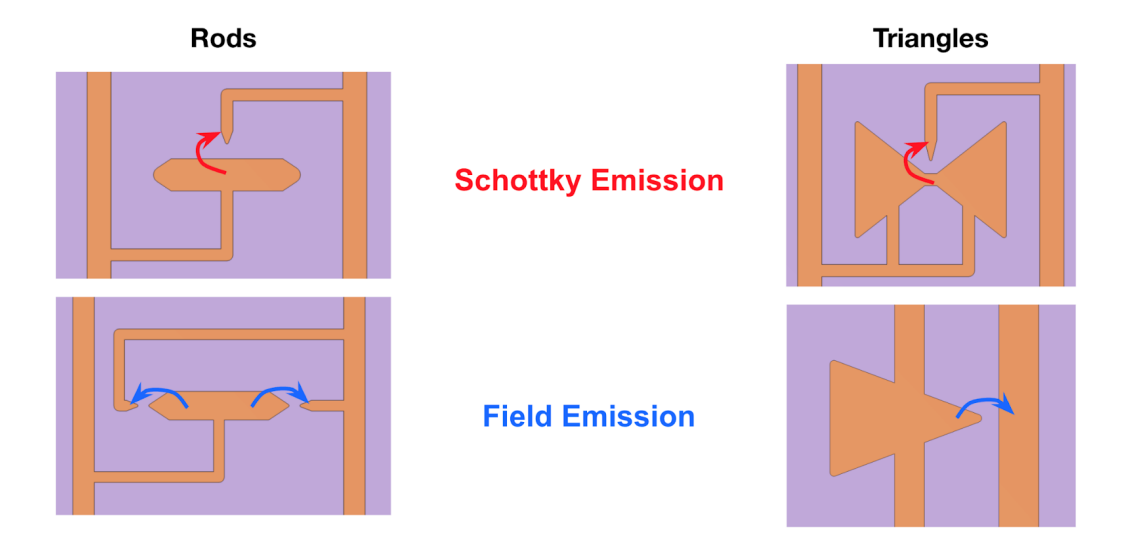


Figure 4.1: 2D design layouts of the antenna geometries. Planar masks for bowties, nanorods, Schottky nanorods, and triangular antennas define the nominal length, aspect ratio, and gap used for fabrication and simulations. Top row (Schottky devices): unlike prior work, the electron-emission channel (metal-semiconductor junction) is intentionally placed at the point of highest thermal buildup (plasmonic hot spot) rather than at the point of highest field enhancement; this targets thermally assisted Schottky emission under optical heating.

their standard configuration, the nanorods behave as efficient field emitters, with localized surface plasmon resonances (LSPRs) concentrated near the extremities, reinforcing FN-type tunneling across the adjacent gap. For the Schottky-oriented configuration, the collector was repositioned toward the center of the nanorod, coinciding with the predicted thermal hotspot. This modified layout is designed to exploit the local temperature rise under illumination to modulate the emission probability of electrons into the emitter, thanks to its placement. Bowtie antennas, finally, were designed to maximize the thermal coupling effect in planar geometries. By mirroring two triangular elements tip-to-tip, the bowtie configuration aligns the emitter–collector gap with the region of strongest Joule heating during optical excitation. This geometry is expected to operate primarily in the Schottky regime, with a measurable temperature dependence of the photocurrent. Comparison between geometries allows a systematic isolation of field-driven versus thermally driven contributions, establishing a direct link between geometry, local field distribution, and detector performance.

4.2 Multiphysics Simulation and Field Analysis

AS the geometrical parameters influencing the plasmonic and thermal response of the device required careful refinement, multiphysics simulations were used to define the design dimensions. The new phase of the project involved experiments where the optical excitation wavelength was tuned to be closer to the intrinsic resonant frequency of the nanoantenna geometry. Since the ultimate goal of the project was to achieve Mid-wavelength (3-5 μm) and Long-wavelength (8-14 μm) Infrared detection, the antennas were defined to match a target frequency within this range, while simultaneously maximizing the thermic response, especially for Schottkyoriented designs. To analyze the interaction between thermic and plasmonic properties, multiphysics simulations were carried out on the different designs. Computer-aided electromagnetic simulations determined local field enhancement and thermal hotspot intensity, and locations under planar wave illumination. A Python-based script created a GDSII file for fabrication steps (Section 4.3) and parametrised COMSOL geometries, then automatically placed them in already embedded surroundings and boundary conditions. Parametric sweeps, mainly one of the antenna dimensions (i.e., length), have been conducted to find the best fit for geometry parameters. They targeted the best unit-cell dimensions to maximize simultaneously electromagnetic and thermal response. At a given length dimension, a broad analysis has been conducted on wavelength and aspect ratio. While the aspect ratio allowed for the control of the other geometrical dimensions, the gathering of data for different wavelengths allowed identification of the resonance peaks of the antennas. Two-dimensional plots were extracted from the simulations (Figure 4.2), highlighting peak values of field enhancement γ and temperature in the unit cell. Each one of these two components was necessary to not only optimize design in the two emission regimes, but also to be able to accurately fit the two photocurrent models and estimate device performances.

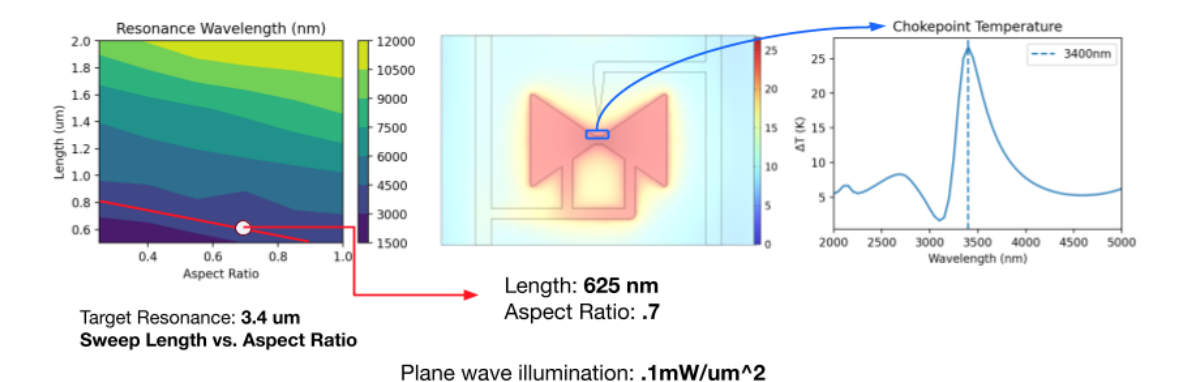


Figure 4.2: Example of the design flow. From the 2D resonance plots discussed in Section 4.2, a target resonance is chosen, which fixes the required antenna length and aspect ratio. The corresponding geometry is then built in COMSOL. Thermal simulations of this design give access to the local temperature distribution, highlighting the choke-point temperature at the gap and the position of the thermal hotspots across the structure. This sequence illustrates how optical design and thermal analysis are combined in practice to guide device optimization.

While the temperature registered was relative to the allegedly hotspot of the geometry, it also corresponded to the peak temperature reached by the geometry, further confirming the hotspot presence. By cross-analyzing γ and ΔT , it was possible to create color-coded maps to indicate the best aspect-ratio and wavelength combinations to maximize both effects at resonance frequency.

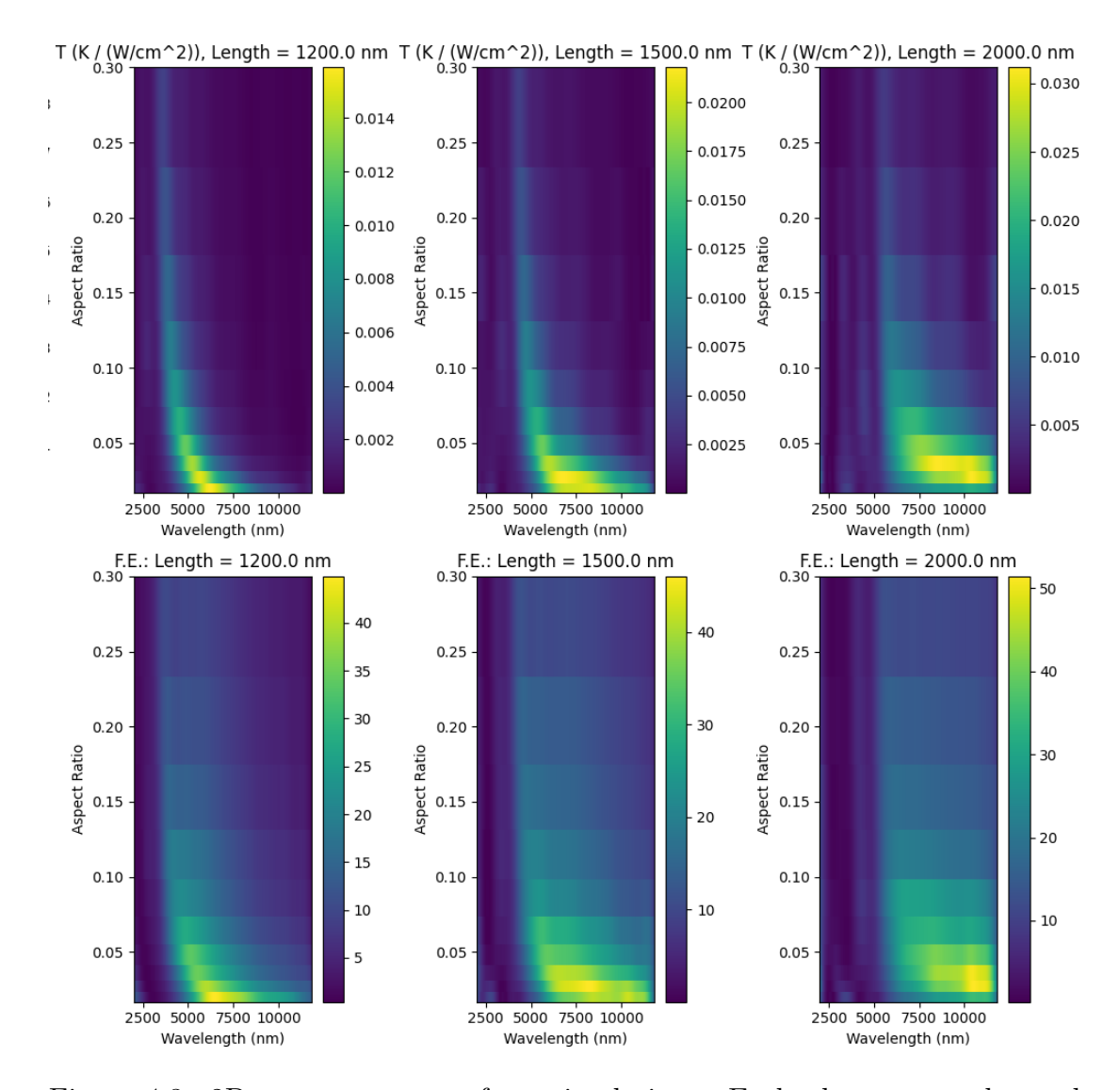


Figure 4.3: 2D resonance maps from simulations. Each plot reports the peak temperature and field enhancement factor as a function of antenna length and aspect ratio. The maps allow us to identify the geometrical parameters providing the desired resonance and quantify the expected local field enhancement at the gap. These plots represent the starting point for geometry selection, later transferred to COMSOL for full 3D geometry and thermal simulations.

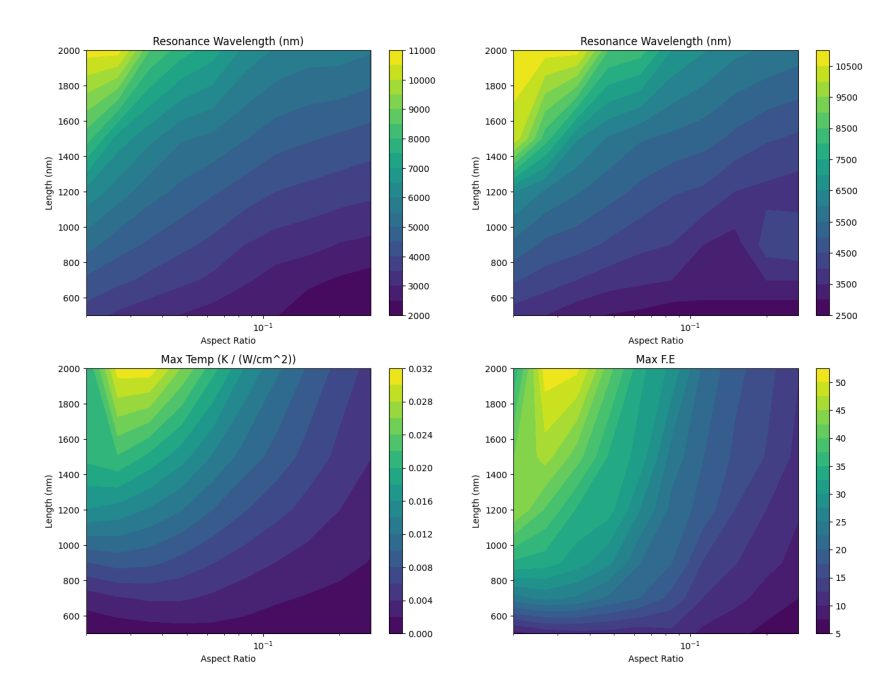


Figure 4.4: Design maps correlating resonance wavelength, field enhancement, and thermal response. The top panels show the simulated resonance wavelength as a function of antenna length and aspect ratio. Complementary maps report the maximum local field enhancement (FE) at the gap and the corresponding choke-point temperature under illumination. Superimposing these maps highlights regions in parameter space where the optical and thermal constraints are simultaneously satisfied. They are used in the design step to provide for length—aspect ratio combinations that provide the targeted resonance wavelength together with high FE and controlled temperature rise, defining the optimal parameters window for fabrication.

These preliminary simulations and design work were carried out by Malick Sere and other colleagues at the QNN group at MIT and at MIT Lincoln Laboratory facilities. The design and subsequent fabrication processes were closely followed by experimental characterization to complete the feedback loop and move towards a feasible, working device.

4.3 Nanofabrication Process

After the design stage produced a set of nanoantenna geometries with the intended properties suited for this project, the fabrication process was initiated. Fabrication represented a key experimental step as it allowed the project to transition from a theoretical concept to a functional device. This section illustrates the fabrication process adopted for the realization of the proposed devices, analyzing materials, techniques, and challenges of the workflow.

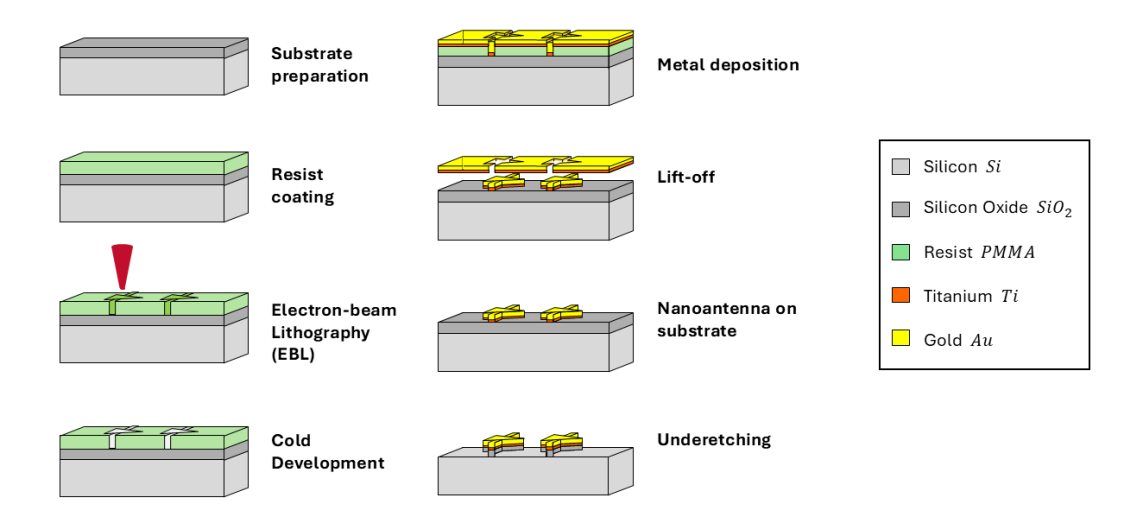


Figure 4.5: Schematic cross-section illustrating the main steps of the fabrication process. The sequence includes substrate preparation, resist coating, electron-beam lithography and development, metal deposition, and lift-off. Subsequently, an optical lithography process is performed to define contact pads on the nanoantennas (not shown here). The final step consists of the underetching of the oxide layer, which releases the structures and reduces dielectric charging effects.

The choice of materials and methods was critical, as the optical and electrical nanoantenna properties are extremely sensitive to both geometry and dimensions. That means that small deviations fundamentally alter the response of the device and its physical behavior. Historically, fabrication protocols and developed within the group for previous nanoantenna devices that employed glass substrates. This choice was mainly imposed by the need to perform experiments in both reflection and transmission modes. However, this project had different requirements. The need for plasmonic field enhancement steered the choice towards a silicon-based substrate, while electrically insulating the antennas through a silicon oxide layer. The final substrate consisted of thermally grown SiO_2 (~ 110 nm) on a silicon wafer. The previously described substrate was initially diced into $1x1cm^2$ square chips to be processed individually. After cleaning in solvents and piranha solution, fabrication proceeded to the electron-beam lithography (EBL) stage. Given the nanometric scale of desired features, the lithography step could not involve the use of a physical mask but rather required direct writing exposure. To be able to develop such small features, diffraction-limited optical lithography does not represent a viable tool as it does not present the required resolution. Indeed, EBL enables sub-50 nm features given electrons sub-angstrom characteristic wavelength, beyond the optical diffraction limit. The nanoantenna arrays were then patterned by electron-beam lithography, a technique that employs a focused electron beam of electrons instead of light to expose a previously applied radiation-sensitive resist. The resist used was polymethyl methacrylate (PMMA), a positive-tone resist widely adopted for nanofabrication. When exposed, PMMA undergoes chain

scission, and exposed regions in the developer are removed thanks to their increased solubility.

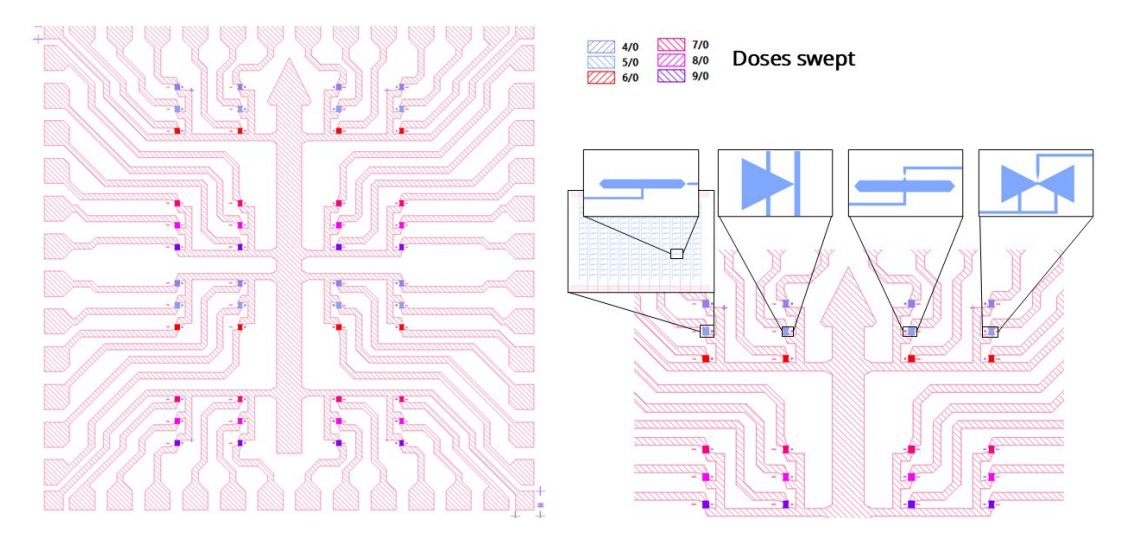


Figure 4.6: Layout view from the GDSII design file. Different colors indicate the swept electron-beam doses used for the fabrication of the antenna arrays. The image also shows the overall contact pattern providing electrical access to the devices. Insets give a magnified view of the arrays, highlighting the individual geometries defined within each block.

The exposed PMMA was developed using a cold-development process, where the developer solution was cooled to approximately $0-5^{\circ}C$ to enhance resolution and minimize resist swelling. This approach is known to improve contrast and reduce line-edge roughness, allowing sub-10 nm features to be resolved [44]. In our case, a standard MIBK:IPA (1:3) developer was employed without the addition of methyl ethyl ketone (MEK), which has been reported to accelerate dissolution in similar processes. Although the absence of MEK slightly limits the development rate, it also preserves a more controlled and reproducible dissolution front, potentially improving gap definition at the smallest scales.

Although EBL provides finer and more detailed patterns to be printed, it also presents several drawbacks. The ability to directly write on the resist, eliminating the use of a hard mask, requires careful tuning of additional parameters, such as charging mitigation, alignment, stitching, and exposure dose. Since the substrate is insulating, charging has to be mitigated using a thin conductive film applied on top of the resist. Alignment and stitching represent common problems, autonomously compensated by the tool's software. However, some related problems, not correctly handled by the software, are quite common. Dose calibration and proximity correction require empirical optimization to avoid overexposure or underexposure. A common method employed to determine optimal settings consists of performing dose-matrix tests, sweeping different values, and evaluating resulting patterns under SEM. While the first fabrication run explored four doses without an optimal point,

the second run managed to successfully identify ideal parameters for each geometry. In some cases, a slight overexposure was intentionally applied to fine-tune the antenna gap size, as the optimal dose varies between geometries.

The main limitation in Electron Beam Lithography is represented by the proximity effect, causing most of the undesired effects and artifacts. This effect occurs from the tail of the Gaussian electron beam, broadens on the resist, and overlaps with features from nearby printed features. By exceeding the resist exposure limit it exposes unwanted areas and modifies the printed pattern. This effect can be mitigated using proximity effect correction (PEC) software, in this case, Beamer. PEC involves different strategies, such as a non-uniform dose modulation, geometrical compensation, or a hybrid approach known as Over-Dose/Under-Exposure (ODUS). In the first fabrication run, a simple variable-dose correction was applied, whereas in the second, a complete PEC strategy including ODUS was implemented. Despite its increased complexity, EBL remains the most effective technique to realize sub-50 nm features as required by the nanoantenna design.

After exposure, the next step consisted of metal deposition. Among commonly widespread Physical Vapor Deposition (PVD) techniques, mainly represented by evaporation and sputtering, the former was employed in this process. In thermal evaporation, a metallic source is resistively or electron-beam heated under high vacuum until atoms sublimate and condense on the substrate, forming a thin metallic film. This method provides high-purity and smooth layers, particularly well suited for nanofabrication processes where step coverage is less critical than surface quality. Using evaporation, 3 nm of titanium (Ti) and 20 nm of gold (Au) were deposited on the patterned substrate. The Ti layer acted as an adhesion promoter between SiO_2 and Au, preventing film delamination during processing. Following deposition, lift-off was performed to remove excess metal and define the nanoantenna structures. Thermal evaporation is advantageous for lift-off because of its highly directional deposition, which minimizes sidewall coating and facilitates resist separation. This approach produced uniform, well-defined metallic features, although film adhesion and edge continuity required optimization during early fabrication runs.

The lift-off process offers a safer and cheaper solution, eliminating the need for exposure of the chip to an acidic element. This approach enables the removal of multilayer structures deposited on thick resist (>2m). However, mechanical lift-off can cause bridging artifacts, especially when metal films remain continuous across narrow gaps. This effect may be partially mitigated by the resist choice, as Image Reversal resists are known to suffer less from this effect. These defects were observed during the first fabrication run but were largely mitigated in the second run, where improved film uniformity ensured clean pattern definition.

After successful deposition of the gold nanoantennas, the chips were inspected

by SEM. Devices presenting promising small nanogaps proceeded to the contact metallization step. The contact layout pattern used has been historically in the group and features a common ground bus, connecting all devices through an arrow-shaped structure, while separate contact pads are used to connect individual emitter terminals. Given the larger feature sizes, contacts were patterned using optical maskless lithography instead of EBL. The contact deposited presented a 40 nm Cr adhesion layer followed by a 100 nm Au layer, providing a thicker base for the pad wire bonding procedure and minimizing the possibility of punch-through.

The following underetching step proved crucial to suppress undesirable charging effects given by the oxide layer. As previously mentioned, the need for this process is given by strong hysteresis appearing in current–voltage (I–V) curves, attributed to charge trapping and release within the SiO_2 layer. As trap states present characteristic lifetimes, this effect causes some spurious low-frequency signal noise. Previous works highlighted how this behaviour can be mitigated by removing the oxide layer, significantly reducing hysteresis.

The previous etch recipe involved a Reactive Ion Etching (RIE) step to initiate the oxide undercut, followed by an isotropic Buffered Oxide Etch (BOE) for the lateral recess. This combination creates a predominant vertical etching while also creating some lateral additional space between the oxide walls, increasing their distance and the probability of charges getting trapped in the oxide rather than travelling directly to the collector.

RIE is a directional etching method used to provide highly anisotropic structures exploiting a directional ion etching bombardment, creating vertical sidewalls characterized by high slopes. Sputtering reactive species combined with high accelerating voltages, it is possible to create extremely directional etches tailored to each process by modifying multiple parameters, such as the gas chemistry, flow rate, chamber pressure, and bias voltage. Buffered Oxide Etch, on the other hand, is a wet chemical etch, creating highly isotropic features due to its purely chemical mechanism. It is diffused because of its extremely selectiveness for SiO_2 , while leaving Si structures intact. Main parameters to tune in this process are represented by concentrations and etching time. The strategy was therefore to combine the anisotropic RIE with isotropic BOE, realizing a predominantly vertical etch with some lateral recess.

The target was to be able to etch 110 nm of SiO_2 on a Si substrate, preserving surrounding structures composed of 4 nm of Ti and 20 nm of Au. Initial tests with high-energy RIE severely damaged the gold, confirmed by SEM imaging. Subsequent low-energy RIE was introduced, but further analysis showed partial gold erosion, despite reduced ion energy. Some of the processed chips presented damage to the point where no conductive film was present on the arrays. The process employed a SAMCO SiO_2 -SEL recipe (100 W ICP, 50 W bias), yielding an estimated etch rate of $28nmmin^{-1}$. After 210 s of etching, only ~ 10 nm of

oxide remained, but the gold film was almost completely removed. A trade-off was then adopted, exposing some of the processed chips to a reduced RIE step with etch time down to 105s. This showed to have left a significant amount of SiO_2 layer without significantly damaging the gold structures. Future fabrication runs plan to introduce a hard mask element made out of nickel (Ni) to protect the gold during the process, removable afterward. In parallel, wet etching tests were conducted on experimental chips. Tuning BOE concentration and etch time, partial underetching was obtained without gold structure collapse. A formulation of 9:1 deionized water (7:1 BOE) was used. The process reported a leftover ~ 80 nm layer of SiO_2 without evident damage to the nanoantennas. Although these results were promising, the process still requires further tuning to successfully combine both etches into a consistent and reproducible hybrid recipe. Even if partially etched chips allowed for the project to transition into the testing phase, this step remains the main bottleneck of the fabrication flow and will be carefully refined in the next runs. An extremely interesting case study came from a chip that underwent both BOE and, subsequently, RIE. The first wet etch process overetched the oxide, causing some damage to some structural elements, as it collapsed overlying gold lines due to their thinner dimensions. As this caused the chip to be electrically unusable while presenting a good gold film quality, it was processed using RIE as well. SEM analysis revealed that RIE had severely damaged the gold, leaving only residues corresponding to the antenna edges. A detailed discussion and corresponding SEM images are presented in Section 4.4.

4.4 Characterization via SEM Imaging

To verify the fabrication results and measure the printed features, the characterization has been performed using a scanning electron microscope (SEM). The SEM system exploits electron interactions with the sample rather than light, enabling imaging with a nanometric resolution, much higher with respect to optical microscopy techniques. Since it is able to provide imaging with a large depth of field, high resolution, and high magnification range, it represents one of the most useful tools in research and development. The system is composed of a vacuum column (down to 10^{-8} mbar) to avoid unwanted scattering of the electrons; an electron gun acts as source, electromagnetic lenses are responsible for the beam collimation and focusing, and a deflection system raster the beam across the sample.

Several detectors are placed in the vacuum chamber to collect signals coming from different interaction mechanisms. The base principle of this technique is the electron beam penetrating the sample and creating an excitation region, known as the interaction volume. Given that generally this area has a tear drop shape, its dimensions depend on the beam acceleration voltage and the atomic number of the specimen, whose combination can lead to a more surface-sensitive analysis in

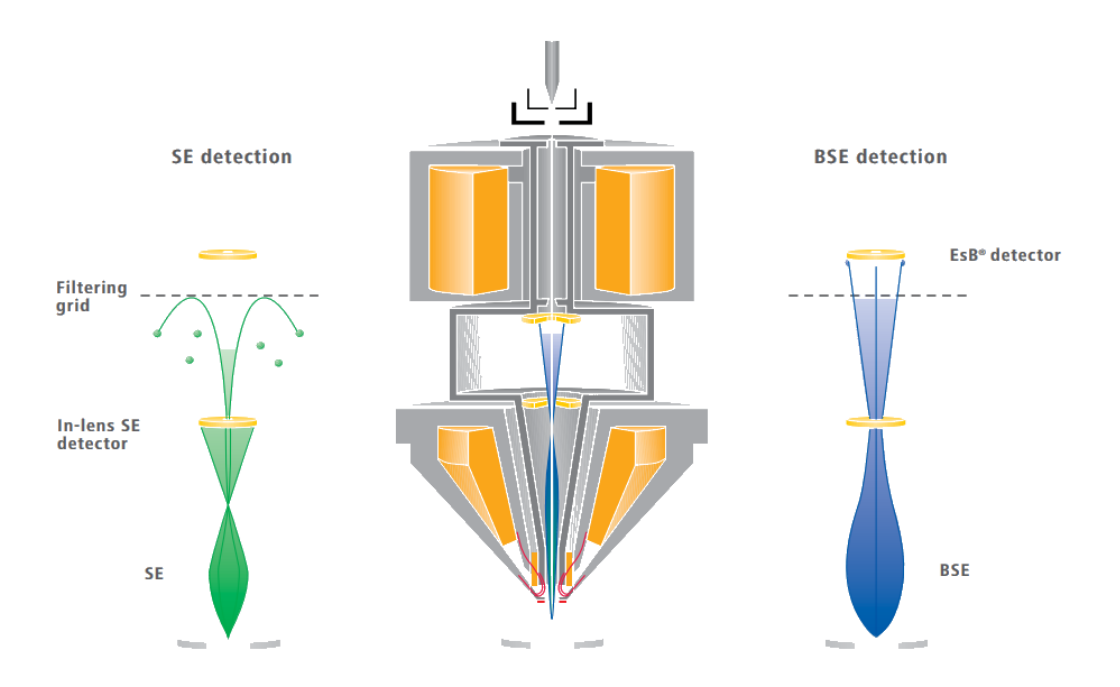


Figure 4.7: Figure adapted from [45]. Schematic representation of a scanning electron microscope (SEM) column and signal detection geometry. The diagram shows the focused primary electron beam interacting with the specimen surface, along with the typical configuration of detectors for secondary electrons (SE) and backscattered electrons (BSE). The insets illustrate how SEs, emitted from near-surface regions, are collected for topographical imaging, while BSEs, scattered from deeper within the interaction volume, provide compositional contrast.

the case of heavier elements and lower voltages, while higher voltages and lighter elements produce a deeper interaction.

The signal generation, and therefore the image formation, depends on the type of interactions with the sample, mainly elastic and inelastic scattering events. Elastic scattering involves a deflection of the incident beam by the specimen's atomic nuclei or core shells with negligible energy loss. Electrons experiencing large scattering angles (>90°) preserving high energy are detected as backscattered electrons (BSE). Inelastic scattering is characterized by a substantial energy loss due to transfer to atoms; the amount of energy transferred depends on the specimen energy levels. Whenever this energy causes an ionization of the sample and emission of lower-energy secondary electrons, those are detected as secondary electrons (SE). As different regions within the interaction volume generate different signals, the main signals are considered to be represented by Auger electrons, backscattered electrons, secondary electrons, characteristic X-rays, and continuum X-rays (Bremsstrahlung). Even if the volumes change with respect to the specimen and the acceleration voltage, it is possible to establish some baseline indicative

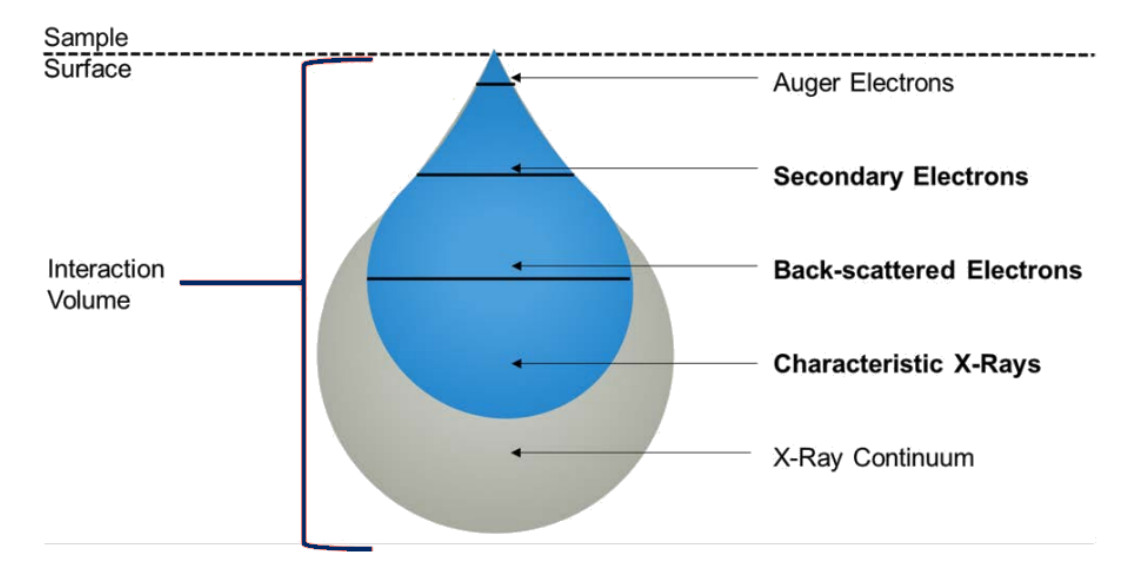


Figure 4.8: Figure adapted from [45]. Schematic representation of the electron–matter interaction volume in a scanning electron microscope (SEM). The diagram highlights the spatial regions from which different signals originate: Auger electrons are generated very close to the surface, secondary electrons (SE) arise from shallow depths and provide topographic information, backscattered electrons (BSE) emerge from deeper regions and carry compositional contrast, while characteristic X-rays and continuum (Bremsstrahlung) X-rays originate from the entire interaction volume. The overall shape and depth of this volume depend on the accelerating voltage and the atomic number of the specimen.

depth for each signal source: ~ 1 nm for Auger, $\sim 5-50$ nm for SE, $\sim 1-2\mu m$ for BSE and $\sim 2-5\mu m$ for characteristic X-rays.

Imaging was important to confirm good deposition of the metals, to verify and measure the gaps between the emitter and collector, whose importance was already established in Section 4.1. For this purpose, SEM signals from different detectors were analyzed and compared. Within the MIT.nano facilities, imaging was performed primarily with a Zeiss Sigma HD VP SEM and a Zeiss Gemini 450 SEM. The first one is equipped with an Everhart Thornley Secondary Electron Detector, an Inlens Secondary Electron Detector, and an Inlens Energy Selective Backscattered Electron Detector (EsB); it can perform analysis in High Vacuum (HV) mode as well as Variable Pressure (VP) mode between 5 – 30Pa. The second one is equipped with an Everhart Thornley Secondary Electron Detector, an Inlens Secondary Electron Detector, an Inlens Energy Selective Backscattered Electron Detector (EsB), a High efficiency Variable Pressure Secondary electron Detector (VPSE), an Angular selective Backscattered Detector, an Annular STEM Detector (aSTEM4), and an Oxford AZtec 100 EDS Detector; it can perform imaging in High Vacuum (HV) mode, Variable Pressure (VP) mode with partial pressure between 5 – 30Pa and Nano VP mode, an enhanced VP mode with an inserted Beamsleeve

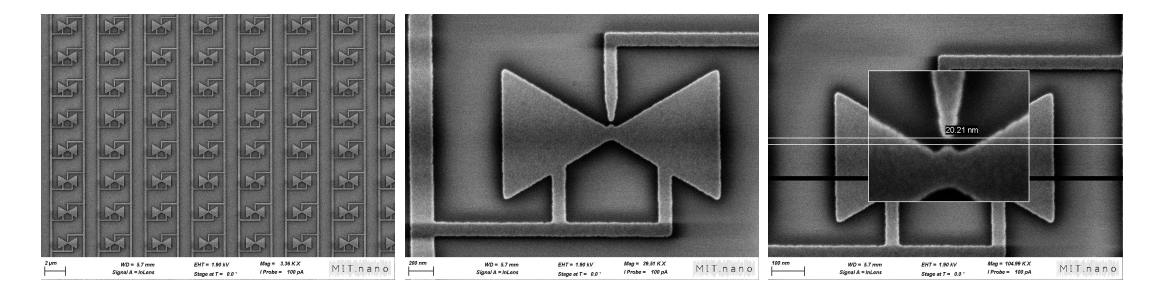


Figure 4.9: InLens SEM images of a bowtie antenna array at increasing magnification. The sequence shows the overall array layout and progressively zooms in on a single device. In the highest magnification image the antenna tips are resolved, revealing a gap of about 20 nm.

aperture below the objective lens allowing for a partial pressure between 5 – 150Pa (350 μm Beamsleeve aperture) or 5 – 40Pa (800 μm Beamsleeve aperture).

InLens detection proved to be especially useful as it provides high-resolution topographical information with enhanced surface sensitivity. It works by gathering signals from secondary electrons generated close to the surface, with relatively low energy, and guided by strong electric and magnetic fields inside the column directly towards the detector. Due to this selective collection of surface-emitted electrons, the signal is sensitive to nanoscale details, edges, and sharp features, thus enabling to resolution of fine morphologies. The InLens detector is integrated coaxially within the electron column and relies on the beam's immersion lens to accelerate and direct the electrons upwards, while filtering out most of the wide-angle, low-energy background. The sensitive section consists of a scintillator such as a photomultiplier or a solid-state-based element that generates a current signal upon electron impact. Given the peculiar position of this detector, usually closer to the electron beam impact point than any other detector, it provides crisper images with higher contrast when compared to conventional Everhart–Thornley or Secondary Electrons of type 2 (SE2) detection.

This type of analysis was especially useful to get a tilted view of the sample, and assess the results of underetching processes explained previously in Section 4.3.

A downside of this type of signal is given by the larger interaction region due to higher energies, leading to a lateral resolution loss. While this is not generally a significant issue, it became a problem for some of the antennas with smaller gaps, appearing ambiguous in InLens but clearly more visible with SE2 detection. Since SE2 electrons originate deeper and are collected by an angled Everhart–Thornley detector, they can provide stronger topographic contrast and higher lateral resolution. However, they also suffer from a shadowing effect, which can make them unsuitable for being used as the principal detection signal. The complementary characteristics of the two signals led to a combination of analyses, which proved to be useful for gap detection and measurement.

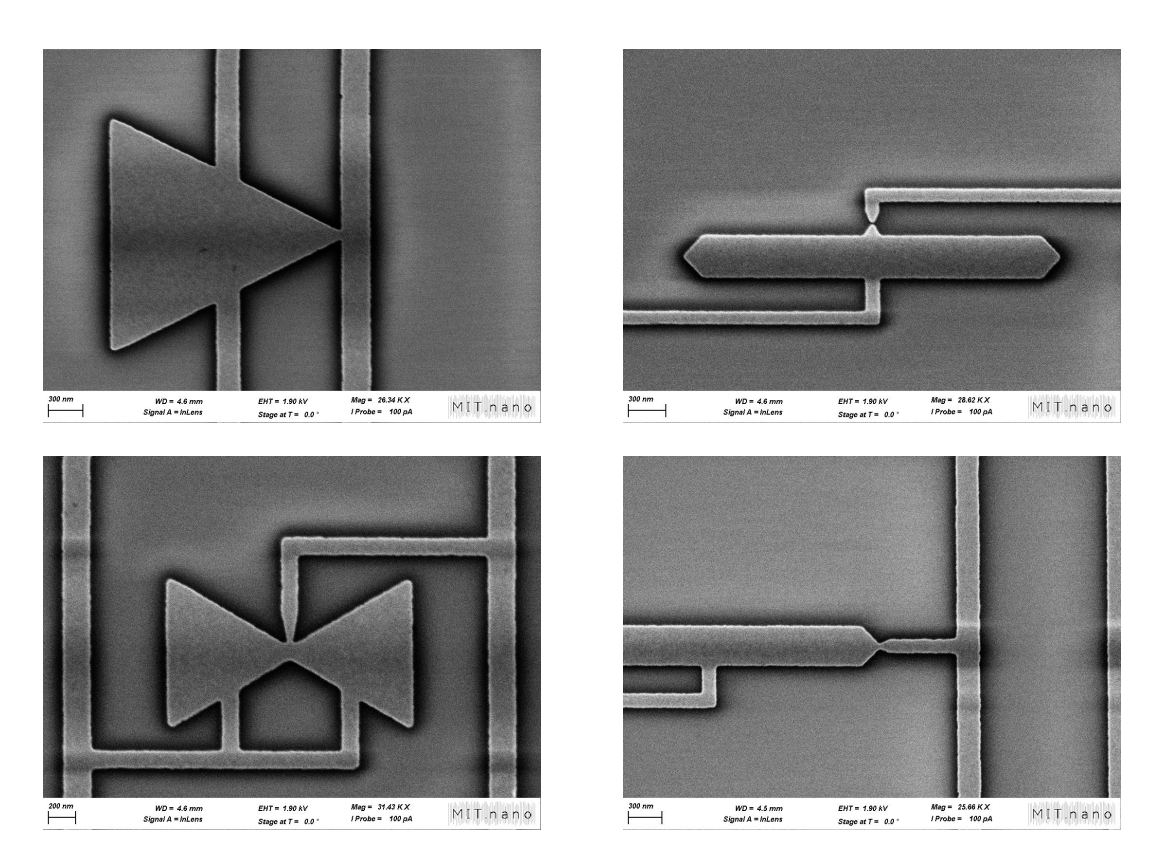


Figure 4.10: SEM images of fabricated nanoantenna geometries. (a) Triangular antennas, overdoses array does not present gap (b) Schottky nanorods, designed to present thermal hotspot across the gap region. (c) Bowtie arrays, overdoses array does not present gap (d) Field-enhancing nanorods, overdoses array does not present gap. All images were acquired with the InLens detector to emphasize surface morphology and definition of the gaps

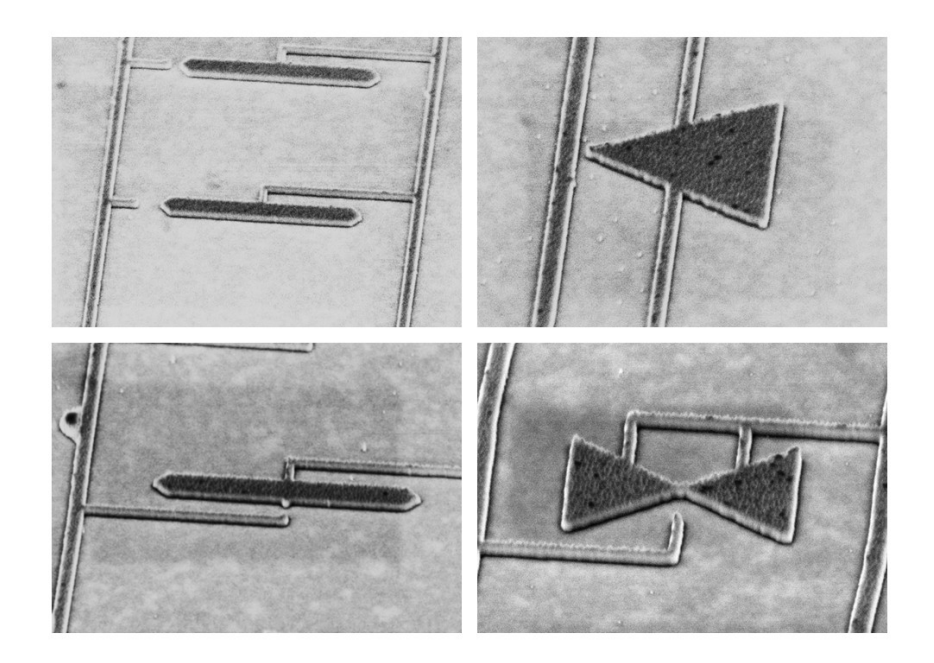


Figure 4.11: Tilted SEM images of the fabricated nanoantenna geometries. (a) Field-enhancing nanorods, (b) triangular antennas, (c) Schottky nanorods, and (d) bowtie antennas. All images were acquired with the InLens detector under tilt 55°, showing that the RIE process produced an anisotropic underetch, leaving the antennas standing on the silicon substrate.

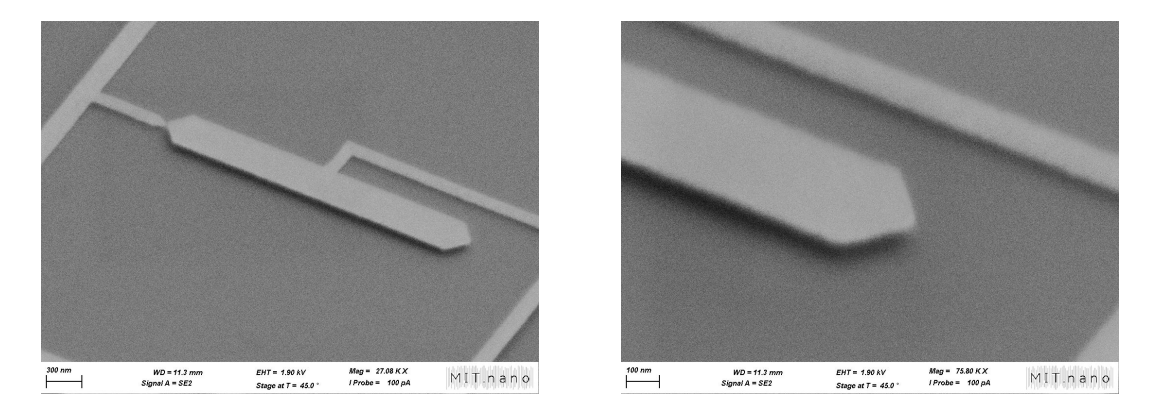


Figure 4.12: Tilted SEM image zoomed on a single nanorod. In this chip, the undercut was obtained by anisotropic wet etching, producing a cavity below the structure. As a result, the antenna appears suspended above the silicon substrate, giving the impression of a floating geometry.

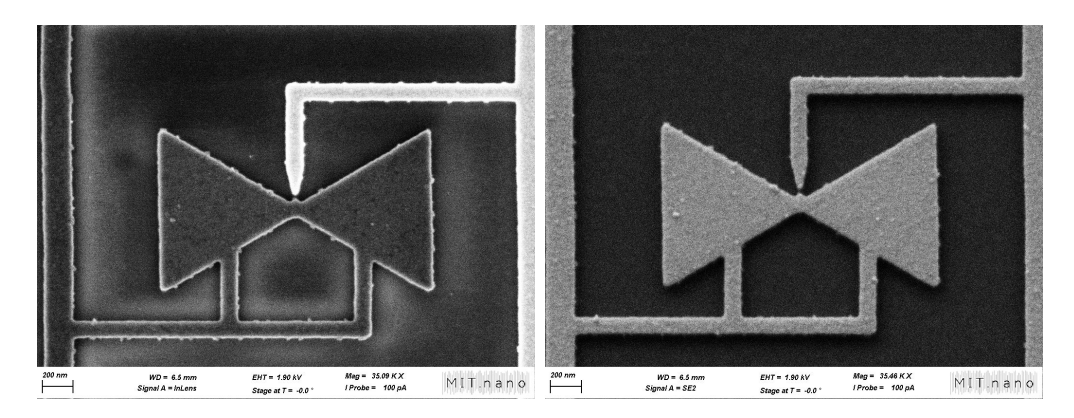
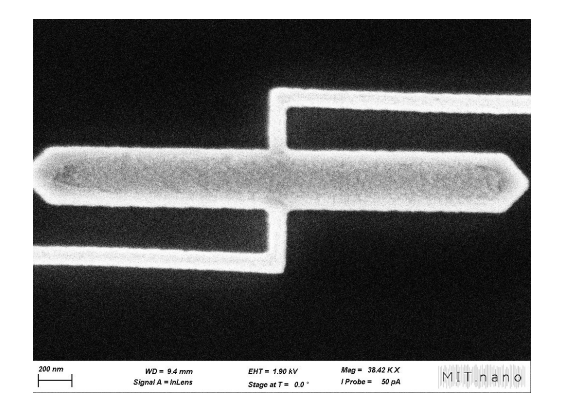


Figure 4.13: Comparison of InLens and SE2 imaging for a bowtie antenna. Sideby-side SEM images acquired with the InLens detector (left) and the SE2 detector (right). The InLens image emphasizes the surface morphology and especially clears the gap by the difference in color due to discharging effects, while the SE2 signal provides more superficial contrast, highlighting different aspects of the same structure.



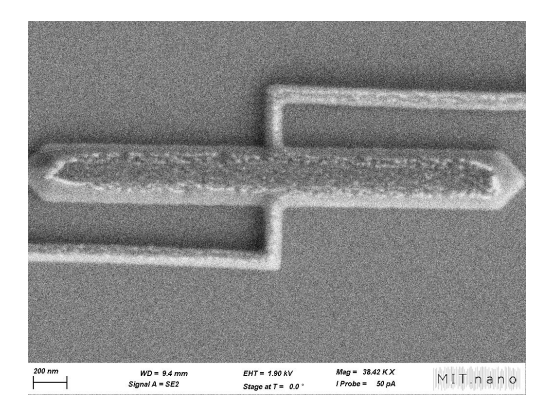


Figure 4.14: Schottky nanorod imaged with InLens and SE2 detectors. Some SEM views show that the gold nanorod was strongly damaged during the underetch process. The structure is barely visible in the InLens image but clearly resolved in SE2, underlining the complementary information provided by the two detectors.

The InLens and SE2 images were acquired with an accelerating voltage applied to the primary electron beam (EHT - Electron High Tension) of 1.90 kV, as suggested by literature for substrates with the same nature as ours, to reduce charging effects. The working distance was ~ 7 mm and the probe current was set ~ 100 pA, to have a stable beam with sufficient signal-to-noise ratio but without introducing visible charging [46, 47].

Variable pressure (VP) and nano-variable pressure (NanoVP) modes were also tested as alternative imaging conditions. In these configurations, a variable amount of gas (Ar) is introduced into the chamber to dissipate the charge accumulated on the insulating sample, as an alternative technique to imaging with conductive coatings, which are usually constructed in gold and are not usable in this case. The VP mode modifies the pressure in the whole chamber and allows a finer control on charging drift with respect to standard imaging mode, but, due to Argon scattering, introduces a loss in resolution. The NanoVP mode can mitigate this side effect by controlling the pressure only in a small region near the sample through the introduction of an additional funnel-shaped element around the column to confine the gas. However, since no substantial improvements were observed for the structures under study, these modes were not further exploited in the imaging process.

Given the difficulties encountered during the underetching processes, the need to perform compositional analysis emerged, solved using Energy-Dispersive Xray Spectroscopy (EDS), available in the SEM system. EDS detectors detect characteristic X-ray signals, generated by an inner rearrangement of electrons transitioning into an inner shell to electrically balance the vacancy created by a collision with a primary electron. The resulting signal is a result of these characteristic lines superimposed on a continuum background (Bremsstrahlung); this leads to indicative but not univocal chemical composition results, as the analysis can only give qualitative information. The EDS detector is placed in the vacuum chamber, and it exploits the interaction between X-ray photons and a cryogenic-cooled semiconductor bulk matrix (usually Li-doped Si). The incoming radiation generates an electron-hole pair in the photosensitive material and thanks to the accelerating bias applied, generated current impulses proportional to the incoming photon energy; this signal is then amplified and directed towards a counter system. Even if the chemical composition is not quantitatively accurate, it is useful to perform compositional mapping. To reach a sufficient signal on the EDS detector, higher energies were needed, and this led to a significant decrease in gold sensitivity due to its reduced thickness. However, this technique allowed a fast and precise assessment of the presence or absence of the SiO_2 layer residue after etching processes.

EDS measurements were acquired using different beam accelerating voltages (EHT), starting from 15 kV and then reducing to 10 kV and 6 kV, while increasing

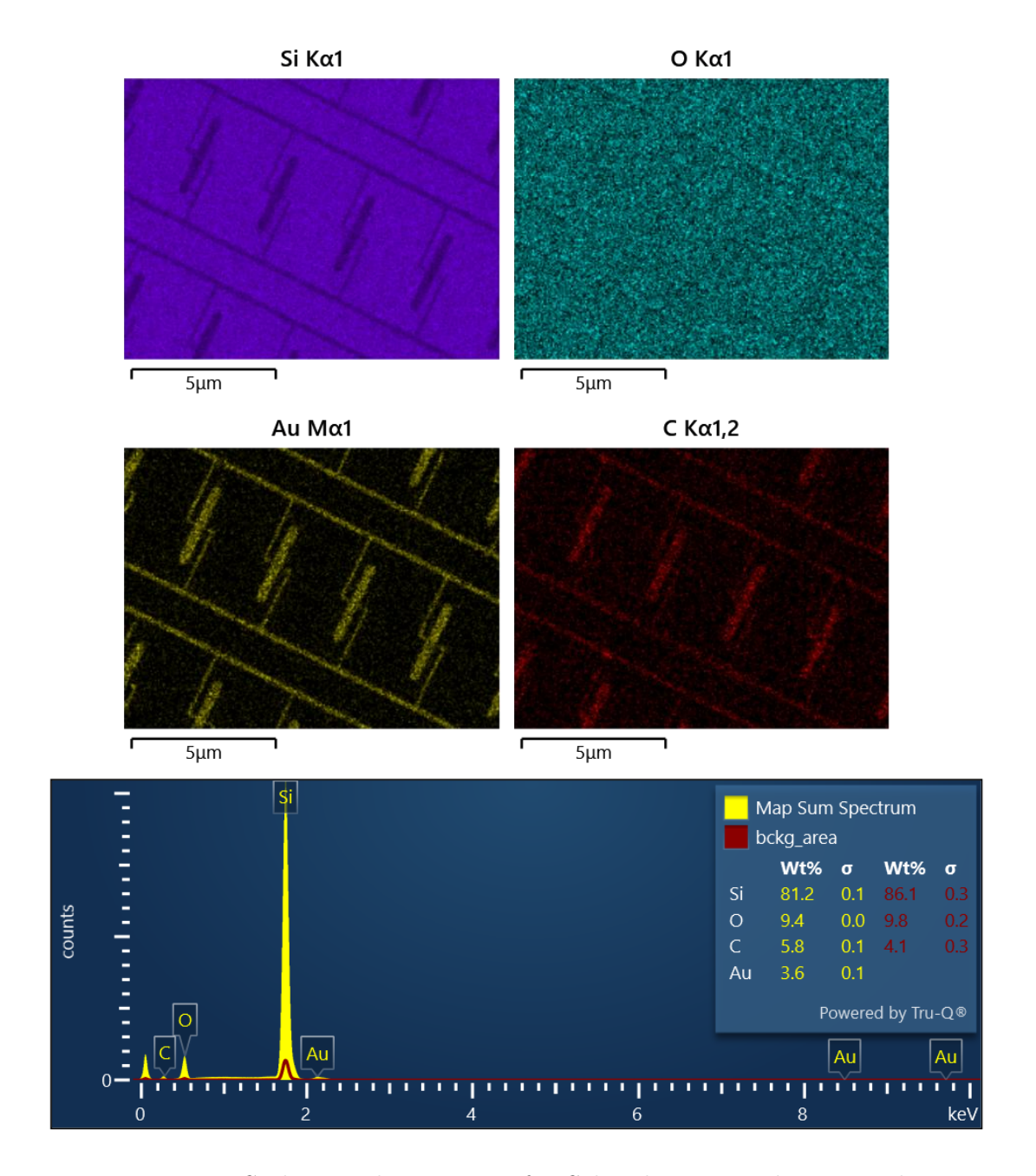


Figure 4.15: EDS elemental mapping of a Schottky nanorod array. The maps report the spatial distribution of Si, O, Au, and C. Gold is localized only on the nanorods, confirming the successful definition of the antenna geometry. Silicon and oxygen signals are distributed across the entire substrate, indicating that the underetch was not effective and the oxide layer was not selectively removed. A residual carbon background is also visible, likely from resist contamination. The superimposed spectrum extracted from the mapping region, compared with the background, highlights the clear Au peaks confined to the antennas, while Si and O dominate the substrate signal.

probe current up to 200 pA to compensate for the signal loss. The change in voltage was used to balance penetration depth and surface sensitivity, while the probe current ensured a sufficient X-ray yield on the detector. Integration times were also progressively adjusted in each case to obtain a stable spectrum with an adequate signal-to-noise ratio.

This analysis revealed some non-trivial issues connected to the fabrication processes, especially in chips subjected to RIE, where the majority of the devices did not survive. In some cases, faint antenna-like features could still be distinguished in InLens images, but no corresponding structure was detected with SE2, indicating that the original metallic antennas had been completely damaged by the plasma process. In other cases, antennas with a topological appearance were visible, but the severe surface damage raised doubts about their actual composition. EDS confirmed these suspicions, showing that the structures were not gold antennas but unetched SiO_2 . This feedback was fundamental, since it pointed to the need for adjusting the plasma power and chemistry in order to prevent gold degradation during underetching.

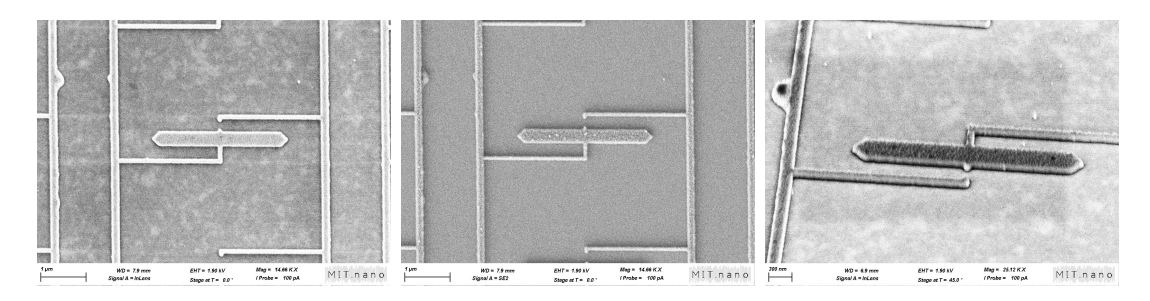


Figure 4.16: SEM images of a Schottky nanorod array after Au loss. InLens (left) shows weak surface contrast; SE2 (center) reveals missing nanorod tips from gold removal. The tilted view (right) confirms the absence of metal and shows residual underetched structures on the substrate.

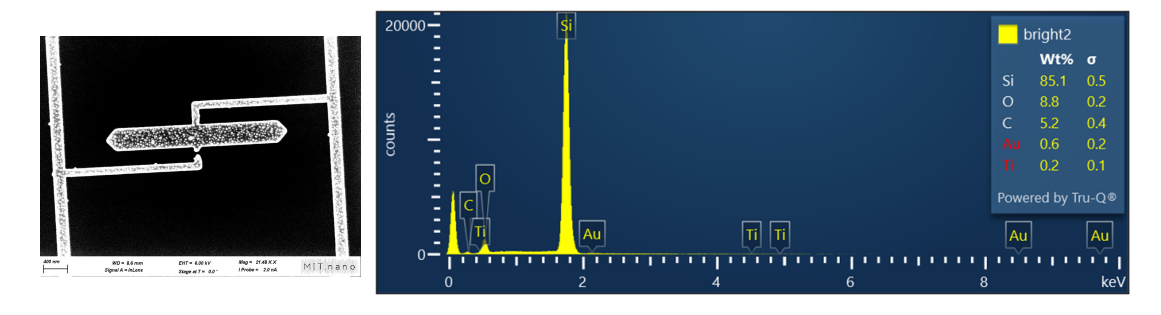


Figure 4.17: EDS of a Schottky nanorod array after Au loss. Elemental maps show only Si, O, and C across the substrate; Au is absent. The spectrum likewise lacks Au peaks, indicating complete removal of the nanorods—consistent with SEM evidence of metal loss after underetching.

5. Experimental setup for device characterization

Building upon prior work that distinguished Fowler–Nordheim and Schottky emission regimes in nanostructured systems [38], this thesis focuses on employing their combined behavior for infrared detection. To make progress in the project and eventually advance towards a deployable device, the optoelectronic detection capabilities, such as responsivity, temporal response speed, and signal-to-noise ratio (SNR), need to be characterized. Given the experimental nature of the device, no commercially available system met all the project requirements. The characterization system fundamentally demanded a set of specialized capabilities: broadband infrared optical excitation, in-vacuum operation capability, and an electronic readout system capable of biasing the nanoantennas. To meet all these requirements, we designed and implemented a fully customized setup, which is fully described later in this chapter, together with performance measurements and benchmarking.

Section 5.1 introduces the optical subsystem, emphasizing IR/visible alignment and the strategies implemented. Section 5.2 focuses on the electronic readout chain and signal processing hardware. Section 5.3 illustrates the overall setup strategy, discussing trade-offs, limitations of the current setup, and possible alternatives.

5.1 Optical Characterization and Alignment System

The setup has been designed to work using different illumination lines with variable wavelengths, ranging from visible to long-wave IR (LWIR). Commercially available systems used to characterize more standard devices, such as photodiode benches or Fourier-Transform Infrared Spectroscopy (FTIR) spectrometers, lack some key features needed for the benchmarking of this device. It is non-trivial to find a system that simultaneously supports both IR and visible spectral lines. Moreover, it was necessary to integrate a low-pressure environment, such as a vacuum chamber, to test the devices under variable pressure and address their pressure-dependent response. The need for a vacuum environment during testing also introduced additional complications for performing in-situ electrical measurements.

A custom platform was therefore implemented to meet these requirements. A key element of the setup is the FTIR unit, which was internally modified to act as an IR source in this optical setup. The setup included an IR source for optical excitation, a collinear visible branch to be able to navigate and locate arrays on the chip, a vacuum chamber for testing, and a power supply to bias the device and perform lock-in amplifier measurements. On the chip, as previously noted, the photoactive section represents only a small fraction of the total area due to the ratio between antenna arrays and contacts. Having multiple geometries on the same chip requires the possibility to electronically isolate them independently, but removes the need for uniform illumination on the entire sample, and allows higher optical power density on the arrays under analysis. On the electrical part, this has been addressed by implementing individual switches on an additional Printed Circuit Board (PCB), as will be explained in the next section. On the optical side, this configuration required an additional real-time imaging branch to locate the optical beam on the desired area with high precision during measurements. Aligning such a system required fine mechanical control over multiple degrees of freedom, such as mirror tilt, axial displacement, and beam overlap, which made optical alignment one of the most demanding aspects of the setup. Similar parabolic-mirror configurations are reported in literature for broadband IR imaging and are known for their sensitivity to angular misalignment [48, 49].

From these requirements, the setup architecture followed naturally. Given the presence of an FTIR instrument in the lab and the possibility of using it for future spectral characterization, the internal FTIR laser has been chosen to act as the main IR source, internally modified to project its beam outward. The main challenge was to shrink the IR beam, initially $\sim 2''$ wide, to a sufficiently small focal spot using a rapid, low-cost solution, avoiding the use of specialized IR lenses. While such lenses exist, they are fairly uncommon on the commercial market, especially for broadband coverage, ranging from mid to long-wave infrared. A different approach was adopted through the use of a pair of parabolic mirrors. Beam focusing was achieved with a two-parabolic mirror configuration, chosen for its broadband response [50]. A broad spectral range was required to cover both mid- and long-wave IR while still being compatible with visible light.

In this configuration, the IR beam is focused by a single parabolic mirror, while the visible beam is reflected by both elements. This configuration is intended to compensate residual aberrations introduced by the off-axis geometry and reproduces the image plane outside of the system. The image so created is then captured and processed by an optical microscope branch, whose camera acts as a navigation system for the chip. Accurate collinearity between the IR and visible lines was achieved by placing a commercially available element that reflected IR light onto one mirror while transmitting visible light. An IR-selective mirror was implemented using an indium—tin—oxide (ITO) coating on glass and subsequently characterized. Literature reports that ITO on glass exhibits high visible transmission and enhanced

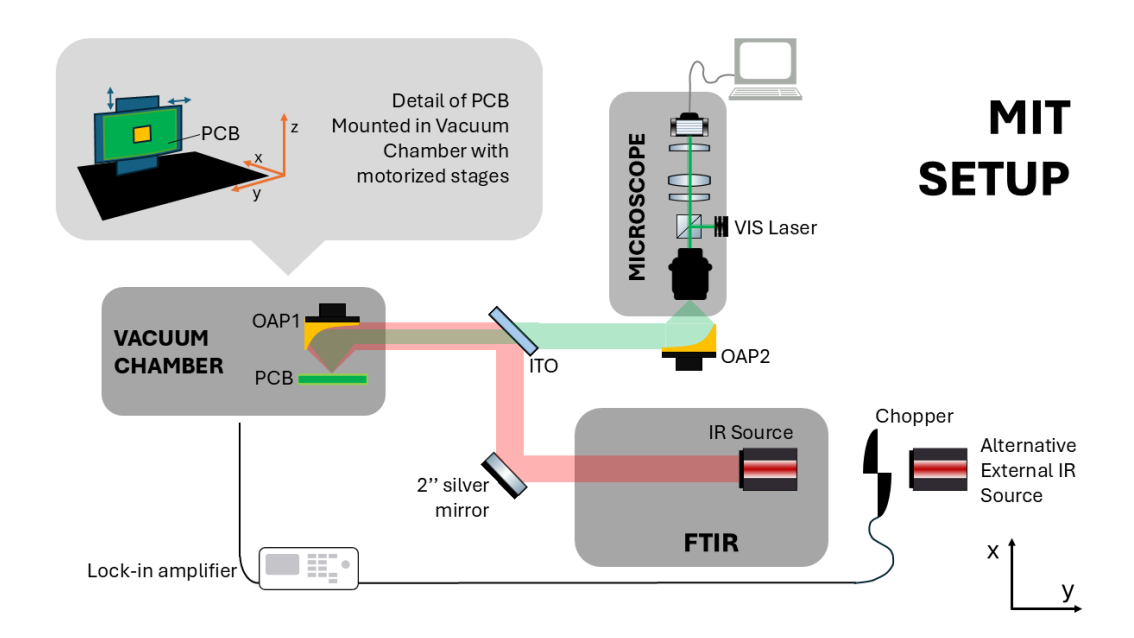


Figure 5.1: Preliminary sketch of the optical setup. Broadband or laser excitation is directed to the sample through free-space optics. A mechanical chopper modulates the beam to provide the reference for lock-in detection. The light beam is focused onto the chip inside the vacuum chamber, with windows and lenses arranged to preserve alignment and minimize aberrations. The scheme illustrates the optical path and components described in Section 5.1, serving as the basis for the subsequent implementation of FTIR and HeNe excitation sources.

infrared reflectance [51], making it suitable for use as a dichroic beam-splitter. Part of the system is then placed within a vacuum chamber, where the chip is mounted, to perform variable-pressure measurements. The following subsections provide the essential background for the main non-traditional elements in the schematic.

FTIR Source

The FTIR unit is a system able to provide spectral analysis exploiting the Fourier transform. It is a system based on a Michelson interferometer, composed of two branches, with one of them serving as a variable-length optical path. The source, typically in the IR range, is split by a beam-splitter, usually obtained by a germanium-based coating on a KBr element. The beam is partially directed towards the movable branch, where a moving motor controls and registers the mirror placement to measure the optical path difference δ . The detector records the resulting signal as a function of mirror displacement, producing an interferogram. In this setup, the FTIR optical path was internally modified to provide direct access to its broadband beam for external optical excitation, while preserving the instrument's capability for future spectral characterization of the device. It is possible to express the interferogram $I(\delta)$, given by the interference of the two

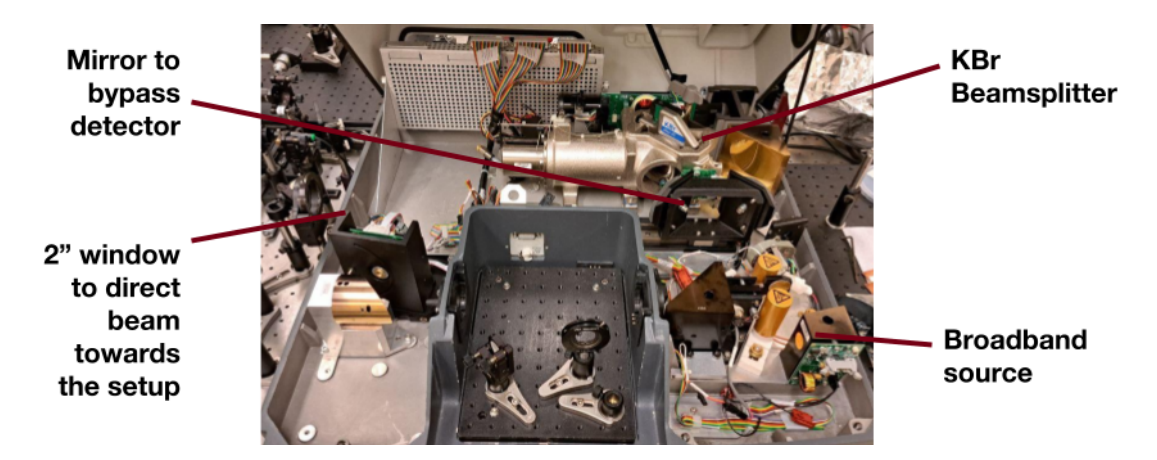


Figure 5.2: Internal view of the FTIR Nicolet 6700 spectrometer. Photograph showing the main optical components of the instrument: the broadband source, the Michelson interferometer with its moving mirror, and the detector stage. Mirrors, beam splitter, and optical paths are visible, providing a direct view of the layout that underlies the operation of the spectrometer.

branches, by its brightness using its Poynting vector and highlighting as δ the path difference, a cosine dependence can be found $[Wm^{-2}]$:

$$B_R(\sigma, \delta) = c\epsilon_0 |rt|^2 E_0^2(\sigma) [1 + \cos(2\pi\sigma\delta)]$$
(5.1)

where σ represents the wavenumber (λ^{-1}) . Taking into account a non-monochromatic point source and analyzing the total radiation power on the detector, carefully taking into consideration only the variable components, an interferogram can be mathematically defined as

$$F(\delta) = \frac{c\epsilon 0}{\bar{\sigma}} |rt|^2 \int_0^\infty E_0^2(\sigma) \cos(2\pi\sigma\delta) d\sigma \tag{5.2}$$

whose Inverse Fourier Transform corresponds to the spectrum previously defined:

$$B(\sigma) \propto \int_{-\infty}^{\infty} F(\delta) exp(-2\pi i \sigma \delta) d\delta = \mathcal{F}^{-1}[F(\delta)]$$
 (5.3)

Fourier Transform-based spectrometers have gained popularity with respect to dispersive monochromators because they present two main advantages. They represent a faster option since all the spectrum is collected simultaneously (Fellgett's advantage), at the same time, they are also able to maintain a higher signal-to-noise ratio since the signal intensity is given by the diameter size of the beam, not being confined by an entrance slit (Jacquinot's advantage).

In this work, the FTIR was used primarily as a broadband IR source. The detection path was bypassed to deliver a wide, collimated ($\sim 2''$) beam into the vacuum chamber for device excitation. It acted as a broadband IR source whose beam, by bypassing entirely the detection stage, was directed towards the detector

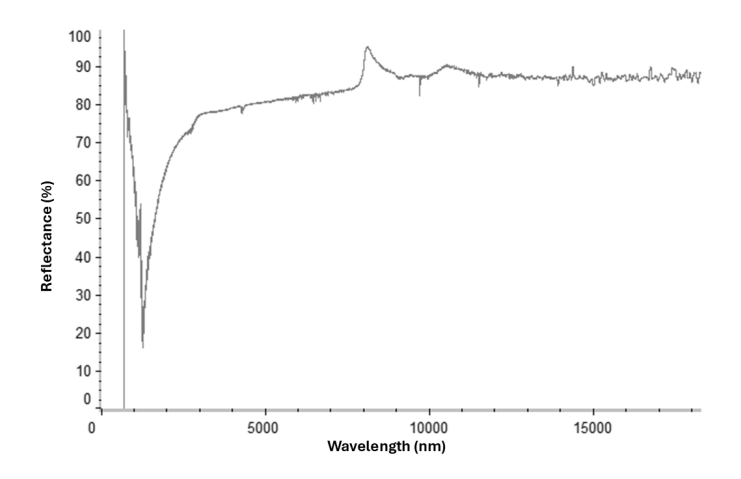


Figure 5.3: FTIR reflectance spectrum of the ITO dichroic beamsplitter. The curve reports the measured reflectance as a function of wavelength, showing low reflection in the visible and near-infrared regions and a strong increase beyond 2 μ m, where ITO behaves as a metallic reflector. The data confirm the expected dichroic behavior of the coating—transparent at short wavelengths and highly reflective in the mid- to long-wave infrared, consistent with the optical response of conductive oxides.

in the vacuum chamber to obtain IR excitation on the sample. The beam already had a wide, collimated ($\sim 2''$) nature, suited for the experiment requirements. The optical path modifications were completely reversible, and this allowed the instrument to be used for its intended spectral analysis purpose. This flexibility has been leveraged to spectrally characterize the ITO element and will be used for this analysis on the device in future implementations. The ITO dichroic beamsplitter exhibited behavior coherent with literature work, characterized by high reflectivity in the IR portion of the spectrum, combined with high transmission of visible wavelengths.

Parabolic Mirrors

To achieve both focusing and imaging, a pair of off-axis parabolic (OAP) mirrors was introduced in the setup. Refractive lenses were avoided due to their limited broadband availability and absorption in IR-compatible materials, leading to the adoption of reflective optics. In this context, OAP mirrors were chosen to provide achromatic focusing while preserving alignment flexibility. Their main advantages are broadband response and the absence of chromatic aberrations [48]. However, their alignment process remains challenging.

During alignment, at least six coupled parameters are involved, such as tilt, decentering, separation, and angular offset of each mirror. Each parameter can independently introduce coma or astigmatism if not properly compensated. This

Off-Axis Parabolic Metal Mirrors

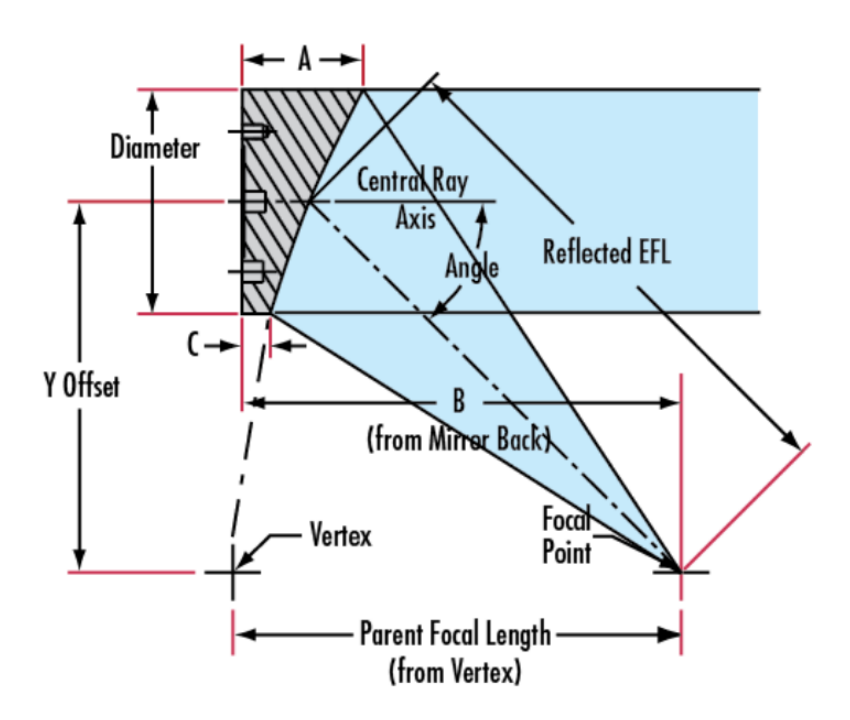


Figure 5.4: Figure adapted from [50]. Off-axis parabolic (OAP) mirror geometry. The diagram defines the parent focal length (from the vertex), off-axis angle, reflected effective focal length (EFL), focal point, and mechanical distances A (aperture setback), B (back working distance from mirror back), C (edge clearance), plus the mirror diameter and Y-offset of the off-axis section.

sensitivity represents the main limitation to reproducibility and requires iterative calibration. OAP mirrors can be viewed as sections cut from a parent parabolic mirror, which gives them their off-axis characteristics. When correctly positioned, they can focus a collimated beam onto a focal point, or conversely, collimate a point source placed at that point. The 90° off-axis geometry is obtained by cutting the parent parabola so that the focal point is laterally displaced from the central ray axis. This geometry gives the element a defined directionality, allowing precise collimation and focusing. A collimated beam centered on the parent axis is focused one effective focal length (EFL) away from the mirror surface, at a point offset laterally by an amount determined by the off-axis angle. Equivalently, the focus lies one parent focal length from the parabola's vertex, projected onto the off-axis section. When properly oriented, OAP mirrors can produce diffraction-limited images for collimated beams. However, for finite-conjugate imaging, aberrations such as coma and astigmatism appear, making alignment particularly challenging and time-consuming. To minimize these aberrations, the mirrors were arranged in a relay configuration, which enables image reproduction without magnification when correctly aligned. In this configuration, two identical OAP mirrors, characterized

by the same focal length, are positioned so that a collimated beam travels between them. This setup reproduces the focal plane without magnification and collects up to $30 \times$ more light compared to an equivalent lens-based system [48]. When well aligned, the image plane remains free from tilt and aberrations. However, even small misalignments can introduce significant distortions.

Mathematically, it is possible to characterize the alignment process with the use of Zernike polynomials, where astigmatism, coma, and trifoil distortions can be modelled as sinusoidal components [52]. Experimentally, this high sensitivity means that even minor mirror displacements manifest as deformations in the image plane. These can be detected and compensated for through specific calibration processes. To obtain a very high-quality image, surface quality has to be taken into account, since it can induce wavefront errors as aberration deformations. To account for these non-idealities, it is possible to use a Shack-Hartmann wave front sensor and compensate for any discrepancy with a flexible piezo-controllable bimorph mirror. In this project, the precision required does not justify such a procedure.

Alternative techniques have been proposed to improve calibration or to reduce sensitivity to misalignments, partially based on mathematical analysis of the resulting image. One of those is the technique proposed by Orlenko et al. [49]whose goal is the minimization of the M^2 factor, defined as the ratio between the beam's divergence and the Gaussian divergence. In practice, M^2 can be monitored via beam diameter/waist measurements; misalignment increases the effective diameter and thus M^2 [49]. Mathematically, in general terms we can define

$$M^2 = \frac{\pi w_0 \theta}{\lambda} \tag{5.4}$$

with w_0 the $1/e^2$ waist radius and θ the far-field half-angle divergence. Any distortion causes a higher beam spot diameter and consequently an increase in M^2 , to be tracked during the alignment process.

Another proven method aims at reducing the sensitivity to alignment by placing an objective after the mirror pair. By compensating small misalignments with an objective tuning, it is possible to desensitize the system to mirror displacement errors up to approximately $500\mu m$ [48]. This strategy has been applied to this setup, given its advantage and image magnification.

Finally, another alignment procedure has been developed based on a Shear Plate Interferometer [50, 53]. By placing this optical element between the pair of mirrors, it can give information on the collimation of the beam. This method uses the interference of the incident ray with its image reflected by the back face of a high-quality optical glass, placed at a 45° angle. Within the overlapping of the two beams, the coherent nature of the laser is able to create constructive and destructive interference, leading to a series of light and dark fringes on the observation screen.

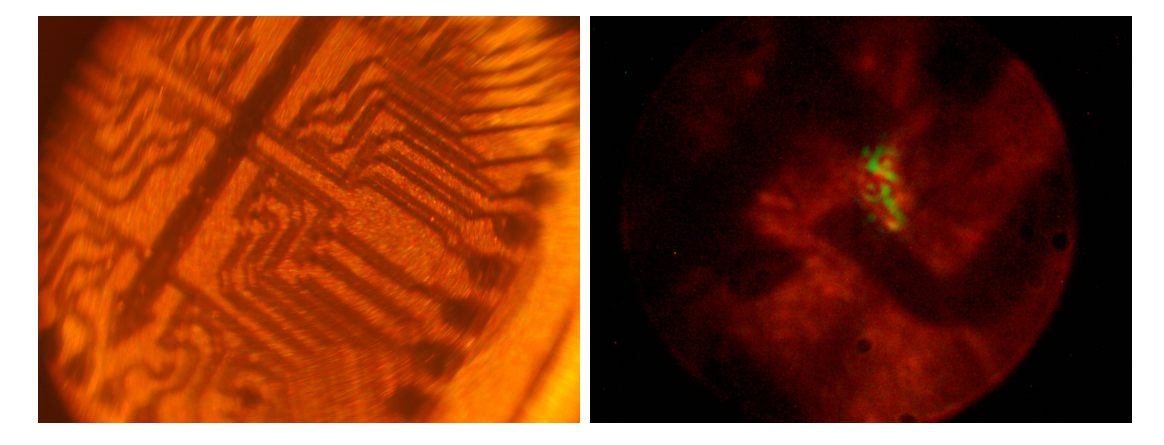


Figure 5.5: Images from the custom-built microscope given by a pair of OAP mirrors. Left: overview of the entire chip under illumination. Right: magnified view with the $20 \times$ objective, where the green tracer beam used for alignment and aiming is clearly visible on the sample surface.

The orientation of those with respect to some reference lines indicates the nature of the beam: counterclockwise-rotated fringes indicate a diverging beam, clockwise rotation points to a converging beam, and when the fringes appear parallel to the reference line, the beam is perfectly collimated. However, for the correct functioning of the system, some hypothesis are needed; the initial source needs a sufficiently high coherent length, exceeding the difference between the beam path and its reflection; the wavefront has to be approximately planar geometry when collimated or spherical when converging or diverging, without evident distortions that could influence and prevent the fringes from being created by interference phenomena. Furthermore, the combination of the wedge angle or the glass orientation needs to produce two beams with significant overlap, where the interference may take place; intensity and polarity have to be fairly constant for the interference to happen. Unfortunately, the laser used in this system presented an intrinsic Airy pattern, probably due to poor internal assembly of the laser element, which prevented stable fringes and made the method impractical in our setup.

Following these trials, a practical alignment procedure combining camera feedback and test-beam tracing was adopted, ensuring diffraction-limited focusing within the measurement range.

Final Experimental Setup and Schematic

The final experimental setup, shown in Figures 5.6 and 5.7, represents the complete and integrated implementation of the optical and electronic system described in the previous sections. It consolidates the preliminary optical design and alignment strategies into a single platform for device characterization.

Figure 5.6 illustrates the overall schematic of the system, where all main

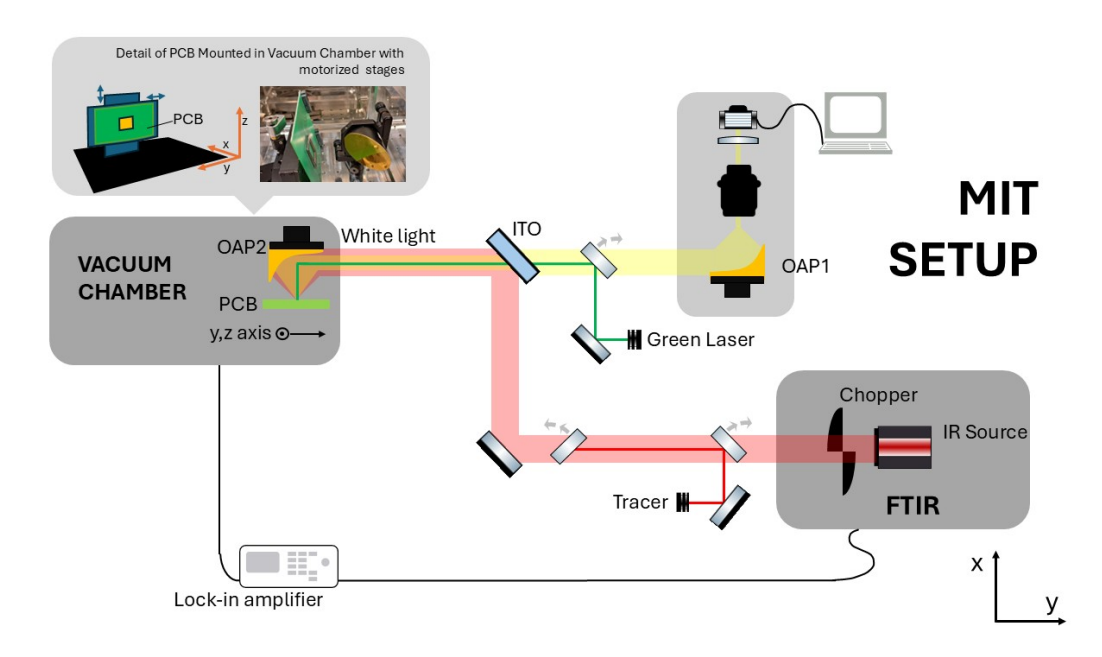


Figure 5.6: Schematic of the final experimental setup. The diagram summarizes the complete optical and electronic chain: broadband or laser source, beam conditioning and focusing optics, chopper for modulation, and the vacuum chamber containing the device. The photocurrent is converted to voltage by the transimpedance amplifier, referenced to the chopper, and read out by the lock-in amplifier. Additional elements such as shielding, FTIR coupling, and the VMA for noise analysis are included, providing a full overview of the setup as implemented in this work.

components are annotated for clarity: broadband or laser excitation sources, beam-conditioning optics, chopper for modulation, vacuum chamber housing the device, and the electronic readout chain composed of the transimpedance amplifier and lock-in amplifier. Additional subsystems such as shielding, FTIR coupling, and the vector signal analyzer (VSA) for noise analysis are also indicated.

Compared with the earlier preliminary configuration, this final setup integrates the external microscope and illumination subsystems more naturally into the optical path. The primary illumination source was provided by a green laser ($\lambda \approx 520$ nm), while a white light source was planned to be installed in a second phase. In this configuration, the external microscope positioning led the laser to pass through both OAP mirrors, projecting the focus point created by the lens objective onto the sample.

A more recent version of the setup was implemented by blending the external systems, such as the microscope, more naturally into the schematic. The current positioning of the visible source exploits its collimated nature by directing it in the intermediate space between the two mirrors and then focusing it onto the sample. An additional red laser ($\lambda \approx 650nm$) was also added to act as a tracer

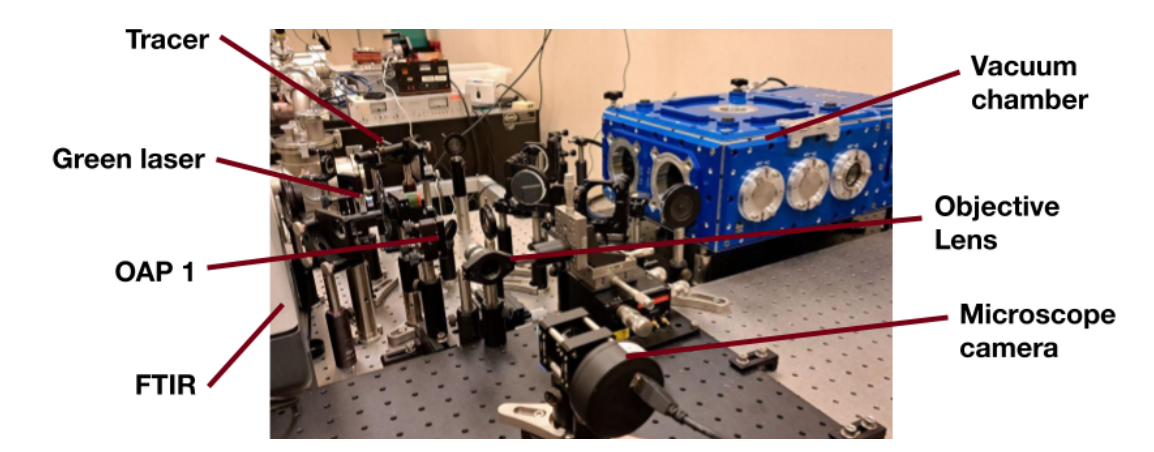


Figure 5.7: Photograph of the final experimental setup. The main optical path with mirrors, focusing optics, and the vacuum chamber is visible, together with the alignment tools and mechanical mounts. The picture provides an overview of the laboratory arrangement used for the measurements described in Chapter 5.

in the visible spectrum, facilitating IR alignment. This represents a common practice for non-visible wavelengths. A white light source was also added in the vacuum chamber to allow wide-field illumination and imaging. To navigate the chip inside the chamber without breaking the vacuum, two vacuum-compatible motors were installed on the PCB stages. Finally, two vacuum-compatible motors were mounted on the PCB stages to allow in-chamber chip navigation without breaking vacuum, completing the configuration of the final experimental setup.

Optical density estimate

Before testing, a preliminary estimation of the radiative power available from a blackbody source was conducted as a reference for expected illumination levels in simulations and later measurements. This was useful both for future experimentation where the optical excitation source is a black body, and for the complementary setup at LL facilities, where the source is indeed a Blackbody (BB) source. The calculation follows Planck's law for spectral radiance, restricting the emission to a defined solid angle and integrating over the relevant wavelength interval.

$$B_{\lambda}(T) = \frac{2hc^2}{\lambda^5} \frac{1}{\exp(hc/\lambda kT) - 1}$$
(5.5)

In practice, the emitted power can be expressed as the product of area, solid angle, and the integrated spectral radiance, while the received power at a distance can be approximated by an inverse-square scaling. The power received at a given distance r is given by:

$$P_{received} = a\Omega \int_{\lambda_{min}}^{\lambda_{max}} B_{\lambda}(T) d\lambda \times \frac{\Omega}{4\pi r^2}$$
 (5.6)

Using this approach, at 1000 K, for an emitting area of 1 cm² and a 10° half-angle cone and a distance of 0.3 m, the available power in the 2–5 μ m range is of the order of 8 mW, increasing to ~ 12 mW for the range 5 to 10 μ m. At 500 K, the power drops below the milliwatt level for both ranges.

5.2 Electronics and Signal Processing

The optical setup had to be completed with a dedicated electronic readout system to allow signal processing and characterization of the devices. An electronics chain was then designed and implemented to analyze the photosignal generated from the arrays. As discussed in Chapter 3 and Chapter 4, the antennas are expected to produce a photocurrent under illumination and external bias, supposedly in the picoampere to nanoampere range. Such weak current values represent a challenge for accurate measurements and require extremely specialized instrumentation, providing a low-noise and high-gain environment. The most straightforward solution is to convert the photocurrent signal into a measurable voltage by means of a transimpedance amplifier (TIA). The main constraints found in this stage were related to the high ambient noise level, introducing spurious signals at 60Hz frequencies and their harmonics; vacuum operation requirements and device-related problems. The approach used consisted of the use of a TIA-based setup to perform broad I-V characterization and photocurrent analysis via a synchronous detection system.

The first stage of the electronics setup consisted of the printed circuit boards (PCBs) and biasing network. The main PCB hosts a Leadless Chip Carrier (LCC) containing the device under test (DUT) and is placed inside the vacuum chamber. Given its placement in a pressure-controlled environment such as the vacuum chamber, some electrical feedthrough connectors have been implemented to link the board to the second PCB element, located outside the chamber.

The internal PCB first element has to operate in vacuum conditions due to the nanoantennas' extreme sensitivity to adsorbates. When operated in standard atmospheric conditions, the devices have been observed to adsorb contaminants, experiencing a significant drop in performance. This process has been reported to be suppressed when the devices are operated in vacuum conditions, and reverses the device degradation by desorbing surface impurities. The external PCB contained a matrix of switches, one per array, allowing each array to be connected or isolated from the electrical circuit independently. Some higher-level switches have also been implemented to control entire sections of arrays at once. This board also presents routing for external bias distribution to the antennas from a power supplier element. This element can differ, based on the type of analysis to be conducted, and usually consists of either a Source Measure Unit (SMU) for I–V sweeps or a transimpedance amplifier for synchronous detection. As the external board has

been observed to pick up non-negligible 60 Hz electromagnetic noise, it has been enclosed in a shielded metallic housing. Similarly, shielding techniques were also necessary for all elements of the signal, as the ambient environment proved to introduce significant noise coupling.

The signal chain proceeded with a transimpedance amplifier (TIA) to convert the photocurrent into a readable voltage. The TIA working principle consists of an adjustable gain between an input current and reading out the output voltage:

$$V_{\text{out}} = -I_{\text{in}} R_f \tag{5.7}$$

where V_{out} is the output voltage, I_{in} is the input photocurrent generated by the device, and R_f is the feedback resistance of the transimpedance amplifier. The amplifier introduces non-zero intrinsic noise, mainly due to Johnson noise related to the feedback resistor and input bias current noise. In addition, the feedback capacitance limits bandwidth operation, creating a trade-off between speed and gain. This relation represents a challenge in the project since the antenna's response is expected to be fast, as will be presented in Chapter 6, and thus a wide-band readout circuitry is required. Several amplifier configurations have been deployed during the measurement phase, covering gains between 10^7 to 10^9 V/A, and sufficient bandwidth.

The initial characterization relied on the previously described setup connected to a Keysight SMU for I-V curves acquisition. Preliminary measurements presented noise as current spikes, traceable to the charging effect in the partially etched oxide layer. They also showed a reduction in hysteresis with respect to non-underetched, confirming the benefit of oxide removal to obtain replicable, stable results. However, no quantitative analyses could be completed due to an instrument failure, resulting in the loss of data. After retrieving the information that Direct Current (DC) analyses are dominated by charging noise, the electronic measurements moved to a synchronous type of detection, specifically lock-in detection which is standard practice to improve the SNR of the device with respect to low-frequency noise.

To implement synchronous detection, some other elements were introduced, such as a reference modulation source and a lock-in amplifier for demodulation and amplification. By modulating the continuous optical signal at a known frequency f_0 using a chopper element, the photocurrent signal is then shifted away from low-f noise such as perturbative and 1/f noise, reducing the noise floor with respect to the signal. By mixing the signal with the reference frequency f_0 set by the chopper element, the system produces two replicas of the signal, one centered at $2f_0$ and a DC component, each with half the signal amplitude. A low-pass filter is then applied to isolate the DC component, recovering the initial signal while suppressing 1/f noise or perturbation, previously shifted at higher frequencies centered around f_0 and reduced by the low-pass filter.

For our measurements lock-in detection is very effective as the dominant noise source interfering with signal measurement is 1/f noise, also known as Flicker

noise when related to vacuum tubes and MOSFETs, or Excess noise in solid state detectors. It is mainly due to surface phenomena, where traps hold carriers for some time before releasing them. Its spectral density follows:

$$N_{1/f}^2(f) = CI^{\alpha} \frac{1}{f^{\beta}} \tag{5.8}$$

where C is a proportionality constant, I the current, and α, β are empirical exponents close to 1.

In addition to improving the SNR of our measurements, by varying the chopping frequency, it is possible to preliminarily estimate the device response time. When the modulation frequency approaches the response time, the detected signal is expected to decrease accordingly due to the inability of the nanoantennas to follow the modulation mechanism.

In summary, the electronic readout chain was designed to enable low-noise photocurrent measurements through transimpedance amplification and synchronous detection. The combined use of a TIA stage and lock-in amplifier provided the necessary gain and noise rejection to resolve signals in the picoampere range while maintaining compatibility with vacuum operation. This configuration established the baseline for all subsequent measurements, ensuring stable and reproducible operation during optical and electrical characterization.

5.3 Setup Design Strategy and Trade-offs

The overall measurement setup required several design choices and compromises due to the experimental characteristics of the device under test. Due to the nanoantennas' need for vacuum operation, under localized optical excitation and low noise readout circuitry, a series of multiple-domains constraints had to be satisfied across optical and electronic aspects. Main characteristic, also coincident with main challenge, was the broadband optical excitation in the infrared range to be coupled with a stable readout system in vacuum. While synchronous detection is a common approach in optical detector characterization, the combination of constraints made the use of commercially available systems impossible, requiring a custom design of the setup.

The first key design choice concerned the use of off-axis parabolic (OAP) mirrors instead of refractive lenses. The relay OAPs configuration presents several advantages, offering the image to be projected outside of the vacuum chamber, useful for tracer and microscope elements, without introducing aberrations if precisely aligned. It also enables tight focusing of the optical excitation onto a single array, increasing the optical power density on the active region. However, OAP mirrors implementation introduces several challenges, the main one represented by

the difficulty in alignment. Indeed, this system represents a non-common choice for optical setup application due to its non-trivial alignment process, involving many degrees of freedom relative to each element's positioning and orientation, as well as relative element-related placement. The configuration sensitivity to relative displacement has already been discussed in Section 5.1, where some strategies to ease the alignment. Nevertheless, the process remains extremely sensitive and its alignment is time-consuming, making it a non widely spread solution for common measurement systems. Alternative approaches based on IR or broadband refractive lenses could simplify alignment, offering a simpler and more compact solution, but that would require an iteration on the design step to preserve the external imaging capability.

A second major design trade-off has been represented by the use of the FTIR system as a broadband IR source. While it has been chosen due to its availability and wide spectral range, its spectral power distribution introduced some challenges in the measurement phase. While reaching the longwave IR range, corresponding to the nanoantennas' peak resonance, most of the emitted optical power appears to be peaked at a lower wavelength, around the near-IR range. This mismatch requires some filtering stages to isolate and individuate each component wavelength contribution to the device's signal. Future modifications may require different source choices, like a blackbody source or quantum cascade laser (QCL), to provide higher optical density and tunable excitation across IR radiation.

A further constraint was imposed by the vacuum environment. Maintaining a stable low-pressure ambient is essential to obtain repeatable measurements, due to the device's degrading behaviour in air. However, the vacuum chamber introduced additional challenges, regarding optical alignment, window optical losses, and electrical wiring because of the need for specialized feedthrough connectors. Future implementations may consider pressure control to be obtained in alternative configurations, such as a vacuum package into the detector housing, creating an antenna's environmental control closer to the final commercially intended form.

From the electronics perspective, the electronic readout circuitry presented design non-idealities influencing the measurement conditions. The use of benchtop instruments increased the noise floor of the system, compared to integrated solutions. A less noisy, more long-term alternative is represented by the integration on the device, or on the PCB, of an internal TIA stage with fixed gain. This solution is commonly implied in similar contexts and provides a pre-amplification stage enabling the signal to be read out as measurable voltage; it would reduce cable capacitance and external pickup, thus improving bandwidth and SNR. Implementing such an element would require careful noise and frequency response analysis to be conducted on the device, ensuring the additional stage does not introduce noise above the device's level intrinsic noise and limit the frequency signal.

In summary, the design choices and compromises made throughout the project were largely dictated by instrument availability and the specific constraints of the nanoantenna device. Despite their complexity, these decisions led to a functional first-generation measurement platform, able to deliver promising results, as presented in Chapter 6. Minor modifications, regarding source power, noise optimization, and vacuum integration, may be introduced in the next experimental phases to improve measurement accuracy and stability.

6. Optical Response and Device Performance

The purpose of this section is to present the preliminary experimental results obtained during the final stage of this thesis project. This phase was fundamental as it brought the project from proof of concept to measurable performance, demonstrating that the measurement setup was operational and able to deliver meaningful, repeatable measurements. Until now, no photocurrent had been reported in these devices at any spectral range. However, this work not only confirms the presence of a photocurrent but also reveals clear response trends under both visible and infrared excitation. The setup, therefore, enables the first quantitative assessment of device performance in these regimes. While initial data seemed to suggest an LWIR-driven photoresponse, follow-up spectral filtering showed the FTIR signal originated from the NIR tail of the source. In the Schottky-type geometries, analysis indicates Schottky emission, rather than Fowler–Nordheim, dominates.

This first assessment involved a limited number of arrays, restricting the set of geometries under test. The first device placed under test consisted of field-emission (FE) nanorods, but due to structural issues, a deep analysis was not possible. Most final measurements were performed on the Schottky-type bowtie nanoantennas, the array in question corresponding to 3J on Chip 12 and presenting a gap size of ~ 35 nm. The device under test (DUT) was mounted, as previously stated, on an LCC carrier integrated into the two-PCB system described in Section 5.2.

The nanorod array (Array 31) degraded during biasing because of electromigration, leaving only one conducting column, whereas the bowtie array (Array 9) remained stable and became the primary DUT for quantitative measurements.

In this preliminary test campaign, measurements were performed under different optical excitations. One of the sources, which produced interesting results still under analysis, was a visible range red laser ($\lambda \approx 650 nm$), delivering tens of milliwatts of optical power. Although this source was not broadband, it allowed an initial characterization of the device in the visible regime, far from resonance. At the same time, subsequent experiments targeted mid- and long-wave infrared (MWIR / LWIR) excitation closer to the antenna resonances. A first infrared (IR) investigation was conducted by introducing a secondary external helium-neon (HeNe) laser into the setup, characterized by a wavelength of $3.39 \mu m$. Lastly, a

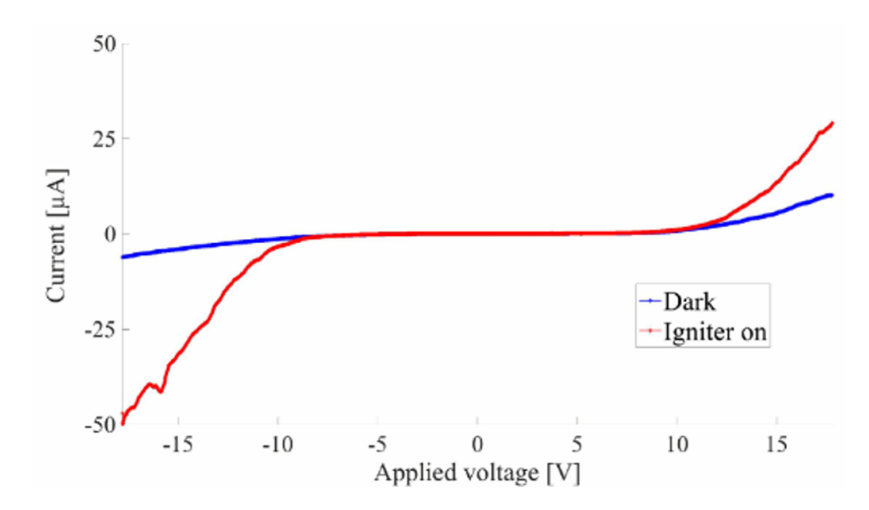


Figure 6.1: Figure adapted from [37]. Reference dark (blue) and illuminated (red) I–V characteristics for a metal–insulator–metal nanojunction under broadband excitation. Illumination lowers the effective barrier and enhances tunnelling/Schottky emission, giving a larger current magnitude and a small photo-offset near zero bias. This qualitative trend is what we expect and use as a guide in the first tests.

broadband FTIR source ($\lambda \sim 1-17\mu m$) provided excitation near the device's designed resonance, even though its available power was lower than ideal. The HeNe laser delivered about 2 mW over a 2.5 mm spot ($\sim 40~mWcm^{-2}$ intensity), and the FTIR Globar produced $\sim 0.1~mW$ of modulated power over a 1.5 mm spot ($\sim 5~mWcm^{-2}$).

As described in Section 5.2, the readout chain consisted of a transimpedance amplifier (TIA) followed by a lock-in amplifier for synchronous detection. Due to the gain–bandwidth trade-off, different TIAs were used, depending on the optical source involved. Depending on the photocurrent values under excitation, gains between 10^7 and 10^9 V/A were selected, and subsequently the modulation frequency was modified accordingly.

The main objectives of this initial testing round were to establish a baseline noise level and identify charging artefacts, verify the presence of photocurrent, and, if detected, evaluate its dependence on bias voltage and modulation frequency. A preliminary lower bound for detectivity (D^*) was also estimated to assess device sensitivity and bandwidth.

6.1 Static electrical characterization

First measurements focused on static electrical behaviour. This was performed by slightly modifying the electrical readout chain and replacing the lock-in amplifier with a Keysight Source-Measure Unit (SMU). This instrument enables direct current–voltage (I–V) sweeps from -10 V to +10 V, to assess the device's current

response in dark conditions. The goal was to establish baseline I-V characteristics and to identify a turn-on voltage (V_{TH}) , corresponding to the onset of electron emission. Above this threshold, electron emission becomes more favorable, enhancing device sensitivity to optical excitation. This bias defines the optimal operating region, where the signal-to-noise ratio (SNR) is expected to be maximized. From the first analysis, the I-V curves appeared noisy and unstable, mostly due to charging and discharging of traps in the oxide layer. These trap-level capture and release charges cause current spikes, particularly evident at higher bias when tunneling effects are significantly more present. Another feature, still under investigation, was a slow current decay after each voltage step, forming long transient tails. This raised a challenge as the base current was investigated to provide a theoretical shot-noise-limited regime, corresponding to the upper detectivity bound for the device. The presence of these behaviours suggests an interpretation of results consistent with charge relaxation in a dielectric layer, which can be modeled as an RC-type transient. The oxide layer remaining between emitter and collector thus appears to act as a capacitive coupling, altering the local electric field during charge accumulation and release.

Although preliminary, this interpretation provides a coherent explanation for the hysteresis and low-frequency noise later observed in synchronous measurements. charge relaxation in the dielectric layer, as o model this effect, the photosensitive antenna region can be represented as a source in series with an oxide capacitance C_{ox} and a leakage resistance R_l , giving a time constant:

$$\tau = R_l C_{ox} \tag{6.1}$$

defining the characteristic frequency of the charging noise. Section 6.3 further quantifies this high-pass charging behavior via frequency sweeps and outlines how to extract a corner frequency and time constant. The measured I-V characteristic showed a non-ohmic trend, consistent with field-assisted electron emission, attributable to a FN or Schottky mechanism. A gradual transition and subsequent increase in the current were observed for biases between 5 V and 10 V, marking the transition to emission-dominated behavior. Further quantitative analysis could have brought more insights into the turn-on threshold and static electrical characteristics. However, that was not possible due to a failure in the instrumentation, causing major data loss.

Additional tests were performed on array 1A, consisting of field-emission nanorods, which yielded currents in the picoampere range following a similar non-ohmic behavior. Subsequent SEM investigation of the array showed that most of the columns had failed during DC characterization, not able to withstand bias application. Only one column remained electrically connected, causing the signal previously captured by the SMU. The wires routing emitters and collectors showed local breakdowns due to electromigration, especially in areas where the

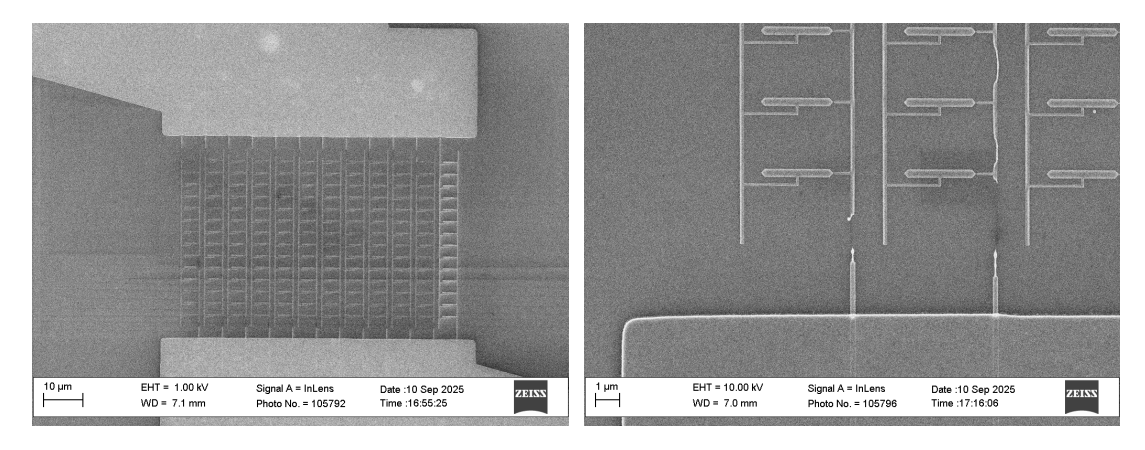


Figure 6.2: SEM illustrating device failure: only one column is still electrically connected out of the whole array (left) and broken wires (right). The failure is due to electromigration of columns presenting one or multiple shorted antenna devices.

current density is expected to be higher, i.e., in those portions where the wiring elements have to withstand current related to all the elements of the column. Further analysis showed how all of these columns presented one or more shorted devices, were no gap opened between emitter and collector. Given that this array intentionally pushed gap sizes below 20 nm, such shorts were expected. However, these local breakdowns electrically disconnected entire columns, making it impossible to recover shorted devices via electromigration of the gaps. This process was considered a viable option to open a gap in shorted devices, as it is supposed to represent the narrowest portion in the gold geometries and thus subject to electromigration under high biases applied. This technique has been known and used in similar arrays to be able to eliminate shorted antenna columns [54].

Overall, this analysis showed the desired non-ohmic response, alongside charging-related noise and structural non-idealities. Given the instrumentation failure and motivated by these results, the next analysis focused on synchronous detection to quantify optical photoresponse.

6.2 Synchronous detection and optical response

Later measurements used the standard configuration, employing a lock-in amplifier to enable synchronous detection. The first test involved the exposure to a visible photoexcitation from a red laser. This first response was prompted by a weak photoresponse previously noticed when the device was exposed to a broad white light source given by a halogen lamp. The laser used was able to deliver $\sim 2mW$ optical power, later reduced by a series of neutral-density (ND) absorptive filters, across a $\sim 3mm$ diameter spot. The antennas were biased at 2 V, and the transimpedance amplifier was set to a $10^7 V/A$ gain. The measurements showed a

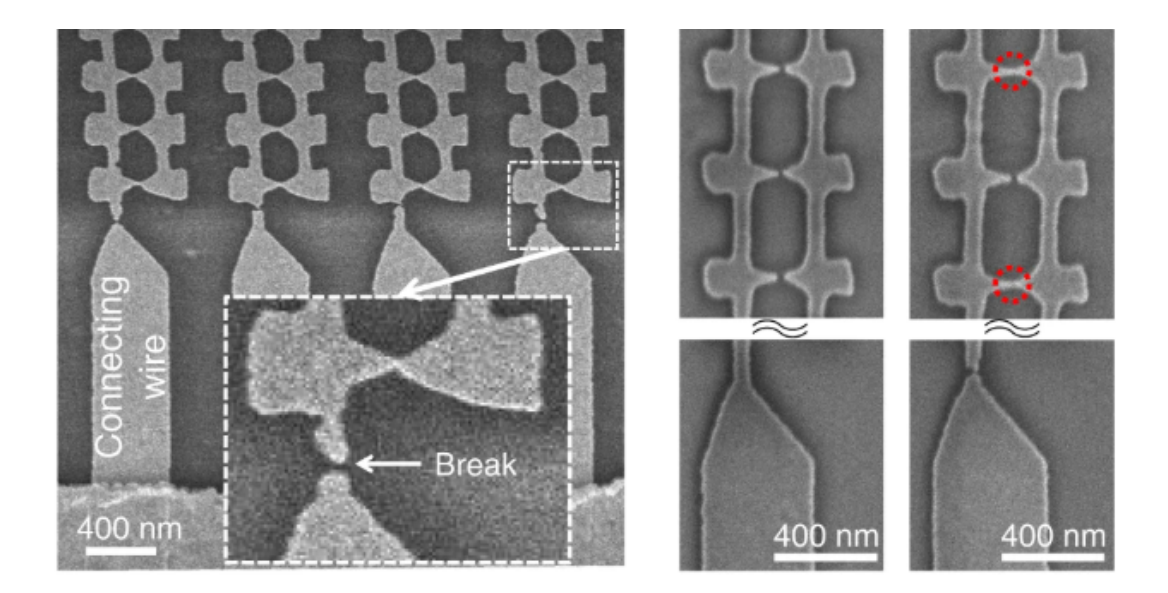


Figure 6.3: SEM image showing the intentional thinning of the connecting wire (adapted from [54]). This structural modification was introduced to enable the selective disconnection of shorted antenna columns: when a column exhibited an electrical short, localized electromigration at the thinned region effectively isolated it from the circuit.

photoresponse of $\sim 17mV$ at a chopping frequency of 500 Hz. This corresponds to a 1.7 nA photocurrent, giving R $\sim 8.510^{-7}$ A/W. When a 1.0 Optical Density (OD) Neutral Density (ND) absorptive filter was introduced, the current reported a drop to 0.6 nA.

An increase in the chopping frequency is supposed to cause a stabilization of the signal, followed by a decrease when overcoming the device response time. Instead, a strong signal increase was observed at higher frequencies, with an output of $\sim 30mV$ at 3.8 kHz, the maximum chopping frequency allowed by this setup. The signal increasing trend was present throughout the whole frequency range, suggesting that the stable regime or cutoff is present at higher frequencies, and the device response time had not yet been reached at these time scales. The measured noise level, around 1.3 μ V, was identified as electronics-limited rather than intrinsic to the device, since the system remained readout-noise-dominated. A more accurate noise floor is expected to be reached by fabricating larger devices, whose noise should not be drowned out by the electronic instruments' noise, or by implementing the Vector Measurement Analyzer (VMA). Under these conditions, the visible-range detectivity, computed using the measured noise, is an approximate value of $D^* \sim 10^8$ Jones.

Similar measurements were conducted using a mid-infrared HeNe laser ($\lambda = 3.39$ μm). Photocurrent levels of approximately 10 fA for the nanorod array and 100 fA for the bowtie array were recorded at 5 V bias and 150 Hz modulation,

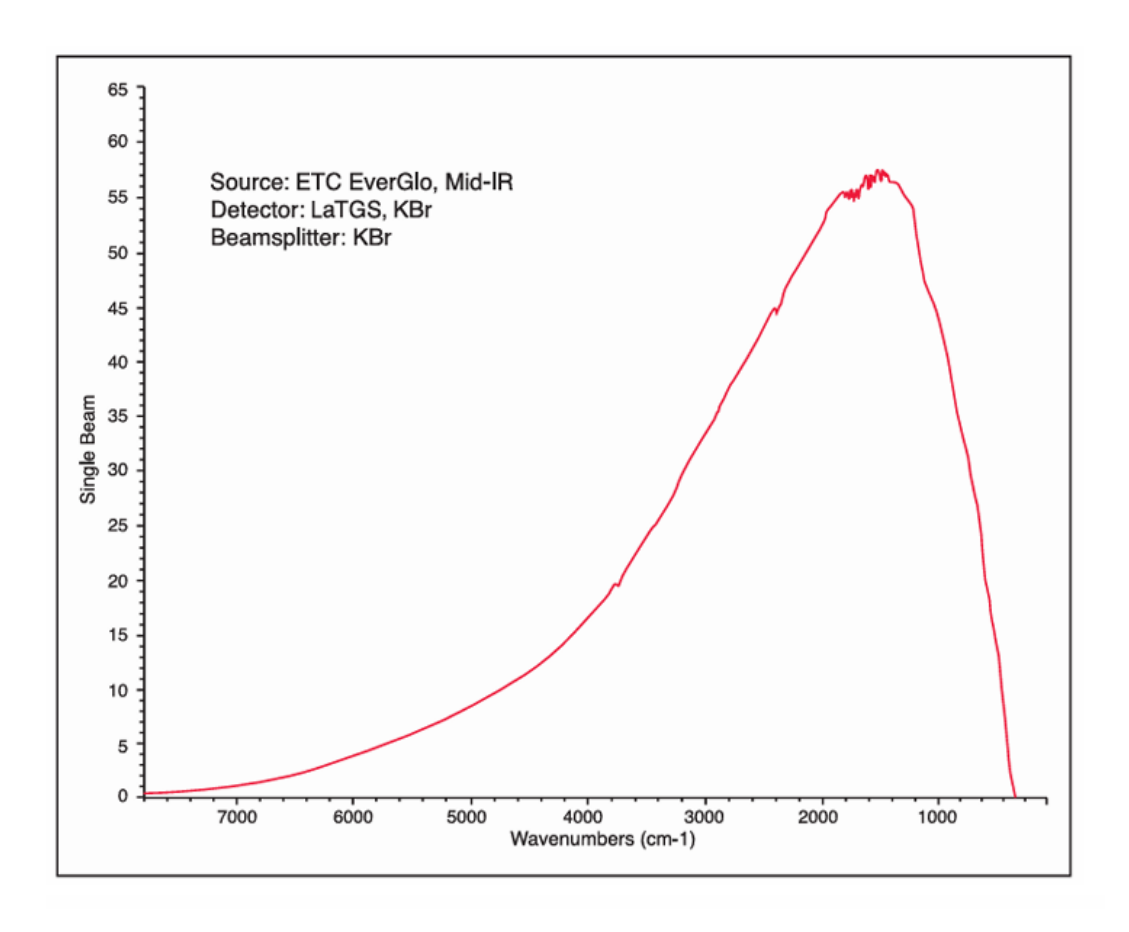


Figure 6.4: Mid-IR portion of Globar spectrum, providing a broadband infrared illumination peaking in the mid-IR region. It spans wavelengths ~ 1 - $17\mu m$, corresponding to wavenumbers ~ 600 - $10000cm^{-1}$.

corresponding to responsivities of roughly 5 x 10^{-11} A/W. Because no independent noise measurement was performed in this configuration, detectivity can only be roughly estimated in the 10^3 Jones range. Later filter tests show no 3–5 μm band response in our FTIR runs, consistent with the small HeNe response.

With the intention of testing wavelengths closer to resonance, the measurements were repeated under illumination by an FTIR broadband source. The optical setup redirected the IR beam, focusing it onto a 3 mm spot, delivering ~ 0.1 mW of modulated mid-/long-IR power. As the initial FTIR beam was large, the chopper frequencies were limited by the need to use larger chopper wheel apertures, as the assumption of a beam size significantly smaller than the slit aperture had to hold to avoid waveform distortion. At a 5 V bias and a gain set to 10^9 , the measured signal was $\sim 0.4 mV$, follow-up spectral checks indicate the residual signal is dominated by the source's NIR tail.

In air, the bowtie array produced a photocurrent of about 90 fA ($\approx 1 \,\mu A/W$ responsivity), while in rough vacuum (~ 100 mTorr) the responsivity increased to $\approx 45 \,\mu A/W$. Follow-on measurements with an 8 μm long-pass and a 3–5 μm band-

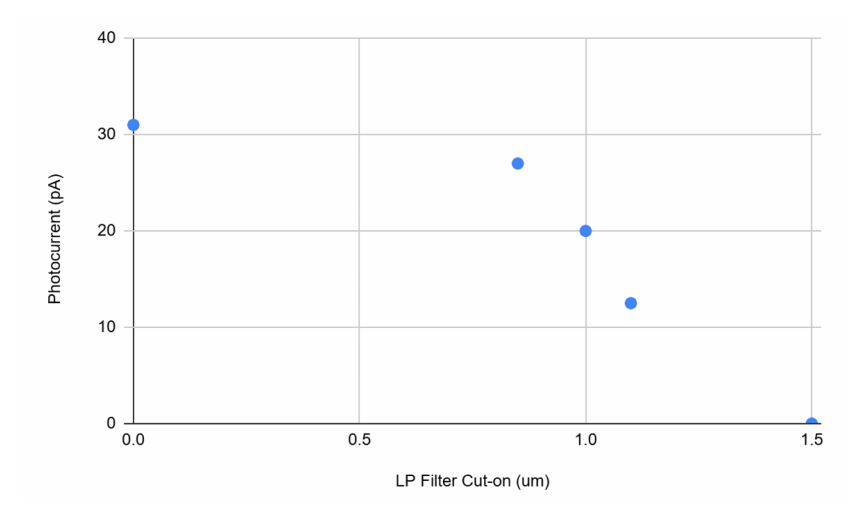


Figure 6.5: Lock-in photocurrent versus long-pass (LP) filter cut-on wavelength at fixed bias and identical optical alignment. The signal decreases monotonically and vanishes with a 1.5 μm LP, indicating that the detected response is dominated by sub-1.5 μm (NIR) content rather than mid/LWIR band radiation.

pass showed no photocurrent, whereas filters that admitted shorter wavelengths did yield a measurable signal. This indicates the FTIR response was dominated by the NIR tail of the source, not LWIR resonance. A refined spot-size estimate and spectral slicing further show that the available in-band LWIR power at the device was very low, explaining why LWIR did not rise above the noise floor. If one (incorrectly) attributes the observed signal only to 8.5–9.5 μm power, the apparent D^* would exceed $\sim 10^7$ Jones, highlighting why spectral filtering is essential.

6.3 Device speed and charging

A second finding is a high-pass behavior: the 1f photocurrent increases with chopping frequency. We model the oxide-charging transients as a first-order high-pass; fitting the 1f amplitude $A_{1f}(f)$ versus f yields a corner frequency $f_c = 1/(2\pi\tau)$, with $\tau = R_l C_{ox}$. Conceptually, the lock-in integrates a spike-and-decay waveform over each half-cycle, so A_{1f} grows as f approaches and exceeds f_c . With more datapoints, a fit should recover f_c and τ . This behavior is consistent with charging previously observed under DC bias. The undercut process is intended to mitigate charging; the chip here was not fully etched down into Si. We could not chop fast enough in the initial run to see a plateau, but the adjusted setup now reaches ~ 3.5 kHz. The devices still respond (to NIR) at this speed without an obvious roll-off, though a detailed speed study remains future work while emission mechanisms are prioritized.

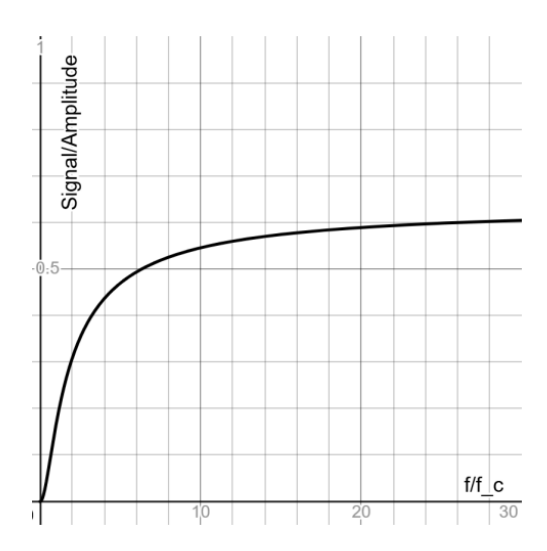


Figure 6.6: Normalized lock-in amplitude versus normalized chopping frequency f/f_c for a first-order RC-coupled (high-pass) model of the device. The response is suppressed at very low f, rises monotonically through the cutoff, and approaches a constant for $f \gg f_c$, consistent with charging-dominated behavior, where $f_c = 1/(2\pi RC)$.

6.4 Spectral trends and mechanism interpretation

Across visible, mid-IR, and long-IR ranges, a clear difference in photoresponse is reported: much higher response can be observed under visible optical excitation, a strong suppression appears in the mid-IR, and an apparent recovery is seen under FTIR illumination. Follow-up spectral checks indicate this recovery comes from the short-wavelength (NIR) tail of the source rather than true LWIR. The physical interpretation of behaviour points towards a double phenomenon-based model. Analyzing the work proposed by Turchetti et al. [55], an alternative mechanism may be involved when analyzing the visible spectral range. While the red laserassociated photon energy is not sufficiently strong to lower the Au work function, creating a photoelectric effect, a multi-photon-driven absorption would explain the strong signal response. These explanations also seem to be consistent with the confinement of a strong signal related to red-associated wavelength and not present in different visible wavelengths. This effect becomes negligible at longer wavelengths, such as in the infrared range, where the signal is expected to be related mainly to field-assisted emission. At the HeNe wavelength, the available in-band power is insufficient, and although plasmonic enhancement near the designed resonance can boost local fields, the measured FTIR response here was dominated by NIR leakage, not true LWIR. The emerging interpretation is hybrid: multiphoton absorption drives the red-laser signal; field-assisted emission is weak in the mid-IR; and the FTIR response observed here was off-band (NIR tail) rather than LWIR. Demonstrating true LWIR response will require higher in-band power

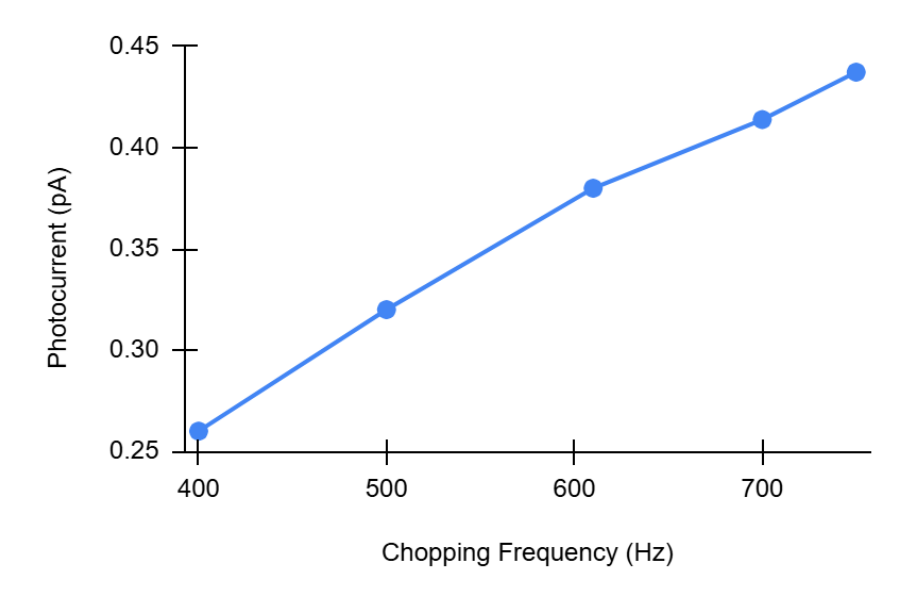


Figure 6.7: Photocurrent as a function of modulation frequency, measured under FTIR illumination at a constant 5 V bias. The increase in signal is consistent with the suppression of oxide-related capacitive effects at higher frequencies.

and/or lower device noise.

6.5 Frequency sweeps and bias dependence

To obtain more stable quantitative results, frequency-dependent sweeps were performed under FTIR illumination at a constant 5 V bias. The photocurrent increased sharply from 100 Hz to about 500 Hz, after which the response began to flatten and gradually decrease, a behaviour marking a roll-off around 500 Hz. This trend indicates suppression of oxide-related charging at low frequencies and the onset of the combined device-and-readout bandwidth limit beyond 500 Hz.

The charge and discharge dynamics related to the oxide are to be considered negligible beyond the trap intrinsic noise frequency, resulting in a stronger, stable signal. It would have been extremely useful to verify this trend at frequencies beyond the kHz regime to determine whether a stability of the signal is reached and subsequently lost, signalling that the device's intrinsic time response has been matched. This analysis was not possible in the current configuration due to chopper limitations; future implementations are planned to enable high harmonic chopping (5f) by reducing the FTIR beam size.

A complementary analysis involved bias-dependent sweeps under FTIR illumination. Measurement conditions correspond to chopping frequency f=500 Hz and a swept-in bias applied from -2 V to 10 V. At low biases (< 3 V), the response remained below the noise floor, as verified by no stable lock-in phase

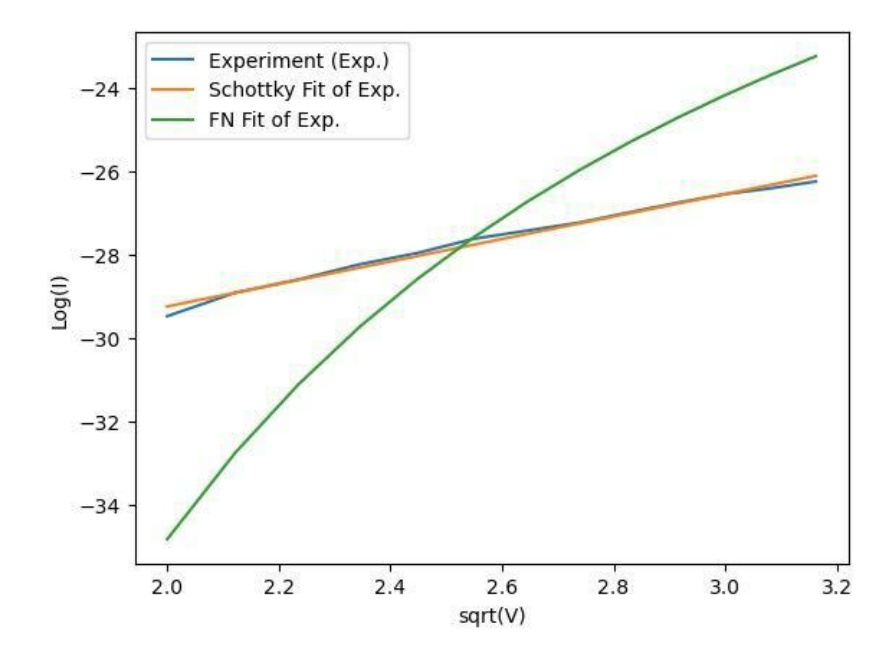


Figure 6.8: Discrimination between emission mechanisms: experimental data plotted as $\log(I)$ vs $V^{1/2}$ (blue) compared with a Schottky fit and a Fowler–Nordheim (FN) fit. In this Schottky-linearization, the data follow a near-linear trend reproduced by the Schottky model (orange), while the FN model (green) shows strong curvature and mismatch. This indicates Schottky-dominated transport over the measured bias range at room temperature.

registered. Around 5 V, a weak but stable photoresponse appears to compete with readout circuitry, as verified by the constant lock-in phase detected, confirming the weak signal does not correspond to a noise artifact. For higher biases, the photocurrent appears to follow a quasi-exponential behaviour, peaking at ~ 4 pA at 10 V. Analyzing the resulting trend in a Schottky plot, representing log(I) vs $V^{1/2}$, confirmed Schottky-type field-assisted emission as the dominant transport mechanism. In this representation, a Schottky analysis provided a substantially better linear fit than Fowler–Nordheim (under plausible enhancement factors), indicating a Schottky emission in this regime. This result indicates a transition happening from a non-assisted regime, where no electron emission effect creates dominant charges flowing, to a field-assisted emission mechanism for biases higher than a turn-on voltage. The constant phase across this range further supports the stability of the detected signal.

6.6 Interpretation and outlook

Different trends have been observed across measurements, pointing to different explanations, still under investigation. The first interpretation of the previously shown results is given by a hybrid dual-mechanism emission, where a multiphoton

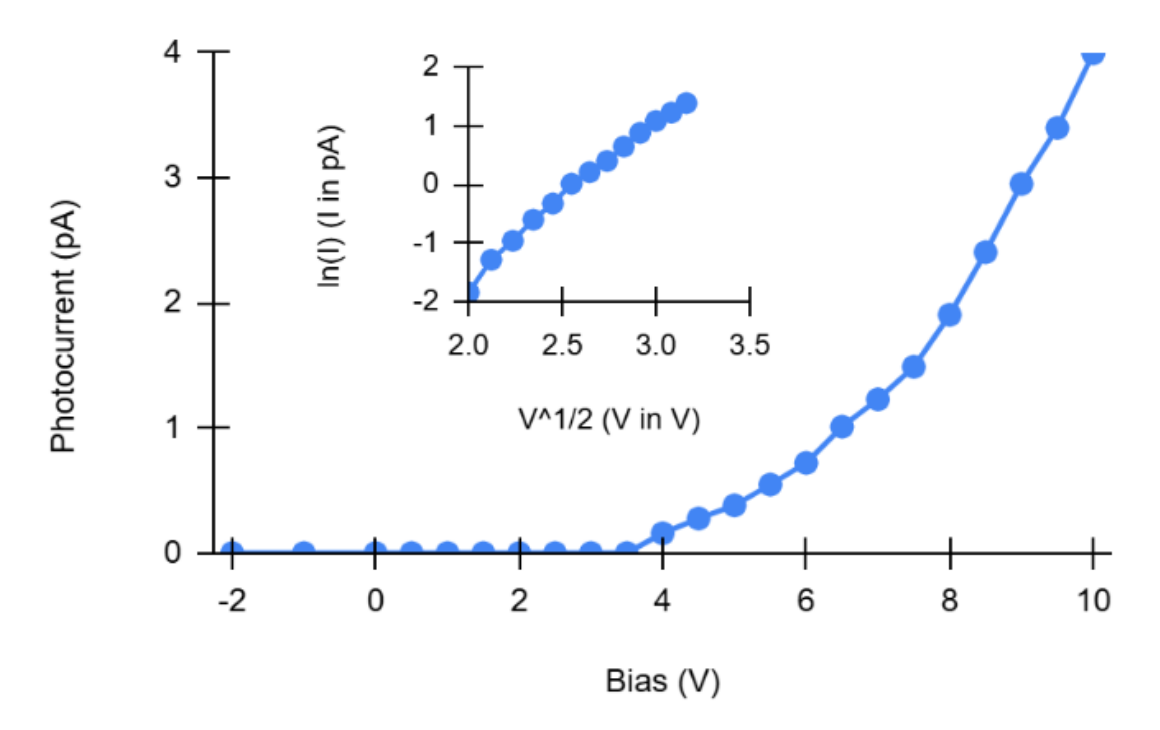


Figure 6.9: Photocurrent as a function of applied bias under FTIR illumination at a chopping frequency of 500 Hz. At low biases (< 3 V), the signal remains below the detection threshold, while around 5 V, a stable photoresponse emerges, indicating the onset of field-assisted emission. For higher biases, the photocurrent follows a quasi-exponential trend, reaching ~ 4 pA at 10 V. The insert shows a Schottky plot, log(I) as a function of $V^{1/2}$, the linear relation supports a Schottky type of emission at higher biases.

absorption component seems to dominate the signal in the visible range, while field-assisted (Schottky/FN) emission becomes predominant for the infrared range. This regime remains the target; however, in these runs the FTIR signal was off-band (NIR tail), so true LWIR performance is still to be demonstrated.

The second main conclusion to be drawn is related to the oxide capacitive role, acting as a distributed RC network influencing the frequency response of the circuit. As further transient analyses are carried out, this hypothesis remains to be confirmed. If proven correct, the refinement of the underetching technique will become even more critical for device optimization. Future improvements to the optical path and chopper frequency have the possibility to give a preliminary estimate of the device response time, which preliminary data suggest to be below the millisecond range. As reported in similar devices, optimal measurement conditions often exist for applied bias and frequency, yielding maximum signal-to-noise ratio (SNR). To identify said conditions, a noise characterization is necessary, especially to separate instrumental and device intrinsic noise.

Even if related to a preliminary stage, the measurements demonstrate measurable and reproducible photoresponse in several arrays, most of the results corresponding to Schottky-based bowtie geometries. As similar results are expected by the remaining geometries, further investigation is needed to confirm them. Detectivity estimates span roughly 10^8 Jones in the visible regime, 10^4 - 10^5 Jones in the mid-IR (HeNe $\lambda=3.39 \ \mu m$), and $\approx 10^5$ Jones (off-band, NIR-tail) near resonance under FTIR illumination. The device's main strength appears to be its bandwidth, while its optical sensitivity requires further refinement. Current measurement limitations are related to the oxide charging effect, introducing frequency noise and masking the device's intrinsic noise levels, and the readout bandwidth-gain trade-off. Next steps will involve extending the swept frequency range into the 5f regime, refining oxide removal, and performing an accurate noise-spectrum analysis via VMA on larger test structures. The latter remains the main challenge to overcome for proper device benchmarking, as it will enable an accurate assessment of D^* . Additional LWIR testing is needed to verify the device response in the designated regime.

7. Conclusions and Future Perspectives

This thesis addressed the design, fabrication, and preliminary characterization of a plasmonic nanoantenna-based device for infrared (IR) detection at room temperature, aiming at the realization of a higher-performance device than the common uncooled devices. The main goal was to demonstrate a system combining plasmonic field enhancement with field-assisted electron emission mechanisms as a viable approach for IR detection. The electron emission theories considered were Schottky emission and Fowler-Nordheim (FN) tunneling. The project followed the process from a theoretical concept to the first experimental measurements. Preliminary tests showed measurable photocurrent generation with promising trends and characteristics, successfully proving the main objective of the project.

The aim is to explore this new approach to room-temperature IR detection, based on field-assisted emission phenomena as an alternative to conventional semiconductor or bolometric mechanisms. Building upon previous work carried out at the Quantum Nanostructures and Nanofabrication (QNN) group at MIT, similar architectures were redesigned to exploit these phenomena. The concept drew inspiration from a device originally designed for field sampling in electron emission, which was here adapted for optical detection. On the theoretical side, part of the project focused on verifying which electron emission regime, amongst Fowler–Nordheim or Schottky, predominates in the device behaviour. Conducted analysis aimed to clarify the roles of temperature and electric field enhancement, and how they interact with plasmonic nanoantenna structures. The understanding of the dominant regime is fundamental to clarifying the physical mechanisms governing the proposed design and explaining how the structures respond through their combined thermal and plasmonic effects, ultimately enabling good responsivity at room temperature.

In the design stage, several geometries were created, addressing both field enhancement and thermal hotspot exploitation simultaneously. Four main geometries were developed, divided into two couples, each targeting one of the two phenomena. The devices were fabricated through high-resolution electron-beam lithography (EBL) and inspected via scanning electron microscopy (SEM) imaging, pushing fabrication limits down to sub-20 nm gaps. The main fabrication bottleneck was the underetch procedure, needed to remove the oxide layer, known to affect

performance stability and frequency response. This step proved to be problematic due to the gold surface's sensitivity to plasma damage during dry etching.

After a long and careful design phase, a custom broadband infrared setup was built for device characterization. The setup integrated optical, mechanical, and electrical modules to meet the specific measurement requirements. Despite technical challenges, the setup enabled the first reproducible measurement of photocurrent from such nanoantenna structures, confirming both the functionality of the setup and the working principle of the device. Even if the measurements presented strict limitations from noise and other constraints, the recorded photocurrents clearly demonstrated light-induced response and revealed interesting behaviour across different excitation conditions.

Due to external constraints, only rough approximations of the device response could be obtained. Nevertheless, these results were sufficient to demonstrate the remarkable potential of the device. Measurements were carried out under the effect of three excitation sources: a red laser, a HeNe laser, and a broadband FTIR source. In the visible range, the estimated lower bound of detectivity reached $\sim 10^8$ Jones, while under FTIR illumination it was $\sim 10^5$ Jones (off-band, NIR-tail); true LWIR in-band detectivity remains to be demonstrated. Although preliminary, these estimates yield exciting potential and highlight the promise of this early fabrication run. The large mismatch in detectivity in the two regimes suggests a system driven by two physical mechanisms, where multiphoton absorption dominates in the visible range and field-assisted emission emerges at longer wavelengths. Preliminary verifications also confirm a Schottky-type emission in the Schottky-based geometries.

Some limitations arose during the measurements phase, mainly due to the charge trapping in the oxide layer acting as a capacitive element. This effect introduced low-frequency noise and transient current effects, limiting the maximum accuracy achievable in performance estimation. Confirming its origin through further investigation will enable the suppression through a finer and better-controlled underetch process.

Another interesting and promising aspect of the device is its fast temporal response, which appears to be particularly short, especially compared to microbolometers, currently state-of-the-art devices for room-temperature IR detection. Next steps will involve frequency modulation tests, combined with more accurate noise-spectrum characterization using a Vector Measurement Analyzer (VMA) on larger test structures. This may allow the identification of device intrinsic noise, currently masked by electronic readout noise, and a more precise estimation of detectivity (D^*) .

Despite these challenges and limitations, the results obtained in this thesis establish a strong starting point for the continuation of the project. It was possible to generate photocurrent from plasmonic nanoantennas under IR excitation, bringing

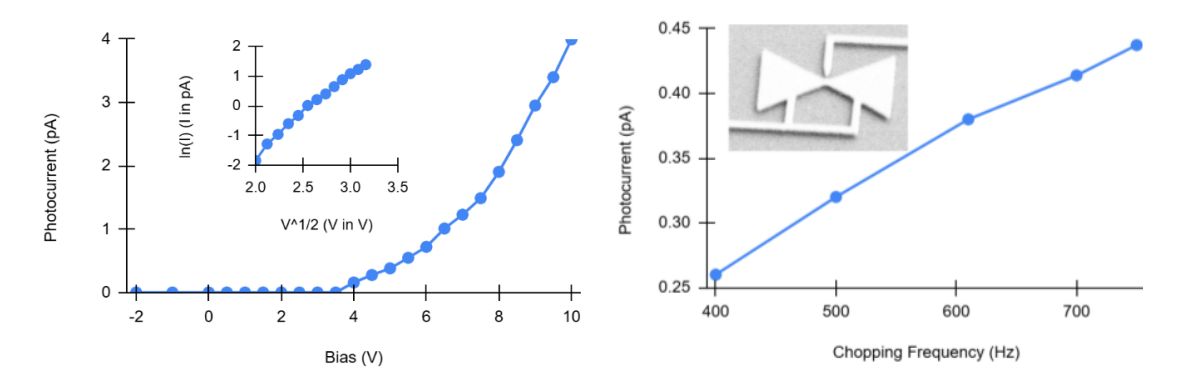


Figure 7.1: Summary of first measurements, determining the first photocurrent in Schottky-type devices. Left: FTIR illumination (source 1.5–17 μm ; measured response attributed to the NIR tail) photocurrent vs. bias. Peak responsivity at 10 V is 45 m/W. Inset: log(I) vs $V^{1/2}$; the linear trend indicates Schottky-type emission at higher biases. Right: measured photocurrent in the lock-in vs chopping frequency. The monotonic increase with frequency is consistent with charging-induced high-pass behavior; no roll-off was observed within the tested range ($\sim kHz$).

this project closer to the realization of IR detectors. Further optimization may lead to integrated imaging arrays capable of producing low-power, ultrafast, uncooled IR detection. Such a system would represent a novelty in the existing market, where room-temperature IR detectors are usually limited to microbolometers, characterized by low sensitivity and slow response times.

In summary, this thesis was able to bridge the gap between theoretical hypotheses and experimental realization of field-assisted IR detectors. The concept's feasibility was proved, revealing promising trends and establishing a baseline for future iterations. This work defines a first benchmark for the next generation of fast, uncooled nanoscale IR detectors, paving the way for a novel approach to optical sensing.

References

- [1] M. F. S. Ferreira et al. "Roadmap on optical sensors". In: *Journal of Optics* 26.1 (2024), p. 013001. DOI: 10.1088/2040-8986/ad0e85.
- [2] I. Kim, R. J. Martins, J. Jang, T. Badloe, S. Khadir, H.-Y. Jung, H. Kim, J. Kim, P. Genevet, and J. Rho. "Nanophotonics for light detection and ranging technology". In: *Nature Nanotechnology* 16.5 (2021), pp. 508–524. DOI: 10.1038/s41565-021-00895-3.
- [3] A. Rogalski. *Infrared and Terahertz Detectors*. 3rd. CRC Press, 2019. DOI: 10.1201/b21951.
- [4] B. Xu, Z. Chen, T. W. Hänsch, and N. Picqué. "Near-ultraviolet photon-counting dual-comb spectroscopy". In: *Nature* 627 (2024), pp. 289–294. DOI: 10.1038/s41586-024-07094-9.
- [5] H. Yu, L. McCuller, M. Tse, N. Kijbunchoo, L. Barsotti, N. Mavalvala, and m. o. t. L. S. Collaboration. "Quantum correlations between light and the kilogram-mass mirrors of LIGO". In: *Nature* 583.7814 (2020), pp. 43–47. DOI: 10.1038/s41586-020-2420-8.
- [6] D. Dicken et al. "JWST MIRI flight performance: Imaging". In: *Astronomy & Astrophysics* 689 (2024), A5. DOI: 10.1051/0004-6361/202449451.
- [7] Y. Ma et al. "Day-Night imaging without Infrared Cutfilter removal based on metal-gradient perovskite single crystal photodetector". In: *Nature Communications* 15 (2024), p. 7516. DOI: 10.1038/s41467-024-51762-3.
- [8] S. Lischke et al. "Ultra-fast germanium photodiode with 3-dB bandwidth of 265 GHz". In: *Nature Photonics* 15.?, correction issued (2021), pp. 925–931. DOI: 10.1038/s41566-021-00948-y.
- [9] Y.-A. Chen et al. "An integrated space-to-ground quantum communication network over 4,600 kilometres". In: *Nature* 589.7841 (2021), pp. 214–219. DOI: 10.1038/s41586-020-03093-8.
- [10] D. I. Herman, M. Walsh, M. K. Kreider, N. Lordi, E. J. Tsao, A. J. Lind, M. Heyrich, J. Combes, J. Genest, and S. A. Diddams. "Squeezed dual-comb spectroscopy". In: *Science* 387.6734 (2025), pp. 653–658. DOI: 10.1126/science. ads6292.

- [11] N. T. Huynh et al. "A fast all-optical 3D photoacoustic scanner for clinical vascular imaging". In: *Nature Biomedical Engineering* 9 (2025), pp. 638–655. DOI: 10.1038/s41551-024-01247-x.
- [12] P. Beard. "Biomedical photoacoustic imaging". In: *Interface Focus* 1.4 (2011), pp. 602–631. DOI: 10.1098/rsfs.2011.0028.
- [13] D. Gehrig and D. Scaramuzza. "Low-latency automotive vision with event cameras". In: *Nature* 629.8014 (2024), pp. 1034–1040. DOI: 10.1038/s41586-024-07409-w.
- [14] M. Bailes et al. "Gravitational-wave physics and astronomy in the 2020s and 2030s". In: *Nature Reviews Physics* 3.5 (2021), pp. 344–366. DOI: 10.1038/s42254-021-00303-8.
- [15] A. Rogalski. "Scaling infrared detectors—status and outlook". In: Reports on Progress in Physics 85.12 (2022), p. 126501. DOI: 10.1088/1361-6633/ac97a8.
- [16] A. Rogalski. "Semiconductor detectors and focal plane arrays for far-infrared imaging". en. In: *Opto-Electronics Review* 21.4 (Jan. 2013). ISSN: 1896-3757. DOI: 10.2478/s11772-013-0110-x. URL: http://www.degruyter.com/view/j/oere.2013.21.issue-4/s11772-013-0110-x/s11772-013-0110-x.xml (visited on 10/11/2025).
- [17] T. Akın. "Low-Cost LWIR-Band CMOS Infrared (CIR) Microbolometers for High Volume Applications". In: Proceedings of the IEEE 33rd International Conference on Micro Electro Mechanical Systems (MEMS 2020). 2020. DOI: 10.1109/MEMS46641.2020.9056383.
- [18] L. Yu, Y. Guo, H. Zhu, M. Luo, P. Han, and X. Ji. "Low-Cost Microbolometer Type Infrared Detectors". In: *Micromachines* 11.9 (2020), p. 800. DOI: 10. 3390/mi11090800.
- [19] H.-J. Syu, Y.-C. Huang, Z.-C. Su, R.-L. Sun, and C.-F. Lin. "An Alternative to Compound Semiconductors Using a Si-Based IR Detector". In: *IEEE Transactions on Electron Devices* 69.1 (2022), pp. 205–211. DOI: 10.1109/ TED.2021.3130566.
- [20] D. Z. Ting, A. Soibel, A. Khoshakhlagh, S. A. Keo, S. B. Rafol, A. M. Fisher,
 B. J. Pepper, E. M. Luong, C. J. Hill, and S. D. Gunapala. "Advances in
 III-V semiconductor infrared absorbers and detectors". In: *Infrared Physics Technology* 97 (2019), pp. 126–152. DOI: 10.1016/j.infrared.2018.12.034.
- [21] A. Rogalski. "History of infrared detectors". en. In: Opto-Electronics Review 20.3 (Jan. 2012). ISSN: 1896-3757. DOI: 10.2478/s11772-012-0037-7. URL: http://www.degruyter.com/view/j/oere.2012.20.issue-3/s11772-012-0037-7/s11772-012-0037-7.xml (visited on 10/02/2025).

- [22] A. Rogalski. "Recent progress in infrared detector technologies". In: *Infrared Physics & Technology*. Proceedings of the International Conference on Quantum Structure Infrared Photodetector (QSIP) 2010 54.3 (May 2011), pp. 136–154. ISSN: 1350-4495. DOI: 10.1016/j.infrared.2010.12.003. URL: https://www.sciencedirect.com/science/article/pii/S1350449510001040 (visited on 10/02/2025).
- [23] T. D. Dao et al. "MEMS-Based Wavelength-Selective Bolometers". en. In: *Micromachines* 10.6 (June 2019). Publisher: Multidisciplinary Digital Publishing Institute, p. 416. ISSN: 2072-666X. DOI: 10.3390/mi10060416. URL: https://www.mdpi.com/2072-666X/10/6/416 (visited on 10/02/2025).
- [24] S. Jiang, J. Li, J. Li, J. Lai, and F. Yi. "Metamaterial microbolometers for multi-spectral infrared polarization imaging". en. In: *Optics Express* 30.6 (Mar. 2022), p. 9065. ISSN: 1094-4087. DOI: 10.1364/OE.452981. URL: https://opg.optica.org/abstract.cfm?URI=oe-30-6-9065 (visited on 10/02/2025).
- [25] IR Detectors For Thermographic Imaging. URL: https://www.photonicsonline. com/doc/ir-detectors-for-thermographic-imaging-0001 (visited on 10/11/2025).
- [26] H.-W. Fink. "Point source for ions and electrons". In: *Physica Scripta* 38.2 (1988), pp. 260–263. DOI: 10.1088/0031-8949/38/2/029.
- [27] C. A. Spindt, I. Brodie, L. Humphrey, and E. R. Westerberg. "Physical properties of thin-film field emission cathodes with molybdenum cones". In: *Journal of Applied Physics* 47.12 (1976), pp. 5248–5263. DOI: 10.1063/1.322600.
- [28] A. V. Crewe, D. N. Eggenberger, J. Wall, and L. M. Welter. "Electron gun using a field emission source". In: *Review of Scientific Instruments* 39.4 (1968), pp. 576–583. DOI: 10.1063/1.1683435.
- [29] E. W. Müller. "Field desorption". In: Physical Review 102 (1956), pp. 618–624.
 DOI: 10.1103/PhysRev.102.618.
- [30] M. R. Bionta, F. Ritzkowsky, M. Turchetti, Y. Yang, D. C. Mor, W. P. Putnam, F. X. Kärtner, K. K. Berggren, and P. D. Keathley. "On-chip sampling of optical fields with attosecond resolution". In: *Nature Photonics* 15.6 (2021), pp. 456–460. DOI: 10.1038/s41566-021-00792-0.
- [31] P. Rácz, Z. Pápa, I. Márton, J. Budai, P. Wróbel, T. Stefaniuk, C. Prietl, J. R. Krenn, and P. Dombi. "Measurement of nanoplasmonic field enhancement with ultrafast photoemission". In: Nano Letters 17.2 (2017), pp. 1181–1186. DOI: 10.1021/acs.nanolett.6b04893.
- [32] L. V. Keldysh. "Ionization in the Field of a Strong Electromagnetic Wave". In: Soviet Physics JETP 20.5 (1965), pp. 1307–1314.

- [33] C. Heide, P. D. Keathley, and M. F. Kling. "Petahertz electronics". en. In: *Nature Reviews Physics* 6.11 (Nov. 2024). Publisher: Nature Publishing Group, pp. 648–662. ISSN: 2522-5820. DOI: 10.1038/s42254-024-00764-7. URL: https://www.nature.com/articles/s42254-024-00764-7 (visited on 09/11/2025).
- [34] Q. Sun, C. Zhang, W. Shao, and X. Li. "Photodetection by Hot Electrons or Hot Holes: A Comparable Study on Physics and Performances". In: *ACS Omega* 4.3 (Mar. 2019). Publisher: American Chemical Society, pp. 6020–6027. DOI: 10.1021/acsomega.9b00267. URL: https://doi.org/10.1021/acsomega.9b00267 (visited on 10/12/2025).
- [35] H. Chalabi, D. Schoen, and M. L. Brongersma. "Hot-Electron Photodetection with a Plasmonic Nanostripe Antenna". en. In: *Nano Letters* 14.3 (Mar. 2014), pp. 1374–1380. ISSN: 1530-6984, 1530-6992. DOI: 10.1021/nl4044373. URL: https://pubs.acs.org/doi/10.1021/nl4044373 (visited on 09/07/2025).
- [36] P. Pertsch, R. Kullock, V. Gabriel, L. Zurak, M. Emmerling, and B. Hecht. "Tunable nano-plasmonic photodetectors". In: *Nano Letters* 22.17 (Sept. 2022). arXiv:2204.13978 [physics], pp. 6982–6987. ISSN: 1530-6984, 1530-6992. DOI: 10.1021/acs.nanolett.2c01772. URL: http://arxiv.org/abs/2204.13978 (visited on 10/12/2025).
- [37] S. Piltan and D. Sievenpiper. "Plasmonic nano-arrays for enhanced photoe-mission and photodetection". en. In: Journal of the Optical Society of America B 35.2 (Feb. 2018), p. 208. ISSN: 0740-3224, 1520-8540. DOI: 10.1364/JOSAB. 35.000208. URL: https://opg.optica.org/abstract.cfm?URI=josab-35-2-208 (visited on 09/07/2025).
- [38] M. Turchetti, Y. Yang, M. Bionta, A. Nardi, L. Daniel, K. K. Berggren, and P. D. Keathley. "Electron Emission Regimes of Planar Nano Vacuum Emitters". en. In: *IEEE Transactions on Electron Devices* 69.7 (July 2022), pp. 3953–3959. ISSN: 0018-9383, 1557-9646. DOI: 10.1109/TED.2022. 3175706. URL: https://ieeexplore.ieee.org/document/9780588/ (visited on 09/07/2025).
- [39] W. S. Koh, L. K. Ang, and T. J. T. Kwan. "Three-dimensional Child–Langmuir law for uniform hot electron emission". en. In: *Physics of Plasmas* 12.5 (May 2005), p. 053107. ISSN: 1070-664X, 1089-7674. DOI: 10.1063/1.1913612. URL: https://pubs.aip.org/pop/article/12/5/053107/1015578/Three-dimensional-Child-Langmuir-law-for-uniform (visited on 09/07/2025).
- [40] D. Tomer, S. Rajput, L. J. Hudy, C. H. Li, and L. Li. "Carrier transport in reverse-biased graphene/semiconductor Schottky junctions". In: Applied Physics Letters 106.17 (May 2015), p. 173510. ISSN: 0003-6951. DOI: 10.1063/1.4919727. URL: https://doi.org/10.1063/1.4919727 (visited on 09/13/2025).

- [41] G. Gaertner, W. Knapp, and R. G. Forbes, eds. Modern Developments in Vacuum Electron Sources. en. Vol. 135. Topics in Applied Physics. Cham: Springer International Publishing, 2020. ISBN: 978-3-030-47290-0 978-3-030-47291-7. DOI: 10.1007/978-3-030-47291-7. URL: http://link.springer.com/10. 1007/978-3-030-47291-7 (visited on 09/13/2025).
- [42] "(PDF) Semiconductor detectors and focal plane arrays for far-infrared imaging". en. In: ResearchGate (Aug. 2025). DOI: 10.2478/s11772-013-0110-x. URL: https://www.researchgate.net/publication/258170389_Semiconductor_detectors_and_focal_plane_arrays_for_far-infrared_imaging (visited on 10/11/2025).
- [43] R. G. Hobbs, W. P. Putnam, A. Fallahi, Y. Yang, F. X. Kärtner, and K. K. Berggren. "Mapping Photoemission and Hot-Electron Emission from Plasmonic Nanoantennas". en. In: *Nano Letters* 17.10 (Oct. 2017), pp. 6069–6076. ISSN: 1530-6984, 1530-6992. DOI: 10.1021/acs.nanolett.7b02495. URL: https://pubs.acs.org/doi/10.1021/acs.nanolett.7b02495 (visited on 09/07/2025).
- [44] W. (Hu, K. Sarveswaran, M. Lieberman, and G. H. Bernstein. "Sub-10 nm electron beam lithography using cold development of poly(methylmethacrylate)". en. In: Journal of Vacuum Science & Technology B: Microelectronics and Nanometer Structures Processing, Measurement, and Phenomena 22.4 (July 2004), pp. 1711–1716. ISSN: 1071-1023, 1520-8567. DOI: 10.1116/1.1763897. URL: https://pubs.aip.org/jvb/article/22/4/1711/589595/Sub-10-nm-electron-beam-lithography-using-cold (visited on 10/11/2025).
- [45] L. Carl Zeiss Microscopy. Fundamentals of Scanning Electron Microscopy in Life Science Research. 2022. URL: https://www.zeiss.com/microscopy/us/products/scanning-electron-microscopes/upgrades/fe-sem.html.
- [46] J. Bean. "Zeiss SEM Operating Instructions". en. In.
- [47] Z. Gemini and Z. Gemini. "Standard Operating Procedure". en. In.
- [48] M. Hejduk and B. R. Heazlewood. "Off-axis parabolic mirror relay microscope for experiments with ultra-cold matter". eng. In: *The Review of Scientific Instruments* 90.12 (Dec. 2019), p. 123701. ISSN: 1089-7623. DOI: 10.1063/1. 5123792.
- [49] E. A. Orlenko, T. Y. Cherezova, Y. V. Sheldakova, A. L. Rukosuev, and A. V. Kudryashov. "Off-axis parabolic mirrors: A method of adjusting them and of measuring and correcting their aberrations". en. In: *Journal of Optical Technology* 72.4 (Apr. 2005), p. 306. ISSN: 1070-9762. DOI: 10.1364/JOT.72. 000306. URL: https://opg.optica.org/jot/abstract.cfm?uri=jot-72-4-306 (visited on 08/28/2025).

- [50] K. Newman. "An introduction to off-axis parabolic mirrors". In: 2013. URL: https://www.semanticscholar.org/paper/An-introduction-to-off-axis-parabolic-mirrors-Newman/90994aa3fb16400723d7e55b81cee014f5d794c7 (visited on 10/12/2025).
- [51] S.-C. Her and C.-F. Chang. "Fabrication and Characterization of Indium Tin Oxide Films". In: Journal of Applied Biomaterials & Functional Materials 15.2 (Apr. 2017), pp. 170–175. ISSN: 2280-8000. DOI: 10.5301/jabfm.5000345. URL: https://www.ncbi.nlm.nih.gov/pmc/articles/PMC6379771/ (visited on 08/25/2025).
- [52] R. E. Parks, C. J. Evans, and L. Shao. "Test of a slow off-axis parabola at its center of curvature". en. In: Applied Optics 34.31 (Nov. 1995), p. 7174. ISSN: 0003-6935, 1539-4522. DOI: 10.1364/AO.34.007174. URL: https://opg.optica.org/abstract.cfm?URI=ao-34-31-7174 (visited on 08/28/2025).
- [53] "http://beammeasurement.mellesgriot.com/tut_shear_plate_test.asp". en. In.
- [54] Y. Yang, M. Turchetti, P. Vasireddy, W. P. Putnam, O. Karnbach, A. Nardi, K. K. Berggren, F. X. Kärtner, and P. D. Keathley. "Light phase detection with on-chip petahertz electronic networks". In: *Nature Communications* 11 (2020), p. 3407. DOI: 10.1038/s41467-020-17250-0.
- [55] M. Turchetti, M. R. Bionta, Y. Yang, F. Ritzkowsky, D. R. Candido, M. E. Flatté, K. K. Berggren, and P. D. Keathley. "Impact of DC bias on weak optical-field-driven electron emission in nano-vacuum-gap detectors". EN. In: JOSA B, Vol. 38, Issue 3, pp. 1009-1016 (Mar. 2021). Publisher: Optica Publishing Group. DOI: 10.1364/JOSAB.413680. URL: https://opg.optica.org/josab/abstract.cfm?uri=josab-38-3-1009 (visited on 10/07/2025).